Study of Charge Transport Properties of Conjugated Polymers and Photovoltaic performance of Bulkheterojunction Solar Cells

By

Siraye Esubalew Debebe

A Thesis submitted to
The Department of Chemistry

Presented in Fulfillment of The Requirements for the Degree of

Doctor of Philosophy (Chemistry)

Addis Ababa University

Addis Ababa, Ethiopia

May 2012

Addis Ababa University

School of Graduate Studies

This is to certify that the thesis prepared by Siraye Esubalew Debebe entitled: *Study of Charge Transport Properties of Conjugated Polymers and Photovoltaic Performance of Bulkheterojunction Solar Cells* and submitted in partial fulfillment of the requirements for the Degree of Doctor of Philosophy (Physical Chemistry) complies with the regulations of the University and meets the accepted standards with respect to originality and quality.

Signed by the Examining Committee

Name	Signature	Date
Prof. Olle Inganäs External Examiner		29 May 2012
Prof. Theodros Solomon Examiner		29 May 2012
Dr. Ahmed Mustefa Examiner		29 May 2012
Dr. Shimelis Admassie Examiner		29 May 2012
Prof. Teketel Yohannes Advisor		29 May 2012

Chair of Department or Graduate Program Coordinator

ABSTRACT

Study of Charge Transport Properties of Conjugated Polymers and Photovoltaic performance of Bulkheterojunction Solar Cells

SIRAYE ESUBALEW DEBEBE

Addis Ababa University, Chemistry Department

Ethiopia, 2012

Alternative energy source of the world in the future is organic photovoltaic, which is sustainable and environmentally friendly. Among the different organic photovoltaics, the class of bulk heterojunction solar cells required to have 10% power conversion efficiency and 10 years of life time to be commercialized.

However, there are many factors that limit their performance. One of these factors is the charge carrier mobility. Therefore, the mobilities of different polymers (APFO-Green 6, APFO-Green 5 and a novel Phenyl substituted Polythiophene compound called PPOPT) have been characterized in order to understand the effect of mobility in their performance.

Transport of holes in a low band gap polyfluorene, APFO-Green6, was investigated by means of admittance spectroscopy in the modulation frequency range 1-5x10^5 Hz and found to be in the order of 10x^{-6} $cm^2V^{-1}s^{-1}$. At room temperature hole mobility of APFO-Green6 is dependent on the applied electric filed, as commonly observed in disordered organic materials. The excess capacitance towards low frequencies provides evidence for charge relaxation in trap levels. A dispersion parameter of 0.4 was achieved from the trend of holes transit times with the electric field. CELIV technique was also applied, but the characteristic signal was not observed. However, it was used to determine the polymer

dielectric constant and found to be 3, which is very common value to many organic materials.

The bulk transport properties of positive carriers in thin films of a low band-gap conjugated polymer, called APFO-Green5, have also been investigated with the ac Admittance technique. The capacitance response at low frequency gave indication of a combination of trapping and double-injection effects, while in the intermediate-high frequency range was determined by the transit time of injected holes. Hole mobility in APFO-Green5 thin films exhibited a Frenkel-like dependence on the applied electric field, with a field-dependent coefficient of around 8×10^{-3} $(Vcm^{-1})^{-1/2}$. A hole mobility close to 2×10^{-5} cm^2 V^{-1} s^{-1} was achieved at the field of $3.5x10^5$ Vcm^{-1}, in excellent agreement with that already reported by using a different bulk investigation technique. The temperature effect was also studied and the charge transport parameters were extracted by analyzing the mobility data by the uncorrelated and the correlated Gaussian Disorder Models. DISCL transient technique was also applied and one order magnitude higher value to that of AS was achieved.

Characterization of a novel polythiophene substituted with a 2'-pentyloxy-5'-(1'''-oxooctyl) phenyl group (PPOPT) is also reported. Optical and electrochemical studies were done. The HOMO (-5.49 eV) and LUMO (-3.14 eV) levels have been determined. The bulk transport properties of thin films of PPOPT are investigated by admittance spectroscopy. The dramatic effect of the phenyl side chain on the mobility of positive carriers in films of PPOPT is described. The photophysics of PPOPT in both solution and thin film is also investigated and correlated to substituent-driven intrachain and interchain arrangements.

More over two other polymers were used to develop bulkheterojunction solar cells and characterized. One of the polymers that is used in a photovoltaic characterization is a novel family of fluorene–thiophene-benzothiadiazole containing, poly{[4'-(9,9-bis(2-ethylhexyl)fluoren-2-yl)-2',1',3'-benzothiadiazole-7,7'-diyl]-co-[2'-(9,9-bis(2-ethyl-hexyl)fluoren-2-yl)thien-7,5'-diyl]} (PFB-co-FT), random copolymers . The study includes selection of the best solvent, analyzing annealing effects, optimization of polymer: PCBM weight ratio, optimization of the active layer thickness and studying the effect of LiF buffer layer in order to get optimized performance. The effect of the incident light intensity was also investigated in order to get insight about the space charge effect on the device. The optimum performance is around 1% and the light intensity study indicates that little or no significant effect of space charge in the solar cell devices.The other bulk heterojunction solar cell characterized is Poly{[2,7-(9,9-bis-(2-ethylhexyl)-fluorene)]-alt-[5,5-(4,7-di-2'-thienyl-2,1,3-benzothiadiazole)]}:PCBM. The solar cells were also characterized under different incident light power intensities. Charge trapping effects take place at low fullerene content in the photoactive blend; an efficient polymer fullerene intermixing with formation of continuous phases is reached at a donor: acceptor ratio of 1:4. For an optimized active layer thickness of 100 nm a power conversion efficiency of 2.57% was obtained. Photocurrent measurements under reverse bias conditions show that a high percentage of the photogenerated excitons do not lead to the formation of free carriers; thus representing the major limiting factor for the devices efficiency.

Key words: Hole mobility, Transport properties, Admittance spectroscopy Conjugated polymers, Polyfluorene, phenyl substitution, organic solar cell, Bulk heterojunction

ACKNOWLEDGEMENTS

There are many institutions and individuals, who have contributed different supports to see this thesis work realized. I would like, in general, to acknowledge all of them for their support.

I especially express my gratitude to Prof. Teketel Yohannes for his all round support and introducing me to the field of application of conjugated polymers for optoelectronic devices. His excellent friendliness and good personality have encouraged me to feel free and relaxed in my stay in this study. Beyond the scientific advisorship, his "stress free" behavior was very inviting to have a discussion with him even personal problems.

My sincere thanks also goes to Dr. Nadia Camaioni for supervising and hosting my most laboratory work, when I was in CNR-Bologna laboratory. I appreciate her patience in managing different problems occurred during the laboratory work. I am also deeply indebted for her concern for my personal life and making me feel at home during my stay in Italy and unreserved interest to discuss the scientific issues whenever we had been together.

I express my sincere thanks to the Camaioni's group members, colleagues and collaborators for their unreserved support during my lab work in CNR- Bologna; Francesca Tinti, Alberto Zaneli, Valeria Fattori, Massimo Cocchi, Anna Calaberes, Recardo Po and Alessandro Martelli just to mention a few.

I would like to thank Prof. Wondimagegn Mamo for providing me most of the polymers, which I have used in this study and encouraging me every time we have met, Dr Shimelis Adimassie for encouraging and advising what to do in solving issues, Dr Merid

Tesema for his concern of my wellbeing and life and all staff members of Chemistry Department, Addis Ababa University, for their encouragement and help during my study in the department.

I would like to acknowledge the contribution of the following institutions: Gondar College of Teacher Education for allowing me to pursue my PhD, Department of Chemistry, Addis Ababa University, for giving me the opportunity to do my PhD, the Abdus Salam International Center for Theoretical Physics (ICTP) for granting me a fellowship through its TRIL program to do my research work in CNR-Bologna, Italy and ENI S.P.A. for supporting part of my work.

My especial thanks goes to Dr. Negussie Wodajo for his concern of my wellbeing and life in general and who has helped me to join my PhD program at the beginning, in particular. He was very dedicated to check my status very regularly in those of five years during my stay like a father does. Really I always appreciate what he has done to me from the bottom of my heart.

Many thanks to my friends Kahsay G. Egziabiher, Alemayehu Mekonnen, Tesfay Atsibeha, Desta Aniteneh, Belina Terfasa, Getachew Adam, Sisay Tadesse, Solomon Mihretie, Gebre Admasu, Mulugeta Mengistu and others for their encouragement and moral support.

I would like to express my sincere thanks, in particular to Tinsae Birhanie and his family for their patience and wise handling of all issues and financial matters in my home base institution, Gondar College of Teacher Education, on behalf of me.

Finally, I would like to express my deepest gratitude to my wife Tesfa Belete, who suffered a lot in those long five years of my stay in Addis for the sake of our bright future,

for encouraging me in the time of desperate and taking care of our two lovely kids. I also thank my kids Erimias and Helina for the love you always give me, when I come home very tired.

Siraye Esubalew Debebe

Addis Ababa

Ethiopia

Table of Contents

LIST OF FIGURES xii

LIST OF TABLES xxi

ABBREVATIONS xxii

1 Fundamentals of charge transport and organic photovoltaic 1

1.1 Introduction 1

1.2 Charge transport in organic semiconductors 3

1.2.1 Charge transport models 6

1.2.2 Charge Carrier Disorder Formalisms 11

1.3 Charge transport measurement techniques 12

1.3.1 Time of Flight (TOF) 13

1.3.2 Charge Extraction by a Linearly Increasing Voltage (CELIV) 18

1.3.3 Dark Injection Space Charge Limited Current transient method (DISCLC) 22

1.3.4 Admittance spectroscopy (AS) 24

1.3.5 Space charge limited current 29

1.4 Organic Photovoltaic 31

1.4.1 Introduction 31

1.4.2 A tendency towards Bulk heterojunction Organic Solar cells 33

1.4.3 Basics of Bulk heterojunction organic photovoltaic 36

1.4.4 Device performance characterization 44

1.4.5 Optimization of bulk heterojunction solar cells 48

1.4.6 Effect of illumination intensity on short circuit current and open circuit voltage 53

1.5 Objectives of the study 55

2 Experimental 56

2.1 General 56
2.2 Hole mobility measurement of APFO-Green 6 57
2.2.1 Hole mobility measurement of APFO-Green 6 with AS 57
2.2.2 Hole mobility measurement of APFO-Green 6 with CELIV 58
2.3 Hole mobility measurement of APFO-Green 5 58
2.3.1 Hole mobility measurement of APFO-Green 5 with AS 58
2.3.2 Hole mobility measurement of APFO-Green 5 with DISCL transient 59
2.4 Transport property of a novel phenyl substituted polythiophene (PPOPT) 60
2.5 Bulk –hetero junction solar cell of random Co-polymer (PF-Co-FT) 61
2.6 BisEH-PFDTBT: PCBM solar cells: a compositional, thickness, and light intensity dependence study 62
3. Result and Discussion 63
3.1 Hole mobility measurement of APFO-Green 6 63
3.1.1 Hole mobility measurement with Admittance Spectroscopy 64
3.1.2 Hole mobility measurement of APFO-Green 6 with CELIV 69
3.1.3 Conclusion 70
3.2 Hole transport property of APFO-Green 5 71
3.2.1 Hole mobility measurement of APFO-Green 5 with Admittance Spectroscopy 72
3.2.1.1 Room Temperature Hole mobility 74
3.2.1.2 Effect of Temperature on Hole mobility 81
3.2.2 Hole mobility measurement of APFO-Green 5 with DISCL transient 88
3.2.3 Conclusion 90
3.3 Transport property of a novel phenyl-substituted polythiophene 92
3.3.1 Optical study 93
3.3.2 Electrochemical study 95

3.3.3 Transport study with AS 96
3.3.4 Conclusion 100
3.4 Bulk-heterojunction solar cells of a random co-polymer (PFB-co-FT) 102
3.4.1 Optical study 103
3.4.2 Photovoltaic properties 104
3.4.3 Conclusion 111
3.5 BisEH-PFDTBT: PCBM solar cells: a compositional, thickness, and light intensity-dependent study 112
3.5.1 Effect of blend composition 113
3.5.2 Light intensity effect 119
3.5.3 Generation of free electron-hole pairs 121
3.5.4 Effect of active layer thickness and LiF buffer layer 124
3.5.5 Conclusion 127
4. References 128

LIST OF FIGURES

Figure 1.1 Schematic view of the fibrillar structure of polyacetylene 4

Figure 1.2 Band transport mechanism in solids a) Perfectly ordered crystal b) Real crystal that involves lattice vibration.....7

Figure 1.3 Principle of the multiple trapping and thermal release limited charge transport, E_F is Fermi energy, E_t trap energy, E_C conduction energy leve.....8

Figure 1.4 Hopping due to lattice vibration transport mechanism in solids.....10

Figure 1.5 Scheme of TOF apparatus.....14

Figure 1.6. Photocurrent versus time response of TOF.....15

Figure 1.7. Typical transient photocurrents: (a) non-dispersive; (b) dispersive. Inset double logarithmic plot.....16

Figure 1.8. A schematic illustration of the CELIV technique. (a) Process of charge extraction. The region $0 \leq x \leq l(t)$ where all electrons have already been extracted is depicted by the shaded area. (b) Scheme of the voltage input and (c) The current density response with capacitive offset Jo and a current density due to drift with maximum of current ΔJ.....19

Figure 1.9. Schematic set up of CELIV: (a) function generator, (b) sample sandwiched between electrodes, (c) variable resistor and (d) oscilloscope.....20

Figure 1.10 An ideal DI-SCLC transient.....23

Figure 1.11 (a) the Ac and DC electrical waves; (b) AS configuration.....24

Figure 1.12 (a) A theoretical capacitance spectrum $C = ImY/\omega$. An example of response due to charge detrapping is plotted by the dashed line. (b) The corresponding change of susceptance, $-\Delta B$.....27

Figure1.13 Different architectures of thin film organic solar cells and their corresponding charge generation and transfer. (a) A single-layer, (b) Bi-layer and (c) Bulk heterojunction solar cell. 34

Figure 1.14 Schematic band diagram of a bulk heterojunction. The numbers refer to the operation processes explained in the text. The dashed line represents the energy levels of the acceptor, while the full lines indicate the energy level of the donor in the PV cell.....37

Figure 1.15 Sun flux 38

Figure 1.16 Equivalent circuit used to model solar cell..... ...45

Figure 1.17 Typical current–voltage characteristics for dark and light current in a solar cell. J_{sc} is the short-circuit current density, V_{OC} is the open circuit voltage, J_M and V_M are the current and voltage at the maximum power point.....46

Figure 1. 18 Energy level diagram of solar cell components.....49

Figure1. 19 Molecular structures of [6,6]-phenyl-C61-butyric acid methyl ester (PCBM) and [6,6]-phenyl-C71-butyric acid methyl ester (PC70BM).....50

Figure 2.1 Device structure of ITO/PEDOT:PSS/APFO-Green 6/Al.....57

Figure 2.2 Device structure ITO/PEDOT:PSS/APFO-Green5/Al.....59

Figure 3.1 Absorption spectra of APFO-Green 6 and its molecular formula.....63

Figure 3.2 Energy levels of ITO/PEDOT:PSS/APFO-Green 6/Al.....64

Figure 3.3 Frequency dependence of conductance (a) and capacitance (b) for an ITO/PEDOT:PSS/APFO-Green6/Al device at different dc bias voltages (values in V_{bias} indicated in the figure). In the bottom figure the broken line

indicate the intermediate frequency range at which capacitance is lower than the geometrical capacitance.....66

Figure 3.4 Variation of capacitance (a) and negative differential susceptance (b) with frequency in the intermediate frequency range, at different dc bias voltages (values in V indicated in the figure).....67

Figure 3.5 Electric field dependence of (a) hole mobilities and (b) hole transit times for an ITO/PEDOT:PSS/APFO-Green6/Al device. The dotted line represents the linear fit to the experimental data.....68

Figure 3.6 CELIV measurement of ITO/PDOT:PSS/APFO-Green/Al, Device B. Thickness of PEDOT:PSS 40 nm, Polymer 380 nm, Al 100 nm. Inset is the ramp with A of 102 kV/s.....70

Figure 3.7 Molecular structure and absorption spectra of APFO-Green 5.....71

Figure 3.8 Device structure and Energy level diagram of ITO/PEDOT:PSS/APFO-Green5/Al.....73

Figure 3.9 Current density as a function of forward bias for an ITO/PEDOT:PSS/APFO-Green 5/Al device. The line is a fit to the experimental data by using the formula of Murgatroyd. The thickness of the polymer layer was 260 nm.....74

Figure 3.10 Frequency dependence of conductance for an ITO/PEDOT:PSS/APFO-Green 5/Al device, for dc bias (V_{bias}) values in the range 0 – 10 V and with a step of 1 V. The arrow indicates the direction of increasing V_{bias}.....75

Figure 3.11 Frequency dependence of capacitance for an ITO/PEDOT:PSS/APFO-Green 5/Al device at different dc bias values (values in V are shown in the figure) in the all range of the modulation frequency in log – log scale.....76

Figure 3.12 Low-frequency range dependence of capacitance for an ITO/PEDOT:PSS/APFO-Green 5/Al device at V_{bias} of 2 V (circles) and of 3 V (squares). The dotted lines represent the linear fits to the experimental data. The values of the dispersion parameter α are shown in the figure.....77

Figure 3.13 (a) Frequency dependence of capacitance for an ITO/PEDOT:PSS/APFO-Green 5/Al device at different dc bias values (values in V are shown in the figure) in the frequency range at which C is lower than the geometrical capacitance. (b) Variation of the negative differential susceptance with frequency at different dc bias voltages (values in V indicated in the figure). In the bottom figure, the lines are shown to guide the eye.....79

Figure 3.14 Electric field dependence of charge-carrier transit times. The line represents the linear fit to the experimental data. The value of the dispersion parameter α is shown in the figure.....80

Figure 3.15 Square-root field dependence of charge-carrier mobility for an ITO/PEDOT:PSS/APFO-Green 5/Al ..device. The line represents the linear fit to the experimental data.....81

Figure 3.16 Frequency dependence of conductance for an ITO/PEDOT:PSS/APFO-Green 5/Al device at different temperatures and for a dc bias of 6 V.....82

Figure 3.17 Intermediate-frequency spectra of capacitance (a) and negative differential susceptance (b) for an ITO/PEDOT:PSS/APFO-Green 5/Al device at different temperatures and for a dc bias of 6 V. In the bottom figure, the lines are shown to guide the eye.....83

Figure 3.18 Square-root field dependence of the average hole mobility for an ITO/PEDOT:PSS/APFO-Green 5/Al device at different temperatures. The lines represent the linear fits to the experimental data.....84

Figure 3.19 Zero-field mobility as a function of $1/T^2$. The line represents the linear fits to the experimental data.....85

Figure 3.20 Poole-Frenkel γ parameter as a function of $(\sigma/kT)^2$ (GDM). The lines represent the linear fits to the experimental data.....86

Figure 3.21 Poole-Frenkel γ parameter as a function of $(\sigma/kT)^{3/2}$ (CDM). The lines represent the linear fits to the experimental data.....87

Figure 3.22 Room temperature DI transient s under applied bias from 10 – 40 V in step of 5V of APFO Green 5 with device structure of ITO/PEDOT: PSS/APFO-Green 5/Al. Polymer film thickness was 2.33 μm.....88

Figure 3.23 Electric field dependence of charge carrier transit time. The dispersion parameter value α is 0.77 and shown on the plot.....89

Figure 3.24 Semi-logarithm plot of square root field dependence of charge-carrier mobility for an ITO/PEDOT:PSS/APFO-Green 5/Al. The line indicates the linear fit of the experimental data.....90

Figure 3.25 Molecular formula of poly[3-(2'-pentyloxy-5'-(1'''-oxooctyl) phenyl)thiophene] (PPOPT)..... 93

Figure 3.26 Normalized UV-Vis absorption and PL spectra of PPOPT in chloroform solution (a) and in spin-coated film onto quartz substrate (b). The excitation wavelengths were 445 nm and 500 nm, in solution and in film, respectively.....94

Figure 3.27 Cyclic voltammogram of a PPOPT film ((a), first scan) and (b) background, spin-coated onto ITO/glass electrode, in $(C_4H_9)NClO_4$/acetonitrile supporting electrolyte at a scan rate of 100 mV s^{-1}.....95

Figure 3.28 Energy diagram and structure of hole-only devices used in this study..... ...96

Figure 3.29 (a) Conductance spectra for an ITO/PEDOT:PSS/PPOPT/Al device, for dc bias (V_{dc}) values in the range 0 – 10 V and with a step of 2 V. The arrow indicates the direction of increasing V_{dc}. (b) Capacitance spectra for an ITO/PEDOT:PSS/PPOPT/Al device at dc bias of 0 V and 5 V.....97

Figure 3.30 Intermediate-frequency range capacitance (a) and negative differential susceptance spectra (b) for an ITO/PEDOT:PSS/PPOPT/Al device at different dc bias (values shown in the figure).....98

Figure 3.31 Square-root field-dependence of the average hole mobility for an ITO/PEDOT:PSS/PPOPT/Al device. The line represents the linear fit to the experimental data.....99

Figure 3.32 Molecular structure of PFB-co-FT.....103

Figure 3.33 Absorption spectrum (normalized) of thin film PFB-co-FT with the background of sun emission spectrum at AM 1.5.....103

Figure 3.34 Absorption spectra of PFB-co-FT:PCBM films spin-coated on quartz substrates for different D:A weight ratios compared with PFB-co-FT pristine film.....104

Figure 3.35 Effect of solvent on PFB-co-FT:PCBM (1:1w/w) solar cells with different solvents. ITO/PEDOT:PSS/active layer/Al. Thickness of around 130 nm.;

squares indicate maximum values and circles indicate average values on eight cells.....105

Figure 3.36 Effect of thermal annealing on PFB-co-FT: PCBM (1:1 w/w) solar cells ~130nm; annealing time 30 min.....106

Figure 3.37 Efficiency verses Donor to Acceptor weight ratio for PFB-co-FT:PCBM solar cells. Active layers (~120 nm thick) deposited from $CHCl_3$ /Chlorobenzene (1:1 v/v) solutions. Circle average values (on a number of cells between 4 and 8) and square dots maximum values.....107

Figure 3.38 Effect of LiF buffer layer for a PFB-co-FT: PCBM solar cell (1:2 w/w), deposited from a $CHCl_3$/ Chlorobenzene (1:1 v/v) solution to a thickness of ~100n 108

Figure 3.39 Efficiency versus active layer thickness for PFB-co-FT:PCBM (1:2 w/w) solar cells deposited from $CHCl_3$/ Chlorobenzene (1:1 v/v) solutions.....108

Figure 3.40 Short-circuit current(a) and Open circuit voltage (b) as a function of the incident light intensity for a PFB-co-FT:PCBM (1:2 w/w) solar cell, deposited from a $CHCl_3$ /Chlorobenzene (1:1 v/v) solution to a thickness of ~100 nm.....109

Figure 3.41 Typical absorption spectra of BisEH-PFDTBT:PCBM films spin-coated onto quartz substrates for different D:A weight ratios, compared to that of a BisEH-PFDTBT pristine film.....114

Figure 3.42 Photoluminescence quenching of BisEH-PFDTBT:PCBM films spin-coated onto quartz substrates: (a) photoluminescence spectra; (b) PL quenching for

different PCBM weight concentration. The excitation wavelength is 552 nm.....116

Figure 3.43 Current density - voltage curves of ITO/PEDOT:PSS/BisEH-PFDTBT:PCBM/Al solar cells under AM1.5 (100 mW cm^{-2}) irradiation for different D:A weight ratios: 1:1 (squares); 1:2 (circles); 1:3 (triangles); 1:4 (diamonds).....117

Figure 3.44 Series resistance and shunt resistance of ITO/PEDOT:PSS/BisEH-PFDTBT:PCBM/Al solar cells as a function of blend composition.....118

Figure 3.45 (a) Open-circuit voltage of ITO/PEDOT:PSS/BisEH-PFDTBT:PCBM/Al solar cells as a function of the incident light power and for different D:A weight ratios: 1:1 (squares); 1:2 (circles); 1:3 (triangles); 1:4 (diamonds). The lines represent the linear fit to the experimental data. (b) The slopes calculated from the linear fits against the D:A weight ratio.....120

Figure 3.46 (a) Effective photocurrent against the effective voltage of ITO/PEDOT:PSS/BisEH-PFDTBT:PCBM/Al solar cells, under white light irradiation (AM1.5, 100mW cm^{-2}), for 1:2 (circles) and 1:4 (squares) D:A weight ratios. (b) Probability of charge generation at short-circuit condition and at the maximum power point is displayed against the D:A weight ratio.....123

Figure 3.47 (a) The photocurrent curves against the effective voltage and for different thickness: 93 nm (squares); 126 nm (circles); 160 nm (triangles). (b) Maximum possible generation rate of free carriers in ITO/PEDOT:PSS/BisEH-

PFDTBT:PCBM(1:4 w/w)/LiF/Al solar cells as a function of the active layer thickness.....125

Figure 3.48 Probability of charge generation at short-circuit condition and at the maximum power point for ITO/PEDOT:PSS/BisEH-PFDTBT:PCBM(1:4 w/w)/LiF/Al solar cells as a function of the active layer thickness.....126

LIST OF TABLES

Table 2.1 Devices tested with CELIV technique.....58

Table 3. 1. Values of the charge transport parameters obtained by fitting the mobility data using the GDM and CDM models.....87

Table 3.2 Summary of photovoltaic parameters of PFB-co-FT:PCBM solar cells (Averages in parenthesis).....110

Table 3.3 Summary of parameters extracted from the J-V curves of ITO/PEDOT:PSS/BisEH-PFDTBT:PCBM/Al solar cells, prepared with different D:A weight ratios and similar thickness of the active layer.....117

Table 3.4 Summary of parameters extracted from the J-V curves of ITO/PEDOT:PSS/BisEH-PFDTBT:PCBM/LiF/Al solar cells, prepared with the same D:A weight ratio of 1:4 and with different thickness of the active layer.....124

ABBREVATIONS

μ	Mobility
D	Diffusion coefficient
E	Electric field
E_t	Energy of trap state
μ_o	Mobility at zero electric field
γ	Poole-Frankel constant
σ	Energetic disorder
Σ	Positional disorder
a	Interstice spacing between hoping sites
A	Area
S	Rate of change of voltage with time
J	Current density
d	Thickness
τ	Transition time
t	Time
ω	Angular frequency
f	Frequency
G	Conductance
B	Susceptance
Y	Admittance
C	Capacitance

α	Dispersion parameter
α'	Slope of Jsc versus light intensity plot
β	Slope of Voc versus light intensity plot
G_{max}	Maximum generation rate
PCE	Power conversion efficiency
P3HT	Poly-3-hexylthiophene
HOMO	Highest occupied molecular orbital
LUMO	Lowest unoccupied molecular orbital
OPV	Organic photovoltaics
I_{sc}	Short circuit current
V_{oc}	Open circuit voltage
FF	Fill factor
APFO	Alternating polyfluorene
PL	Photoluminescence

1 Fundamentals of charge transport and organic photovoltaic

1.1 Introduction

Polymeric materials, in different forms, have been used by human being since the prehistoric times. However, the polymer science on a molecular basis is the development of the 20th century.

All conventional polymers, called plastics, have been used traditionally because of their attractive chemical, mechanical, electrical insulating properties but not for their electronic properties.

The discovery of semiconductor properties of simple organic molecules like Anthracene in 1960s [1] has opened a new window for application of organic electronics. Since then, many other organic semiconductors have been developed and used in a variety of applications including xerography, light emitting diodes, field-effect transistors, and solar cells [2, 3]. Therefore, there are many organic semiconductors, which have a different property as compared to common insulating organic solids that can be used for many electronic applications. Particularly, the achievement of Alan J. Heegar group [4] in 1977 to improve the conductivity of polyacetylene considered as the biggest turning point for conjugated polymers to be used as electronic devices.

Organic semiconductors, in general, are attractive for use in macroelectronic applications for a variety of reasons. Most importantly, many of them can be dissolved in common organic solvents to form inks which can then be printed over large areas, potentially at great speed and low cost. Moreover they have several features which are unusual for semiconductors: they are extremely flexible and can be semi-transparent or

colored. This raises the potential of integrating organic semiconductors into entirely new formats, such as textile-integrated photovoltaics, or semi-transparent displays.

Another key advantage of working with organic semiconductors is that there are an almost limitless number of them. Compared to inorganic semiconductors, they are very easy to modify or design entirely from scratch. This means that properties such as light emission or absorption could be fine tuned for specific applications.

Alongside their potential advantages, organic semiconductors also pose serious challenges that must be overcome before they can be commercialized in macroelectronic applications. The first is a range of other inorganic semiconductors, such as amorphous silicon and copper indium gallium diselenide, exist that perform better than the organic [5] and huge industries already exist around them. Therefore, organics should have to compete against these incumbents for a market share. In fact, the cost of implementing new manufacturing processes means that organics will actually have to perform better than inorganics to gain substantial market penetration, by offering either cheaper, better, or entirely novel electronic devices.

A second challenge faced by organic electronic devices is the need to improve their lifetimes. Because organic semiconductors transport charges via an energetically excited state, molecules are prone to react with surrounding molecules such as oxygen and water. These reactions change the chemical structure and therefore the electronic properties of the semiconductor, usually with a detrimental effect on the performance of the device [6]. As a result, the performance of the device declines over time. This is a particular issue in optoelectronic applications where energetically unfavorable reactions can be driven by high energy radiation. These days, the lifetimes are most commonly extended by encapsulating the devices with protective membranes that slow the transmission of molecules like water [7].

Another key challenge is the need to improve charge transport which is very critical to electronic applications.

Finally, it should be necessary to point out that the key factor for commercialization of organic devices is not necessarily needed to match the properties (like mobilities) of those inorganic ones. Their novel properties could be enough to penetrate the market as far as their performance is well optimized.

1.2 Charge transport in organic semiconductors

Charge transport has been a subject of interest from the standpoints of both basic science and technology. Particularly, understanding of charge transport properties of organic semiconductors is of fundamental importance for further advancement of electronic and optoelectronic devices.

In conjugated polymers, due to the intrinsic low dimensionality of the system, charge carriers tend to have a strong coupling to the lattice [8]. This factor together with electron – electron correlation effect and other molecular structural details can lead to the formation of various types of excitations in conjugated polymers. For example, solitons (in degenerate ground state structures like polyacetylene), polarons and bipolarons (in non degenerate ground state structures like polypyrole, etc), bound excitons (in strongly correlated systems), electons and holes (injected carriers in semiconducting polymer devices) and free carriers (in fully doped metallic conjugated polymers).

Excitations like solitons, polarons, bipolarons and excitons are spread over several angstroms along the conjugated segment. Furthermore, morphological factors (crystallinity, amorphous nature, intermolecular interaction, etc) and the degree of disorder (both intra and inter-chain) combine with the range of charge carrier species, making the charge transport mechanism in conducting polymers quite complex

compared with the conventional systems. In general, the conjugation length (the extent of the delocalized π-electrons in the polymer backbone), inter-chain interactions, carrier density and degrees of disorder are the most significant parameters, playing major role in the charge transport mechanism in conducting polymers.

Polymer chains may extend through a number of crystallite regions, or they can be folded back on themselves within the crystallite regions; in either case the ordered crystallites are interconnected by amorphous region. A crystalline domain, however, is not perfectly ordered: there are point defects such as chain ends, crosslinks, etc. The overall electrical transport is a superposition of intra-chain, inter-chain, and inter-fiber charge transport mechanisms, Figure 1.1 [10].

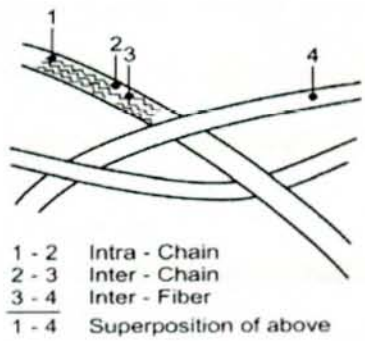

Figure 1.1 Schematic view of the fibrillar structure of polyacetylene [9].

In conjugated polymers, charge carriers can be created by light-induced photocurrent generation, chemical doping and injection of carriers from electrodes in an electric field. The photogenerated and field –induced carriers are transient with short life times, where as the carriers in chemically doped systems are stabilized by the presence of counter ions.

The key quantity that used to characterize the charge transport property of a material is charge-carrier mobility (μ). It is used to evaluate the performances of

organic semiconductor devices such as light-emitting diodes (OLEDs), field-effect transistors (OFETs) or solar cells (OSCs), etc.

In OLEDS a balanced mobility of electrons and holes is required for a better performance [10]. Otherwise, the surplus electrons or holes will not recombine to give the required radiative luminescence, which results in low operation efficiency.

In OPVs a low mobility of charge carriers leads to buildup of space charges due to accumulation of charge carriers in the device which may also enhance the recombination. Moreover, the dissociation of exciton to free carriers decreases and as a result the current density decreases, which in turn decreases the device efficiency. Very high mobility leads to the depletion of the charge carriers and consequently the quasi Fermi levels tend to bend. As a result the open circuit voltage decrease, which decreases the efficiency of the solar cell. Therefore, optimized carrier mobility is an important condition that must be fulfilled to obtain highly efficient organic solar cells [11].

In OFETs a high mobility of the charge carriers leads to a better performance of the device [12].

Therefore, a precise measurement of the mobilities of electrons and holes can give insight into possible limitations for applications. Hence, the knowledge about the physical processes, such as recombination and charge carrier transport, and their impact on the charge collection in semiconductors is crucially important for an optimization and has therefore been intensively studied [13-15].

The transport of charge carriers could be based on diffusion or/and drift mechanisms based on the presence and absence of electric field on the system understudy. In the absence of any external potential, the transport is purely diffusive and the mobility is simply described as

$$\mu = \frac{eD}{kT} \tag{1.1}$$

where μ is mobility, e is unit charge, D diffusion coefficient, k Boltzmann constant, T absolute temperature.

When an external electric field is applied, it induces a drift of charge carriers and the mobility can then be defined as the ratio of drift velocity to the amplitude of electric field:

$$\mu = \frac{v}{E} \tag{1.2}$$

where v is drift velocity of charge carrier and E applied electric field strength.

Drift is the effect that dominates the migration of the charges across an organic layer in the devices [16]. Hence, the drift mobility is used to characterize the mobilities of materials that is to be used in optoelectronic devices.

1.2.1 Charge transport models

Different theories have been proposed to describe charge transport in organic semiconducting materials; however, none of them can explain all experimental observations. Probably, several mechanisms occur at the same time and depending on the specific conditions charge transport is dominated by one of these mechanisms. Hence, a very brief overview of the models that are often used to explain charge transport in organic semiconductors will be discussed bellow.

1.2.1.1 Band transport

In the band transport model intermolecular interactions lead to the formation of energy bands in which electrons and holes can be transported freely. Band transport thus occurs in delocalized states and in a perfect crystal. Therefore, in a perfect crystal a carrier is delocalized and moves as a plane wave without scattering, Figure 1.2a. In a

real crystal, there is always lattice vibration or phonons that disrupt the crystal symmetry. These phonons scatter the electron and thereby reduce its mobility, Figure 1.2b. Since the lattice vibrations are increased at high temperatures, the band transport model suggests that the charge carrier mobility decreases with increasing temperature.

Typically, band transport is observed in inorganic semiconductors, which are highly ordered with strong coupling between the atoms. Most organic semiconductors, however, are characterized by a high degree of disorder and the weak electronic coupling (Van der Waals and dipole-dipole interactions) between different molecules can easily be broken, causing localized instead of delocalized states. Consequently, band transport is generally not the transport mechanism in organic semiconductors. Only for highly ordered molecular crystals such as naphtalene [17], anthracene [18], rubrene [19] and pentacene [20] this behavior, indicated by an increase of the mobility at lower temperatures, has been observed but not for the polymers.

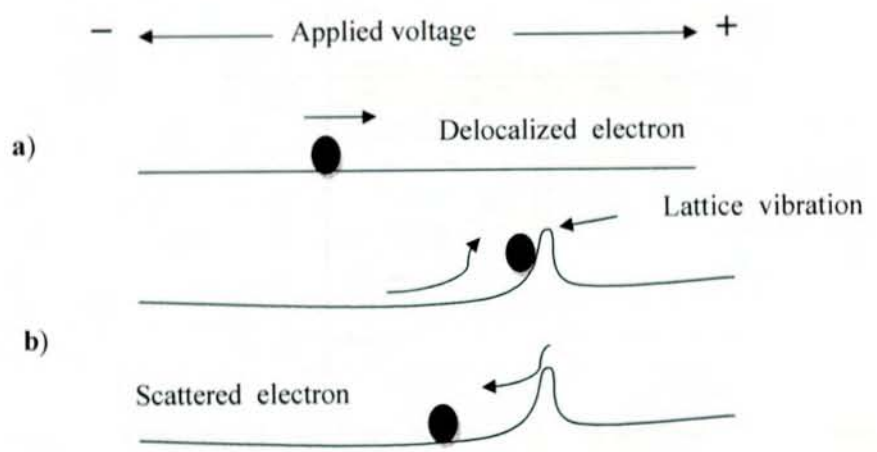

Figure 1.2 Band transport mechanism in solids a) Perfectly ordered crystal b) Real crystal that involves lattice vibration.

1.2.1.2 Multiple Trapping and Release Model (MTR)

The starting point of the model is a distribution of localized levels in the vicinity of a delocalized transport band edge. This model assumes that charge transport occurs through delocalized, extended states. Transport is, however, impeded by impurities, defects, grain boundaries, etc, which create a distribution of traps near the transport band. Traps are, therefore levels localized at lattice defects or impurities in which the charge carriers are immobilized. These traps can be deep traps, which are located near the center of the band gap, or shallow traps, which are located close to the conduction or valence band, Figure 1.3.

During charge transport charge carriers can be trapped. These trapped carriers can then, after a certain time, be thermally released to reach the transport band, where they can be trapped again. The time the carriers are trapped depends strongly on the temperature and on the depth of the trap. The higher the temperature and the shallower the trap, the faster the carriers are released.

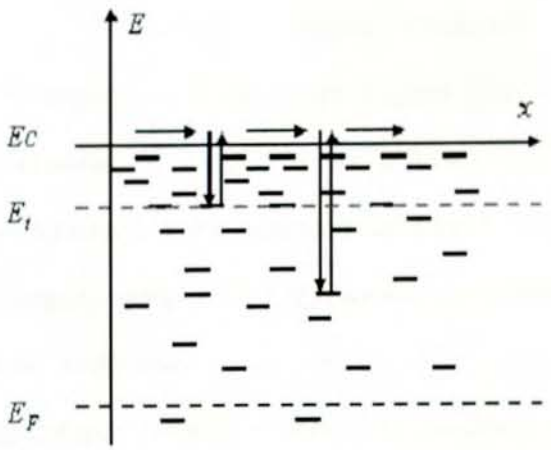

Figure 1.3 Principle of the multiple trapping and thermal release limited charge transport, E_F is Fermi energy, E_t trap energy, E_C conduction energy level [21].

The MTR model predicts an Arrhenius-like temperature dependence of the mobility [22]. In organic semiconductor films the distribution of energy levels below the nominal LUMO or HOMO is to a large extent due to disorder. Therefore, the MTR model has been used quite successfully to describe transport in some of organic films [23, 24]. This model assumes an exponential distribution of gap states. The charges injected or the charges which are already present in the organic semiconductor are trapped into localized states with a probability close to one and then released through a thermally activated process.

The drift mobility is given by:

$$\mu_D = \mu_o \theta \exp\left(-\frac{E_t}{kT}\right) \tag{1.3}$$

where μ_o is the mobility at the band edge, θ is the ratio between the effective density of states at the transport band edge and the density of traps, and E_t is the energy of the trap state.

1.2.1.3 Hopping transport

If the lattice is irregular, or if the carrier becomes localized on a defect site, lattice vibrations are essential for a carrier to move from one site to another. This phonon-assisted tunneling directly between electronically localized centered at different position is known as hopping transport [25]. It is an activated process and the mobility increases with increasing temperature, Figure 1.4.

In the hopping transport model, the mobility of the charge carriers depends on their energy within the density of states distribution and increases if the density of neighboring states (in space) is large, and/or if there are states available at lower energy.

At elevated temperatures, thermal energy is sufficient to overcome small energy barriers. At low temperature, however, transport only takes place via tunneling.

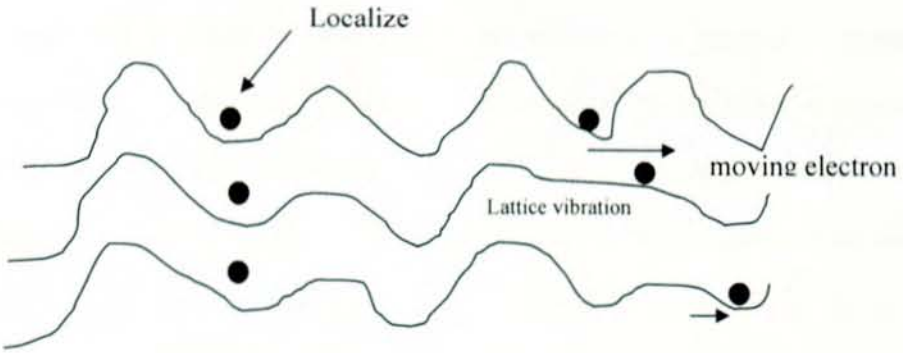

Figure 1.4 Hopping due to lattice vibration transport mechanism in solids.

Organic small molecules or polymer layers often have microstructures that can be characterized as nanocrystalline, or even amorphous. It is generally agreed that the mobility in such dispersed systems is then due to thermally assisted tunneling ("hopping") between localized molecular states [26].

Hopping transport can also be well approximated by a random walk of charge carriers in positionally and energetically disordered landscapes [27]. This typical disorder controlled transport is characterized by considerable activation energy. Charge carrier mobility in such materials are electric field dependent and follows Poole-Frenkel behavior [28],

$$\mu(E) = \mu_o \exp(\gamma\sqrt{E}) \tag{1.4}$$

Where μ_o the mobility at zero field and γ is the parameter describing how strong is the dependence of mobility on electric field.

1.2.2 Charge Carrier Disorder Formalisms

1.2.2.1 Gaussian Disorder Model (GDM)

This model was developed by Bassler [29] and considers the hopping of charge carriers in a lattice of localized states, which are subjected to energetic and positional Gaussian disorder. The energetic disorder, described by the parameter σ, arises from the fluctuations of energy levels, while the positional disorder, described by the parameter Σ, arises from the fluctuations of intermolecular distances or mutual orientations of neighboring molecules. These assumptions lead to the following expression for the electric field E and temperature T dependent charge mobility:

$$\mu_{GDM} = \mu_{inf} \exp\left[-\left(\frac{2\sigma}{3kT}\right)^2\right] \begin{cases} \exp\left[c\left(\left\{\frac{\sigma}{kT}\right\} - \Sigma^2\right)\sqrt{E}\right]; \Sigma \geq 1.5 \\ \exp\left[c\left(\left\{\frac{\sigma}{kT}\right\} - 2.25\right)\sqrt{E}\right]; \Sigma < 1.5 \end{cases} \quad (1.5)$$

Where μ_{inf} is the mobility in the limit $T \rightarrow \infty$ and $E \rightarrow 0$, k Boltzman constant, T absolute temperature, σ width of Gaussian distribution of the energy states, which describes energetic disorder and Σ degree of spatial disorders, *c* an empirical constant and μ_{inf} is the high temperature limit of mobility.

As formulated in the last equation, hopping transport in Gaussian DOS results in $\ln(\mu) \propto T^{-2}$ relationship, which deviates from the Arrhenius behavior $\ln(\mu) \propto T^{-1}$. However, the GDM model has been widely used to explain experimental transport studies in many disordered materials, like organic polymers.

1.2.2.2 Correlated Gaussian Disorder Model (CDM)

Novikov *et al* [30] has proposed a new model called Correlated Gaussian Disorder Model (CDM), in order to circumvent the deficiencies observed between the GDM and the experimental results. One of the reasons for discrepancies arises in GDM

is that it works only in a narrow field range, describing experimental values only in high field range ($E > 3 \times 10^5$ V/cm). The CDM considers spatially correlated energetic disorder as a necessary requirement for improving the GDM model so as to account for the $\ln(\mu) \propto E$ behavior over a broader electric field range. The spatial correlations in disordered materials may originate from long-range charge-dipole interactions. The strong coupling of phonon and electronic states in organic solids rationalizes the inclusion of correlation in transport models.

The new correlated disorder model (CDM) is expressed as

$$\mu_{CDM} = \mu_{inf} \exp\left\{-\left(\frac{3\sigma}{5kT}\right)^2 + C_0\left[\left(\frac{\sigma}{kT}\right)^{3/2} - \Gamma\right]\sqrt{\frac{qaE}{\sigma}}\right\} \tag{1.6}$$

where $C_0 = 0.78$ and $\Gamma = 2$, a is the interstice spacing between hopping sites, q electron charge.

Γ characterizes geometrical disorder and thus should depend upon transport site concentration.

1.3 Charge transport measurement techniques

There are various types of charge carrier mobility measurement techniques. These techniques could be categorized into four groups based on the mechanism of charge carrier generation [31]. They are Photo-generated, Doping generated, Injection generated, and Electric field generated.

Time of Flight (TOF) from photo-generated, Charge Extraction by Linearly increasing Voltage (CELIV) from doping generated, Admittance Spectroscopy (AS), Dark Injection space charge limited current (DISCLC) and Space charge limited current (SCLC) from injection generated have been discussed in more details in this thesis. However, there are other more techniques like Organic Field Effect Transistors

(OFET), Transient Electroluminescence (EL), etc that have been used to determine the mobility of organic semiconductors.

In all cases the sample to be characterized should be prepared as a form of device with different architectures, which will be explained in each respective topic, in order to make characterization simple. In general, in the device development steps, the sample material is sandwiched between electrodes. The device architecture could be designed for a single charge carrier transport i.e. hole or electron only transporting device. In some techniques it is possible to characterize both electron and hole mobility simultaneously such that the devices should be developed to allow both carrier transportation.

For hole only devices, the work function of hole injecting electrode and HOMO level of the semiconductor should be aligned but its LUMO level should be very deep relative to the other electrode in order to block injection of electrons. Likewise for electrons only devices, the LUMO level of the semiconductor should be aligned with the work-function of electron injecting electrode but its HOMO level should be deeper than the work-function of the other electrode in order to block holes. For simultaneous measurement of electrons and holes no need of blocking contact electrodes rather both electrodes should inject charge carriers.

Therefore, it is very crucial to consider the work-function of metal electrodes and HOMO or/and LUMO levels of semiconductors during preparation of devices before conducting the measurement.

1.3.1 Time of Flight (TOF)

TOF is a well known technique and it is widely used to measure the charge carrier transport in various low mobility (and low conductivity) semiconductors. Charge

carrier mobilities in organic materials were first measured with the TOF technique by Kepler and Leblanc [32] and still used as standard method with a lot of improvements.

The apparatuses needed for TOF measurement are LASER light source, electrical potential source, variable resistors and an Oscilloscope, Figure 1.5.

The TOF method is based on the measurement of the carrier transit time (τ), namely, the time required for a sheet of charge carriers photo-generated near one of the electrodes by pulsed light irradiation to drift across the sample to the other electrode under an applied electric field [33].

The TOF method is a rather direct and general measurement technique for determining mobilities of charge carriers in that it directly visualizes their field-induced transit motion through a sample from the start at one electrode to the arrival at the opposite one.

As depicted in Figure 1.5, an organic layer with a few microns thick (d) is sandwiched between two electrodes. The material is first irradiated at the time t_0 by a laser pulse in the proximity of one electrode to generate charges. Initially, both types of charge carriers are generated. This results an initial current spike on current versus time response of the measurement as shown in Figure 1.7.

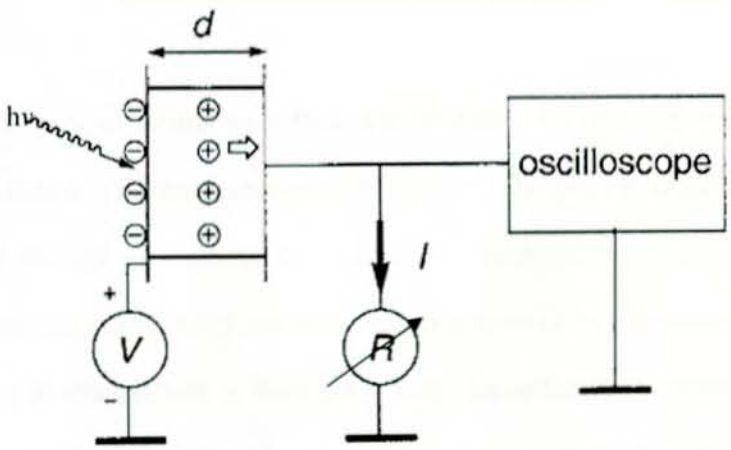

Figure 1.5 Scheme of TOF apparatus.

One species instantly recombines at the respective electrode, depending on the polarity of the applied bias and the corresponding electric field, while the other starts moving at a constant velocity (v) through the bulk of the sample. This uniform movement of the package results in a plateau region in the transient. When it reaches the adjacent electrode, charge carriers from the packet start to recombine accompanied by a drop of the photocurrent, leading to a tail in the transient. The transit time τ is determined from the intersection of an extrapolation of the plateau and a tangent to the tail, Figure 1.6.

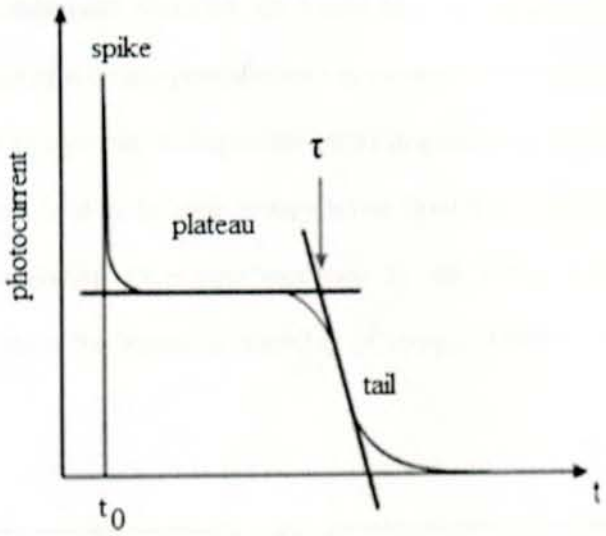

Figure 1.6. Photocurrent versus time response of TOF.

In the case of measuring a hole drift mobility, for instance, the transparent electrode is held at a positive potential with respect to the ground, while the other one is grounded through a resistance R which has a much smaller resistance than the sample. At the beginning, holes and electrons are generated by photo-excitation of the film through irradiation with a short pulse laser. Immediately the electrons will be collected by the positive electrode and the holes will start moving to the negative electrode. When charge carriers start to drift, photocurrents flow until the charge

carriers arrive at the other electrode and the response is shown in Figure 1.7. The response could be either non-dispersive or dispersive types based on the transport mechanism of the charge carriers. A sharp signal is obtained in the case of ordered materials (non-dispersive transport) while in disordered systems a broadening of the signal (dispersive transport) occurs due to a distribution of transient times across the material.

Figure 1.7a shows a typical transient of non dispersive transport while Figure 1.7b shows the photocurrent response for dispersive transport, which is without any definite cusp. In the dispersive transport the transit time, τ, is determined from the double logarithmic plots of transient photocurrents as shown in the inset of Figure 1.7b. This shape is due to a charge trap or dispersion effect in a material, which means that some charge carriers are hold in different energy levels from a transporting level for a certain time during traveling from one electrode to the other. Therefore, TOF measurements clearly show the impact on mobility of structural defects present in the material.

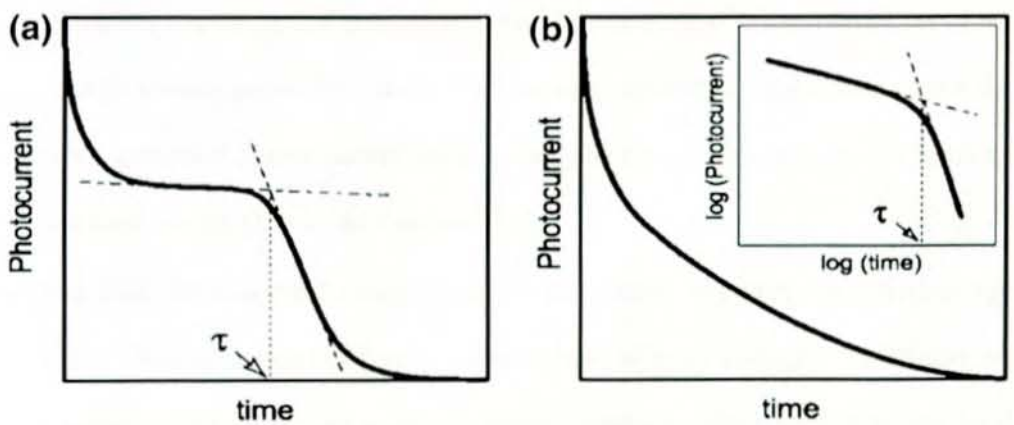

Figure 1.7. Typical transient photocurrents: (**a**) non-dispersive; (**b**) dispersive. *Inset* double logarithmic plot.

The mobility of the holes or electrons is estimated via:

$$\mu = \frac{d}{\tau E} = \frac{d^2}{\tau V} \tag{1.7}$$

where d is the distance between the electrodes, E is the electric field, τ is the averaged transient time, and V is the applied voltage.

One of the advantages of using TOF technique is that the hole and electron mobility can be studied separately simply by changing the polarity of applied voltage.

There are several restrictions to the experimental practice in time-of-flight experiments:

- The film thickness should be very much larger than the thin sheet of carriers width. This is correlated to the absorption profile of the laser beam and limits the applicability of the method to strongly absorbing materials or very thick layers. Therefore, the sample size should be arranged in order to have the light absorption to be within 10% of the sample size. The thickness of samples is usually in the range from 5 to 20 μm.
- The absorption depth of the optical excitation is small compared to the film thickness and the optical pulse duration is short compared to the transit time of the charge carriers across the sample. Low intensity optical pulses are used so that the photogenerated charge carrier density does not significantly perturb the spatially uniform electric field in the structure [34].
- The total photo-injected charge must be very much less than capacitive charge (CV). The total number of created charges must be small enough not to distort the external electric field. As a rule of thumb, less than three percent of the total amount of charges that are stored on the electrodes should be created. This constrains the experiment to low excitation intensities and low electric fields.

- Both electrodes must be non-injecting and form blocking contact.
- One of the electrodes should be semitransparent in order to allow the penetration of laser light into the sample
- The laser pulse width should be very much less than the transit time.
- Carrier recombination time or trapping time should be very much greater than transit time.
- The time constant RC has to be at least one order of magnitude smaller than the transit time to guarantee full time resolution of the transient signal (is necessary to prevent the rising time of the signal from being longer than the transit time τ). It is determined by the capacitance C of the whole setup and the resistance R, caused by the wire connections and the shunt-resistor used to measure the photocurrent with the oscilloscope.

1.3.2 Charge Extraction by a Linearly Increasing Voltage (CELIV)

Another approach to measure charge carrier mobility was introduced by G. Juska *et al.* [35], called Charge carrier Extraction by Linearly Increasing Voltage (CELIV). There are two types of CELIV techniques: Dark-CELIV and Photo-CELIV. In this report the former is only addressed.

In Dark CELIV the charge carriers studied are equilibrium charge carriers, which of course are of great importance for the understanding of steady state transport in optoelectronic devices.

The basic idea of this method is illustrated in Figure 1.8.

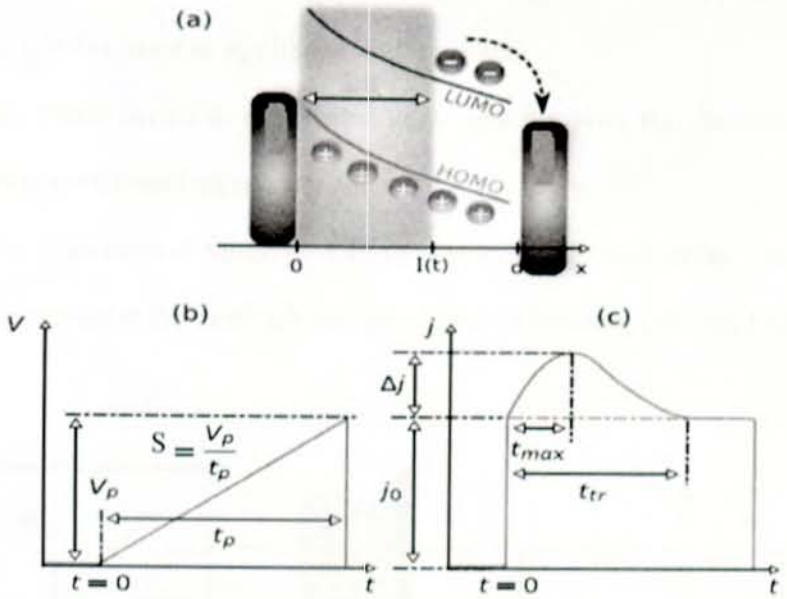

Figure 1.8. A schematic illustration of the CELIV technique. (a) Process of charge extraction. The region $0 \leq x \leq l(t)$ where all electrons have already been extracted is depicted by the shaded area. (b) Scheme of the voltage input and (c) The current density response with capacitive offset Jo and a current density due to drift with maximum of current ΔJ.

Here, a linearly increasing voltage, V(t), is applied on the device that is sandwiched between blocking electrodes, Figure 1.8b.Then, the extraction of charge carriers begins and reaches maximum at t_{max} and correspondingly the current density also reaches maximum, j_{max}. After t_{max} both the charge carrier concentration and the external current density decreases since the charge carriers get depleted in the sample. Therefore, the linearly increasing voltage is used to extract equilibrium charge carriers with density n and mobility μ from a film with a certain dielectric permittivity ε and thickness d.

In CELIV method there is no injection of charge carriers rather than extracting the charge carriers found in equilibrium in the sample.

The whole device is represented as a capacitor with the film between two electrodes at x = 0 (blocking contact) and x = d.

The experimental setup of CELIV involves an oscilloscope and a pulse generator, a sample in the sandwich configuration with blocking contacts, Figure 1.9.

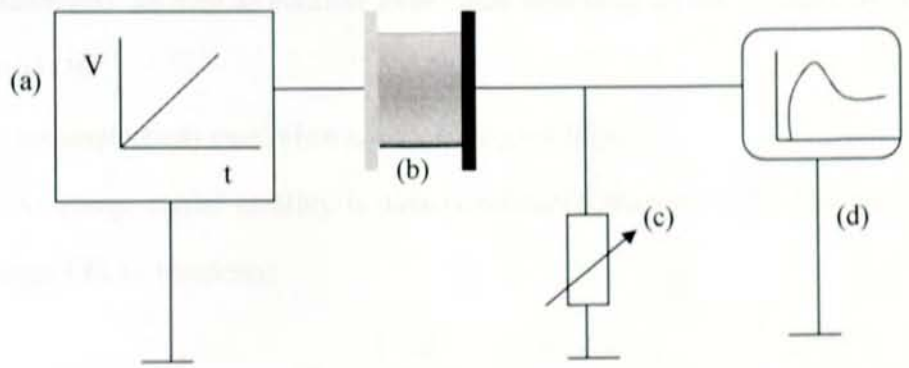

Figure 1.9. Schematic set up of CELIV: (a) function generator, (b) sample sandwiched between electrodes, (c) variable resistor and (d) oscilloscope

In CELIV method, when the density of current as a function of time measured, differentiating RC-circuit current step j(0) is seen in the beginning, Figure 1.8c [33].

$$j(0)=\frac{S}{d}\varepsilon\varepsilon_0 \qquad (1.8)$$

where, $\varepsilon, \varepsilon_0$, are the dielectric constant of the material and vacuum, respectively, S is the slope of the applied voltage pulse and d is the thickness of the dielectric.

The total current density, j(t), with in the sample, due to the redistribution of the charge carriers (electric field) is estimated by [35]:

$$j(t) = \frac{S}{d}\left[\varepsilon\varepsilon_0 + \sigma t\left(1 - \frac{\mu S t^2}{2d^2}\right)\right] \tag{1.9}$$

Where σ is conductivity and the other terms defined previously.

To calculate the mobility based on the transition time (t_{tr}) is difficult since the determination of the transition time from the current versus time curve is not so easy in this technique, Figure 1.8c. Therefore, a relationship of mobility with t_{max} has been developed. Based on this idea, in order to estimate transport parameters from CELIV measurements we need to consider three cases depending on the conductivity of the material [36]:

1. Low conductivity case, when $\tau_\sigma >> t_{tr}$ (or $\Delta j << j(0)$);

   The charge carrier mobility is directly estimated from the extraction maximum from CELIV transients:

$$\mu = \frac{2}{3}\frac{d^2}{St_{max}^2} \tag{1.10}$$

2. High conductivity case, $\tau_\sigma << t_{tr}$ (or $\Delta j >> j(0)$)

The charge carrier mobility is then estimated:

$$\mu = \frac{d^2 j(0)}{St_{max}^2 \Delta j} \tag{1.11}$$

3. Moderately conductivity, $\tau_\sigma \approx t_{tr}$ (or $\Delta j \approx j(0)$)

$$\mu = \frac{2}{3}\frac{d^2}{St_{max}^2 (1 + 0.36\Delta j / j(0))} \tag{1.12}$$

where $(1 + 0.36\Delta j/j(0))$ is the numerically calculated correction factor.

Recently there is a big debate on the value of the correction factor that is used in Equation 1.12. The debate is based on the consideration of the status of charge carriers in the devices. Many papers reported so far has considered the extracted carriers during

CELIV measurement are equilibrium carriers and homogeneously distributed. However some scholars are challenging this idea and suggested that these carriers are not at equilibrium and homogenous [14, 37]. They pointed out that real devices exhibit an inhomogeneous distribution of electrons and holes in the device, with the electron concentration being highest at the cathode and lowest at the anode and vice versa for holes. Therefore, the correction factor 0.36 introduced by Juska *et al* [38] has been replaced by 0.21 by Deibel *et al* [14] and 0.18 by Bange *et al* [39].

Very lately Lorrmann *et al* [40] has come with a new formula that helps to calculate the mobility that is expected to be valid for all cases:

$$\mu = \frac{d^2}{2St_{\max}^2}\left[\frac{1}{6.2\left(1+0.002\frac{\Delta j}{j_0}\right)}+\frac{1}{\left(1+0.12\frac{\Delta j}{j_0}\right)}\right]^2 \tag{1.13}$$

CELIV is simple and easy method to apply. However, it is difficult to determine the type of carrier under measurement. Therefore, there should be a complimentary method that could be used to identify the polarity of charge carrier. Frequently, the TOF method is used for this purpose.

1.3.3 Dark Injection Space Charge Limited Current transient method (DISCLC)

DISCLC transient technique is one of the known methods that have been used for the measurement of mobility in organic electronic materials [34, 41-43]. In this technique the organic layer thickness d is sandwiched between anode and cathode electrodes. Here one electrode should be Ohmic for the charge carrier of interest and the other blocking electrode. A big reservoir of charges for Ohmic injection can be achieved by using a metal electrode that provides a small energy barrier for electron or hole injection and the carriers are injected by a voltage pulse. Therefore, when a

step change in voltage is applied to the device the time-dependent current response can be measured.

For a device having low trap density and short trapping times (or the complete absence of traps), the current rises to a peak above its steady-state value. The idealized response of an organic semiconductor material where the mobility is not field dependent is shown in Figure 1.10.

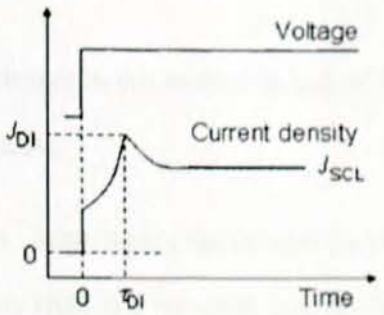

Figure 1.10 An ideal DI-SCLC transient.

If a voltage step is applied at a time t = 0 the measured current density reaches a peak J_{DI} at a time $t = \tau_{DI}$. For $t > \tau_{DI}$, the transient current decays monotonically and asymptotically to a steady-state value of J_{SCL}. The characteristic time τ_{DI} is the arrival time of the fastest carriers at the noninjecting electrode.

τ_{DI} is related to the space-charge free carrier transit time τ_{tr} by approximate relationship [44, 45]:

$$\tau_{DI} = 0.787\ \tau_{tr} \tag{1.14}$$

The mobility and transit time are related by

$$\mu = \frac{d}{\tau_{tr} E} \tag{1.15}$$

And hence

$$\mu = \frac{0.787 d}{\tau_{DI} E} \tag{1.16}$$

injection. Alternatively, if the charge injection remains Ohmic, deviation of this ratio could also be a consequence of non-negligible charge diffusion or field dependent mobilities.

One of the big challenges in this method is lack of Ohmic injecting electrodes and encountered limited success.

1.3.4 Admittance spectroscopy (AS)

Admittance spectroscopy (AS) is a powerful tool for the investigation of charge-carrier transport in high resistivity materials [47].

In this method, we consider a two-terminal device consisting of an organic semiconductor with a dielectric constant ε and a thickness d, sandwiched between two electrodes. One of the electrodes is assumed to form an injecting contact with the organic material. The other contact is blocking. The instruments used and the configuration is shown in Figure 1.11B.

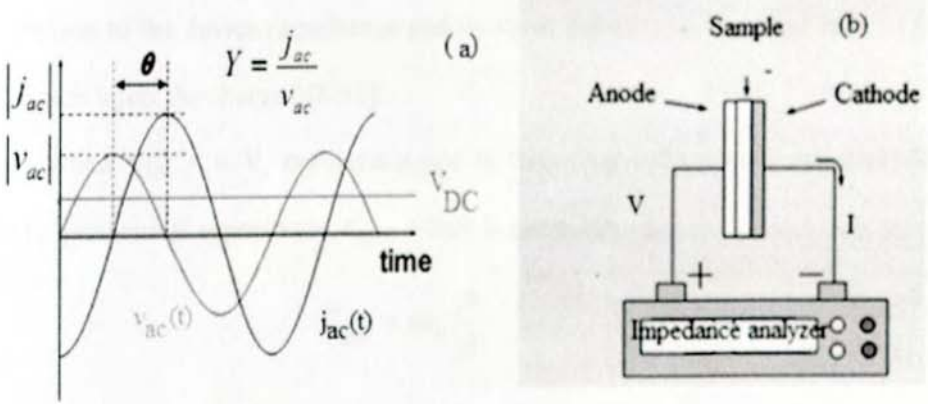

Figure 1.11 (a) the Ac and DC electrical waves; (b) AS configuration.

driven by a small harmonic voltage modulation, v_{ac}, is probed. The amplitude and the phase difference of the ac current, i_{ac}, are monitored as a function of frequency, f, and the frequency dependent admittance, Y(ω), can be obtained as follows:

$$Y(\omega) = i_{ac} / v_{ac} = G(\omega) + i\omega C(\omega) = G(\omega) + iB(\omega) \quad (1.17)$$

Where $\omega = 2\pi f$ is angular frequency, f is the linear frequency, $G(\omega)$ is the conductance, $C(\omega)$ is the capacitance and $B(\omega)$ is the susceptance of the system.

The real part of admittance, i.e. conductance, is related to conduction process within the device, such as translative motion of charge carriers in the device. On the other hand, the imaginary part, i.e. susceptance, is linked with the displacement process, for example due to reorientation of electric dipoles within the material under the electric field.

In admittance spectroscopy, for the characterization of the material mobility the capacitance against frequency response is necessarily monitored, Figure 1.12a. When charge is injected into a material between two electrodes it will result an additional contribution to the device capacitance and its value depends on the magnitude of DC-bias, which inject the charge [48-51].

When V_{DC} = 0 V, the capacitance is frequency independent and essentially equal to geometrical capacitance, C_{geo}, which is given by

$$C_{geo} = \varepsilon\varepsilon_o \frac{A}{d} \quad (1.18)$$

Where C_{geo} is geometrical capacitance, ε dielectric constant of the material, ε_o vacuum permittivity, d active layer thickness and A area.

is due to the finite transit time of carriers across the device at given voltage that result a space charge limited current. Particularly, the portion of charge injected due to AC voltage modulation relaxes into equilibrium space charge and the injected current lags behind the applied AC-voltage, V_{AC}, (due to finite carrier mobility) that reduces the phase of Y. As a result, there is an inductive contribution to C and C exhibits its minimum. However, if the voltage modulation is too fast, $f > \tau_{tr}^{-1}$, the injected charge will not have enough time to reach equilibrium and the original capacitance will be restored.

If there are traps and a subsequent emission of charges from trap states (dispersive transport behavior) exists in the material, this results in an additional positive contribution to the capacitance. The presence of this phenomenon is observed at the extreme lower frequency regions, Figure 1.12 dashed lines. The capacitance due to trapping increases and saturates at low frequencies. But at higher frequencies the release rate from the traps cannot keep up with the voltage modulation and the contribution due to trapping becomes negligible.

In the case of heavy trapping (highly dispersive transport) the capacitance is larger than C_{geo} at all frequencies and the inductive response due to space charge may be totally masked by the excess trapping capacitance. Consequently the transit time cannot be resolved.

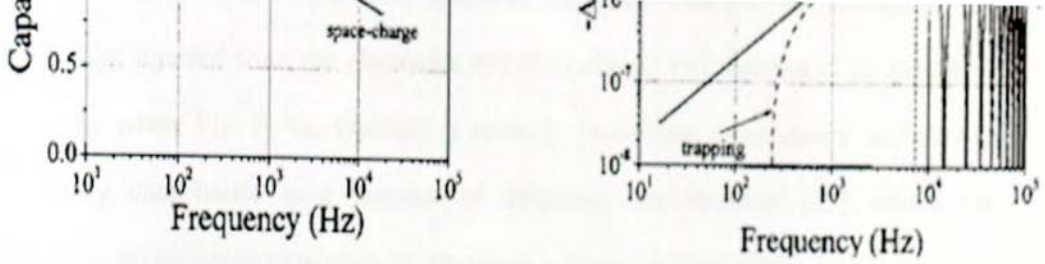

Figure 1.12 (a) A theoretical capacitance spectrum C = ImY /ω. An example of response due to charge detrapping is plotted by the dashed line. (b) The corresponding change of susceptance, −ΔB [52].

The response of capacitance as a function of frequency gives insight about the mobility of charge carrier in the sample. However, it is a little bit challenging to determine the relaxation frequency from capacitance against frequency plot, which is related to the transit time. Therefore, it is suggested to analyze the data by plotting the change in susceptance, −ΔB, as a function of frequency, as it was suggested by Martens *et al* [53], Figure 1.12b, which is given by

$$-\Delta B = -\omega(C - C_{geo}) \tag{1.19}$$

Clearly, −ΔB peaks at a frequency f_{max}, which scales with the corresponding transit time τ_{tr} according to an approximate relation

$$f_{max} \approx 0.54\ \tau_{tr}^{-1} \tag{1.20}$$

The mobility can be determined based on the following relation [54]:

charges are injected from the electrodes and the polymer will behave as an insulator. However, when $V_{DC} > V_{bi}$ typically a strongly increasing conductance and slowly decreasing capacitance as a function of frequency are observed [55], which are signatures of relaxation of permanent dipoles in a disordered material.

Admittance Spectroscopy can also be used to determine the mobility of electrons and holes simultaneously on a single sample [53]. This avoids the possible effect of different preparation conditions, which may occur when analyzing two different structures. This ability of AS makes it more attractive. In this case situation of the recombination of carriers should be taken into account. Therefore, the situation is more complex and depends on the interplay between carrier transit time and the recombination time.

Simultaneous determination of electron and hole mobilities is possible under three main conditions [47]. First, the Schottky barrier heights of the anode and the cathode must be sufficiently low to allow simultaneous injection of both electrons and holes at comparable rates, leading to modulation of electron and hole concentrations inside the organic layer by the applied ac voltage. Second, the recombination rate between electrons and holes must be in an intermediate range. Too strong rates lead to recombination close to the electrodes; therefore there is no transit time effect. Too weak rates lead to electron or hole currents crossing the layer without modulation of the carrier concentration. Third, trap concentrations have to be sufficiently weak such that their contribution to the admittance curves does not mask the susceptance peak

both carrier mobilities will be possible for few organic material.

One of the big advantage of AS over TOF is that it is very effective to determine the mobility of carriers in highly dispersive materials [51]. The AS signals remain clear for mobility determination when deep traps are present, while the TOF transients show highly dispersive characteristics without any indication of the carrier transit time. The other advantage of AS when compared to CELIV techniques is that in the former there is no problem in identifying the type of charge carrier (hole or electron) but in the later case it is very difficult to know without a support of other techniques like TOF.

1.3.5 Space charge limited current

Space charge limited (SCL) techniques are a much used way of measuring the mobility in organic materials. In such techniques the injection of one carrier species is reduced, by careful selection of the electrode materials, while the contacts can inject and extract more carriers than the bulk can carry. The resulting current density is proportional to the charge carrier mobility. In the absence of any trapping effects the current density is given by the Child's Law [56, 57]

$$J = \frac{9}{8}\mu\varepsilon\varepsilon_o \frac{V^2}{d^3} \tag{1.22}$$

The mobility, therefore, can be extracted from the J-V plot of Equation 1.22.

electrode and captured by the other.

3. The carrier mobility and the dielectric permittivity are constant throughout the sample.
4. The electric field at the charge injecting electrode is zero.
5. All current is drift current (diffusion plays no role).

This technique has been applied to neat and blend materials [59]. However, at high applied voltage the mobility increment beyond the quadratic behavior described by Equation 1.22 is often observed. The deviations are due to a field-dependent mobility [60]. Therefore, by using the Poole-Frankel mobility relation, Equation 1.4, Murgatroyd has shown that the resulting SCL current density is given by [61]:

$$J_{scl} = \frac{9}{8}\varepsilon_r\varepsilon_o\mu_o\frac{V^2}{d^2}\exp\left(0.891\gamma\sqrt{\frac{V}{L}}\right) \tag{1.23}$$

This procedure makes possible the quantification of the apparent bias dependence of the mobility, but ignores the density dependence of the mobility and is, therefore, not strictly correct. Hence, for a correct interpretation of current voltage data it might be necessary to correct for the series resistance of the substrate and the built in voltage [62].

energy source these days is fossil fuel that comprises oil, gas and coal. Unfortunately the fossil fuels are not cheap, renewable and environmentally friendly. Therefore, there should be an alternative source of energy which will satisfy these issues.

The alternative energy sources to that of fossil fuels could be hydroelectric powers, geothermal, wind, nuclear power, solar energy, etc. Except the solar energy the other energy sources are either too expensive or not enough to satisfy the high energy demand of human being in the future. In the coming two decades the world needs about 60 terawatts of energy with satisfactory distribution all over the world. But now all energy sources are producing only about 15 terawatts. If we extensively use nuclear energy, the amount of energy that can be produced sum up to 25 terawatts, which is not even half of the required amount. However, the sun strikes the earth with 165,000 terawatts every moment of every day freely and without any cost [63]. Therefore, the sustainable and suitable source of energy of the future would be solar energy.

Even though the solar energy is a free source, conversion of it to the required form of energy (commonly to electrical energy) is a big challenge. There have been many researches attempting to develop efficient solar cell devices (photovoltaic cells), which convert the solar energy to electrical energy [64].

A breakthrough in developing a solar cell was done in 1954 by Pearson *et al* from Bell laboratory, which produced a 6% efficient solar cell based on crystalline silicon with *p-n* junction [65]. This technology now is a matured and long established at the industrial scale. The current efficiency of the crystalline based silicon solar cell is around 24% [66] and nowadays, it is the primary solar cell source worldwide.

approaches are under study to address issues related to crystalline silicon based solar cells. One of these is application of thin film based solar cells.

Thin-film technologies, which can use inorganic semiconductors, organic dyes or organic polymers, are nanometers to a few micrometers thick, and can be applied in continuous industrial production using, for example, vacuum deposition, sputtering and printing. Thin films also use fewer raw materials compared with silicon wafers, and so cut costs [68].

Among the categories of thin film solar cells, the organic photovoltaics gets more attention because of their ease of processing, mechanical flexibility, light weight and potential for low cost fabrication of large areas [69, 70]. Additionally, their material properties can be infinitely tailored by modifying their chemical structure [71, 72], even tuning of their color is possible, resulting in greater customization than traditional solar cells.

Today three different types of organic solar cells are known: small molecule solar cell, polymer solar cell and dye-sensitized solar cell (Grätzel cell). Small molecule solar cells are processed in vacuum by physical vapour deposition, whereas polymer solar cells are processed by spin-coating or ink-jet printing. Grätzel cells contain a highly porous layer of titanium dioxide as electron transport layer on which dye molecules are adsorbed. It is typically processed by coating of the titanium dioxide with subsequent sintering and dying.

Many years of research have been done on the organic solar cells and its efficiency remained below 0.1% for a long time, making them unsuitable for any

cells: dye-sensitized solar cells [74]; planar organic semiconductor cells (bilayers) [75]; and high surface area, or bulk heterojunction cells [76].

Another revolutionary development in organic photovoltaics came in the mid 1990s with the introduction of the dispersive (or bulk) heterojunction, where the donor and acceptor material are blended together. The ultrafast photoinduced electron transfer from a conjugated polymer as donor to buckminsterfullerene (C_{60}) or its derivatives as acceptor was first observed in 1992 by Sariciftci *et al* [77]. Since then this material combination has been extensively studied in bulk heterojunction photovoltaic cells. In 1995 Yu et al [76] fabricated the first fully organic bulk heterojunction cell based on a mixture of soluble PPV derivative with a fullerene acceptor such as C_{60} derivative PCBM [78]. In 2001 Shaheen et al [79] obtained the first truly promising results for bulk heterojunction solar cells when mixing a conjugated polymer such as MDMO-PPV with PCBM in a 20:80 weight percentage and optimizing the nanoscale morphology of the film, yielding a power conversion efficiency of 2.5%.

Recently, power conversion efficiencies of of 8.3 % (certified) [80] and over 9 % (uncertified) [81] have been reported for bulk hetrojunction organic solar cells.

1.4.2 A tendency towards Bulk heterojunction Organic Solar cells

There are different architectures of conjugated polymer based organic solar cells. The early attempts used an organic semiconductor as a direct replacement for inorganic semiconductor in the conventional solar cell and it is called single layer photovoltaic cell, Figure 1.13a. It can be made by sandwiching a thin film of polymer between two

of charge a battery.

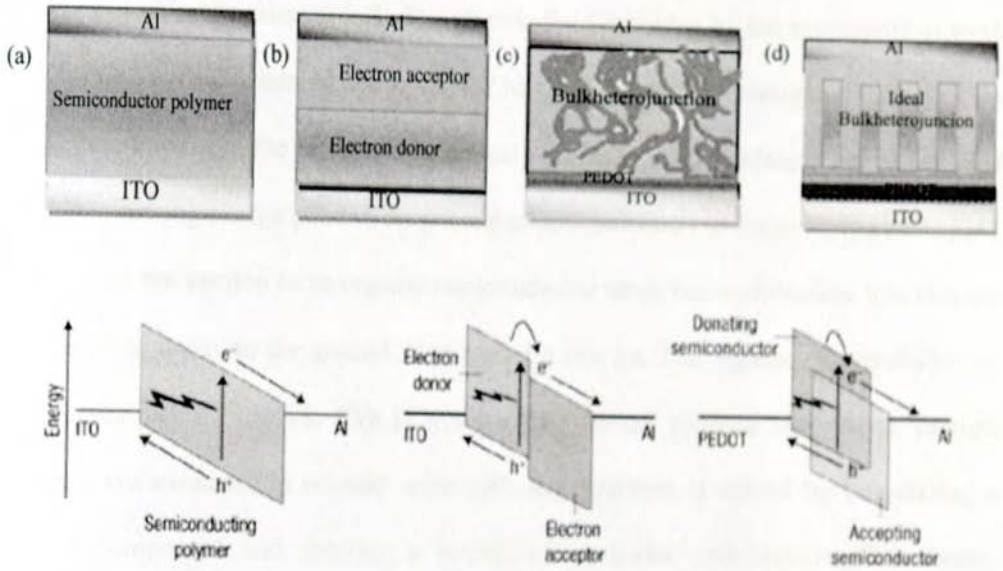

Figure1.13 Different architectures of thin film organic solar cells and their corresponding charge generation and transfer. (a) A single-layer (b) Bi-layer (c) Bulk heterojunction solar cell.

However, the efficiency of this single layer architecture organic photovoltaic cell remained very poor. Therefore, organic solar cells with only one semiconductor do not work well in practice. This is because, in organic solar cells, the photoexcited electron is electrostatically bound to the hole left in the valance band and together they constitute exciton [82]. The formation of excitons is the most important feature that distinguishes organic from inorganic semiconductors. The excitons are neutral and

4) of organic semiconductors makes it difficult for the exciton to dissociate into a separated electron and hole, since the Coulomb energy binding such localized charges is high (~1 eV) compared to k_BT. The electric field provided by the asymmetrical work function of the electrode is not sufficient to break up these photo-generated excitons [83]. In comparison, the exciton in a crystal of silicon has a binding energy of around 0.1 eV, allowing charge pairs to be generated spontaneously at room temperature [84]. As a result, the exciton in an organic semiconductor tends not to dissociate into charges but rather to decay to the ground state within a few ns. The organic photovoltaics are sometimes called excitonic PVs [85] since they do not produce free charge carriers rather gives excitons. In organic solar cells this problem is solved by introducing a second component and forming a hetrojunction device architecture. This second component should act as electron acceptor and has a higher affinity for electrons and a lower conduction band [73], Figure 1.13b. If the exciton is formed near the interface, the electron can transfer to this second (electron accepting) semiconductor and travel to the positive electrode. The hole can then travel in the donor semiconductor to the negative electrode. Therefore, the hetrojunction is necessary to separate the light generated excitons.

The polymer film typically needs to be at least 100 nm thick to absorb enough light. However, the excitons diffusion length is too short (ranges 4-20 nm [86]) and they cannot diffuse across a film this thick to find the interface. Rather they typically decay when diffusing in a polymer before separation into free carriers. The useful strategy is to interpenetrate the two polymers throughout the film so that there are more

In bulk heterojunction the electron donor (conjugated polymer) and the electron acceptor are randomly interspersed throughout the film. As a result there are possibilities to have dead ends or isolated components, which are not in contact with the respective electrodes in the bulk. These isolated components could act as charge carrier traps or sinks, which decreases the overall efficiency of the cell. Based on this fact an ideal architecture of bulk heterojunction is suggested as shown schematically in Figure 1.13d.

In the ideal device structure every exciton formed on the conjugated polymer will be within a diffusion length of an electron acceptor. Additionally, in the ideal structure both the conjugated polymer and electron acceptor should have straight pathways to the electrode to minimize the carrier transport time and reduce the probability of back electron transfer. The ideal structure should be designed so that each phase of the bulk heterojunction is only in contact with one of the electrodes, which would help ensure a high shunt resistance through the device and prevent carrier loss at the wrong electrodes, although to some extent this requirement can be mitigated through the use of highly selective contacts [86].

1.4.3 Basics of Bulk heterojunction organic photovoltaic

Organic solar cells are made on supporting substrate (glass, plastic, etc.) typically coated with a conducting material that will serve as an electrode. This electrode is normally coated with a conducting polymer (e.g. (poly(3,4-ethylenedioxythiophene)-polystyrene sulfonate) PEDOT-PSS) and then coated with the

indium doped tin oxide (ITO). However, due to the scarcity of indium, constant price increases and brittleness of the ITO when deposited onto flexible electrodes it is a challenge to use in the future.

There are at least five fundamental steps takes place in organic solar cells [87] : (1) photons are absorbed in the donor (acceptor) and excitons are created; (2) excitons diffuse within the donor (acceptor) phase; (3) if the excitons encounter an interface with the acceptor (donor) before decaying, then fast dissociation takes place, leading to charge generation; (4) charge carriers are transported to the electrodes via diffusion and/or drift processes; (5) charge carriers are collected at the electrodes, Figure 1.14.

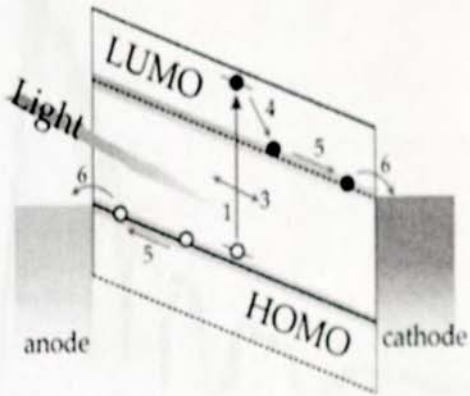

Figure 1.14 Schematic band diagram of a bulk heterojunction. The numbers refer to the operation processes explained in the text. The dashed line represents the energy levels of the acceptor, while the full lines indicate the energy level of the donor in the PV cell.

therefore a layer thickness of just a few hundred nanometers is sufficient to absorb all of the light at the peak absorption wavelength. However, band gaps tend to be relatively large and absorption bands tend to be relatively narrow (compared to inorganic semiconductors) and, therefore, only a small fraction of the solar spectrum is absorbed, Figure 1.15. Moreover, there is typically a mismatch between the material absorption spectrum and the solar spectrum: the photon flux of the AM1.5 solar spectrum peaks at around 700 nm (1.8 eV) while most common donor polymers have absorbance peaks at higher energies.

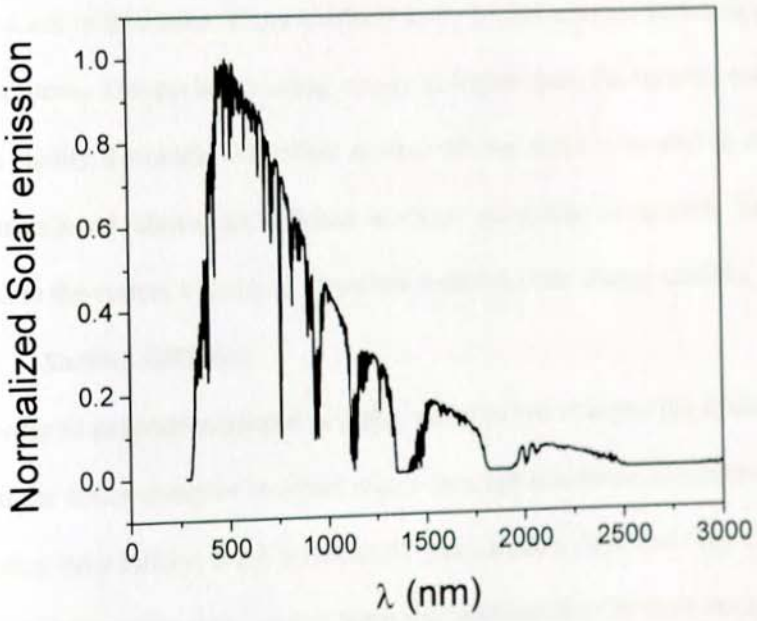

Figure 1.15 Sun flux.

(c) using an acceptor molecules that absorb in the visible region

(d) reduction of reflection losses by using different mechanisms like coating anti-reflectance or structuring the interface.

It is important to note that using a thicker polymer is not a useful strategy as this increases the resistance loss due to the typical low charge carrier mobility present in the organic polymers.

After absorption of the incident light photoexcitation of donor material occurs i.e electrons excite from the ground state to the excited state and holes generated on ground state. However, the hole and electron are generated bound by their Coulomb attraction but not in free state. These Coulombically bound electron and hole pairs are known as excitons. The exciton binding energy is higher than the thermal energy and they cannot readily dissociate. Therefore another driving force is needed to dissociate them. As mentioned above, an efficient electron accepting component has to be introduced into the system in order to dissociate them into free charge carriers.

2. Exciton diffusion

In order to generate separated negative and positive charges, the excitons need to diffuse to the donor–acceptor interface where they can dissociate. Since excitons are neutral species, their motion is not influenced by any electric field and they diffuse via random hops; importantly, they need to reach the interface prior to their decay back to the ground state.

polymer–fullerene devices is ultrafast, around 40–45 fs [89, 90], and in this time regime there is no competing decay process for the optically excited electron–hole pair.

The details of dissociation, however, are still subject to debate. The elementary steps involved in the pathway from photoexcitation to the generation of free charges are shown in Scheme 1.1[71, 91].

It has been proposed that the exciton directly dissociates into free charge carriers because the excess photon energy after exciton dissociation is used to separate the bound pair at the interface. On the other hand, there is evidence that charge transfer forms a bound pair (geminate pair), which can then either dissociate or recombine, Scheme 1.1steps 3 and 4.

The relevant factor for the occurrence of step 3 is the alignment of the energy levels of the participating molecules. Only if the offset between the LUMOs (for electron transfer) or the HOMOs (for hole transfer) of donor and acceptor is large enough to overcome the coulombic attraction between the charges, charge separation will be possible.

Photogenerated excitons in the donor side will dissociate by transferring the electron to the LUMO level of the acceptor and retaining the positive charge, while those created in the other side will transfer the hole to the HOMO of the donor while retaining the negative charge. This step leads to the formation of free charge carriers [92]. The amount of the energy offset necessary to dissociate the excitons is 0.3 – 0.5 eV [93].

$$[D^{*}, A] \rightleftharpoons [D^{\cdot+}, A^{\cdot-}] \quad (3)$$

$$[D^{\cdot+}, A^{\cdot-}] \rightleftharpoons D^{\cdot+} + A^{\cdot-} \quad (4)$$

Scheme 1.1 Elementary steps in the process of photoinduced charge separation for a donor (D) and an acceptor (A): 1) Photoexcitation of the donor; 2) diffusion of the exciton and formation of an encounter pair; 3) electron transfer within the encounter pair to form a geminate pair; 4) charge separation.

The generation rate and the extent of generation of free e-h pairs can be studied by analyzing the photocurrent density (J_{ph}) under reverse bias condition [83, 94].

In the case of an ideal solar cell (no recombination and space-charge formation), the photocurrent can be taken as a direct measure of the photogeneration of free charge carriers [83]. In this case the internal field in the device is given by

$$E = \frac{(V_{oc} - V)}{d} \quad (1.24)$$

Where V is the applied voltage, V_{oc} is the open-circuit voltage, and d is the thickness of the active layer.

The photocurrent for a charge carrier is then given by

$$J_{ph} = ep\mu E \quad (1.25)$$

where μ is the mobility and p is the density of the photogenerated carrier.

the device before recombination and their life time becomes equal to the transit time,

$$\tau = \frac{d^2}{\mu V} \tag{1.27}$$

From this the photocurrent through the external circuit is simply

$$J_{ph} = eGd \tag{1.28}$$

This indicates that the photocurrent is independent of applied voltage and mobility (because the carrier life time is will always exceed the transit time in situations where there is little or no recombination).

However, Hughes and Sokel pointed out that Equation (1.28) is not valid at low bias voltages because diffusion currents have been neglected [95]. Considering the diffusion process, the photocurrent is given by the following analytical solution:

$$J_{ph} = eGd\left[\frac{\exp(eV/kT)+1}{\exp(eV/kT)-1} - \frac{2kT}{eV}\right] \tag{1.29}$$

where eGd is a saturated photocurrent, k Bolzmann constant and T is temperature.

Experimentally, the current density is measured in the dark (J_D) and in illumination (J_L) under reverse bias. The effective photocurrent is, therefore, given by

$$J_{ph} = J_D - J_L \tag{1.30}$$

Then the J_{ph} will be plotted on double logarithmic scale against the effective voltage across the device, given by (V_o-V), where V_o is compensation voltage defined as the voltage where J_{ph} is zero (J_L=J_D). The photocurrent increases linearly with effective voltages at low voltages and subsequently tends to saturate. The linear behavior at low

At the voltages where the photocurrent saturated, all bound e-h pairs are separated and the maximum photocurrent is achieved.

By comparing the photocurrent with the experimentally observed J_{sat} the dissociation efficiency can be determined. The dissociation efficiency at short circuit condition (V = 0), for instance, can be calculated as the ratio of J_{sc} to J_{sat}.

4. Charge transportation

Following exciton dissociation, electrons are found in the acceptor phase whereas holes remain in the donor phase. Subsequently, the electrons and holes must be transported from the D/A interface towards the respective electrodes to produce photocurrent.

Current density (J) in OPVs is composed of a drift and a diffusion component. Depending on the morphology of the D–A interface relative to the electrodes, either diffusion or drift might dominate. For instance, in planar bilayers diffusion current is very important and photocurrent can still be observed even in flat band conditions, allowing open circuit voltage values that can be higher than the difference in work function of the metal electrodes [96]. On the other hand, for a pure bulk-heterojunction device, where the donor–acceptor interfaces are randomly distributed in space, the net diffusion current is small and the drift component dominates. Obviously, the relative importance of the diffusion current will strongly depend on morphology, which often contains dead-ends and intricate pathways of each component to the respective electrode.

Efficient charge transport is important as it will be in competition with interfacial recombination, and will therefore limit device thickness.

In terms of the charge transport mechanism, hopping is usually the basis of all proposed models due to the localized nature of the charge carriers.

5. Charge extraction

Once charges reach the electrode they need to be extracted with minimum loss. The simplest picture for charge extraction would be a hopping or tunneling step, from the organic material (HOMO level for holes and LUMO level for electrons) to the Fermi level of the electrode. The latter process dominates for large energy barriers and low temperatures; while, at room temperature, thermionic emission over the barrier is normally used to describe transport characteristics [97]. However, in real devices charge extraction is a much more complex problem, due to the morphological and chemical nature of the organic–electrode interface.

1.4.4 Device performance characterization [98]

The photovoltaic cell can be modeled as a current source in parallel with a diode. When there is no light it behaves like a diode. Mostly the equivalent circuit of organic solar cells, like the conventional p-n solar cells, approximated to contain

(A) a diode with a reverse saturation current density, J_o;

(B) a current source, J_{ph}, which corresponds to the photocurrent upon illumination;

(C) a series resistance, R_s, which takes account of the finite conductivity of the semiconducting material, the contact resistance between the semiconductors and the adjacent electrodes, and the resistance associated with electrodes and interconnections;

(D) a shunt resistance, R_{sh}, which takes into account the loss of carriers via possible leakage paths like pinholes in the film or recombination centers introduced by impurities, Figure 1.16.

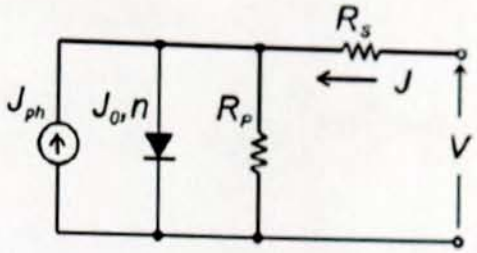

Figure 1.16 Equivalent circuit used to model solar cell.

Solving for this simple circuit provides the following analytical expression for the current-voltage characteristics, referred to as the Shockley equation:

$$J = \frac{1}{1 + R_s / R_{sh}} \left[J_o \left\{ \exp\left(\frac{V - JR_s A}{nkT / e} \right) - 1 \right\} - \left(J_{ph} - \frac{V}{R_{sh} A} \right) \right] \qquad (1.32)$$

where J_o is the saturation current, e the elementary charge, kT the thermal energy, A the area of the cell, n the diode ideality factor, V the applied voltage, R_s the series resistance, R_{sh} the shunt resistance, and J_{ph} the photocurrent.

The current –voltage curve of an illuminated and dark photovoltaic cell has been shown in Figure 1.17.

1. Short circuit current density (J_{sc})

The short circuit current density corresponds to the short circuit condition when the impedance is low and is calculated when the voltage is zero. It is the maximum current that can be produced by the cell.

By analyzing Equation 1.32 the J_{sc} will be

$$J_{sc} = \frac{1}{1 + R_s / R_{sh}} \left[J_o \left\{ \exp\left(\frac{|J_{sc}| R_s A}{nkT / e} \right) - 1 \right\} - J_{ph} \right] \approx -J_{ph} \qquad (1.33)$$

2. Open circuit voltage (V_{OC})

The open circuit voltage occurs when there is no current passing through the cell, and it is the maximum voltage that can be obtained by the system.

From Equation 1.32 the V_{oc} will be:

$$V_{OC} = n\frac{kT}{e}\ln\left\{1+\frac{J_{ph}}{J_o}\left(1-\frac{V_{OC}}{J_{ph}R_{sh}A}\right)\right\} \approx n\frac{kT}{e}\ln\left\{1+\frac{J_{ph}}{J_o}\right\} \qquad (1.34)$$

In Equation 1.33 and 1.34 the approximations are made for the cases where R_s is very small and R_{sh} is very large so that their impacts can be ignored.

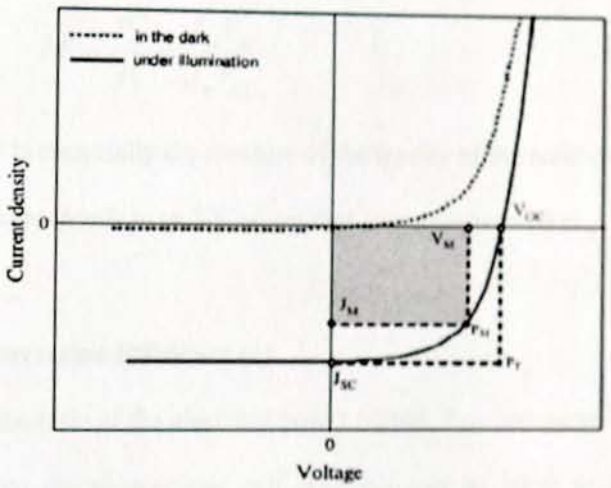

Figure 1.17 Typical current–voltage characteristics for dark and light current in a solar cell. J_{sc} is the short-circuit current density, V_{OC} is the open circuit voltage, J_M and V_M are the current and voltage at the maximum power point.

3. Maximum power (P_{Max})

The power produced by the cell can be easily calculate along the I-V sweep by the equation P = IV = JVA. At the J_{sc} and V_{oc} points, the power will be zero and the

maximum value for power will occur between the two. The voltage and the current at this maximum power point are denoted as V_M and J_M respectively, Figure 1.17.

Therefore,

$$P_M = I_M V_M = J_M V_M A \tag{1.35}$$

4. Fill Factor (FF)

The fill factor can be calculated by comparing the maximum power (P_M) to the theoretical power (P_T) that would be output at both the open circuit voltage and short circuit current together.

$$FF = \frac{P_M}{P_T} = \frac{J_M V_M}{J_{sc} V_{OC}} \tag{1.36}$$

The fill factor is essentially the measure of the quality of the solar cell. A larger FF is desirable, and corresponds to an I-V sweep that is more square-like.

5. Power Conversion Efficiency (η)

Efficiency is the ratio of the electrical power output, P_{out}, compared to the solar power in put, P_{in}, into the photovoltaic cell. The P_{out} can be taken to be P_M (the maximum power from the cell), since the solar cell can be operated up to its maximum power output to get the maximum efficiency.

$$\eta = \frac{P_{out}}{P_{in}}$$
$$\Rightarrow \eta_{\max} = \frac{P_M}{P_{in}} = \frac{J_M V_M}{P_{in}} = FF \frac{J_{sc} V_{OC}}{P_{in}} \tag{1.37}$$

1.4.5 Optimization of bulk heterojunction solar cells

There are many factors that affect the performance of organic solar cells [71, 89, 99]. Therefore, in order to get a better performance different parameters are considered and optimized: proper selection of Donor and Acceptor components (consideration of electronic structure), Donor to Acceptor ratio, active layer thickness, solvent and thermal annealing, and using buffer layer underneath of hole/electron collector electrode. The change of these parameters could bring in improvement of electronic properties, the nanomorphology or/and the electrical contacts of the device under study.

During improvement of the nanomorphology of the device we have to give due attention to the properties of the excitons and the mobility of the charge carriers in the device. The lifetime of the exciton is short and its diffusion length in organic materials is only about 10 – 20 nm. This means that the exciton must reach the D/A interface to give the charge transfer without undergoing to a radiative or nonradiative decay. Thus, the donor and acceptor phases should self-organize to form nanodomains with dimensions comparable to the exciton diffusion length. To increase the possibility for the exciton to reach the interface, the donor-acceptor contact area must be as large as possible. In other words, the size of the domains should be as small as possible, preferably at molecular level [77] so that the donor–acceptor interface is large [76].

Furthermore, once the exciton is formed and dissociated, the hole and the electron must drift to the electrodes within their lifetimes. Again, the phase morphology is critical to form percolated pathways to the contacts.

Electronic structure of components

Figure 1.18 shows how the electronic structures of donor and acceptor affect the photovoltaic parameters of devices. The J_{sc} decreases with the increase of bandgap (less

absorption). Whereas the Voc scales with the difference between HOMO level of the donor and the LUMO level of the acceptor.

It was suggested that for polymer:PCBM solar cells the maximum Voc value can estimated with [100]

$$V_{oc} = (1/e)\left(|E_{HOMO}^{Donor}| - |E_{LUMO}^{Acceptor}|\right) - 0.3V \qquad (1.38)$$

Where e is elementary charge, the acceptor is PCBM with LUMO level of – 4.3 eV and 0.3 V is empirical factor.

More recently, based on measurements of the energy of charge transfer states and relating to V_{oc} of different donor: acceptor blends, an equation has been developed to estimate the maximum open circuit voltage for any BHJ [101]:

$$V_{oc} = (1/e)\left(E_g - 0.6\ eV\right) \qquad (1.39)$$

In order to get efficient exciton dissociation an offset energy (ΔE_{LUMO} and ΔE_{HOMO}) of 0.3 – 0.5eV is required [102].

In general, a proper combination of donor and acceptor has to be chosen to maximize the power conversion efficiency.

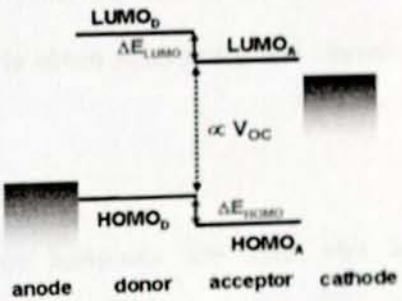

Figure 1. 18 Energy level diagram of solar cell components.

Donor to Acceptor ratio

As for electron donors, a wide range of different conjugated polymers and oligomers have been studied. However, for acceptors, fullerenes are the bench marks of

these days organic solar cells. Particularly, [6,6]-phenyl-C_{61}-butyric acid methyl ester (PCBM) and [6,6]-phenyl-C_{71}-butyric acid methyl ester(PC70BM), Figure 1.19, have been extensively used.

Figure1.19 Molecular structures of [6,6]-phenyl-C61-butyric acid methyl ester (PC60BM) and [6,6]-phenyl-C71-butyric acid methyl ester (PC70BM).

Fullerenes have a set of truly unique characteristics such as high electron affinity as well as high electron mobility that make them very good acceptor components in BHJ solar cells. Importantly, the photoinduced electron transfer from excited donors is orders of magnitude faster than back-transfer or exciton decay.

The addition of fullerenes assists the electrons transfer. In the other hand, increasing the concentration of fullerene decreases the absorption coefficient of the polymer/fullerene blend, leading to lower photoinduced charge generation and hence lower device efficiency. Therefore, the ratio of the electron donor to the electron acceptor must be optimized to obtain maximum power conversion efficiency of the system.

Thickness

The thickness of the composite film must also be optimized. The photoinduced carrier generation in a thin film is low due to low absorption by the composite. A thick film provides high photo-induced carrier generation due to the high absorption by the composite but low efficiency due to the higher resistance of the layer. The photoinduced charge separation also depends on the mobility of the charge carrier in the polymer material.

Annealing

Annealing, in general, improves the nanomorphology of the device. The annealing could be done either with solvent or/and thermal annealing.

Solvent annealing

Solvent annealing is done by exposing the solar cell device before the top electrode deposition on the film of the active layer to less volatile solvent vapor. It is believed that solvent annealing induces the polymer self organization into ordered structure, resulting a better absorption and hole mobility [103].

When the active material is exposed to solvent vapor, the solvent molecules can penetrate into the film and increase the space between polymer chains, the chains become more mobile and self organization can occur to form ordering. As a result the Jsc increases and consequently the power conversion efficiency increases.

Thermal annealing

Thermal annealing is heating of active material above the glass transition temperature and it is usually done as post production process.

Optimal post-production annealing provides two main morphological effects: enhancement of polymer crystallinity, leading to increased absorption and improved charge carrier transport, and diffusion of the components (like PCBM) leading to an increase of the phase separation [104,105].

As a result of heating, the morphology of the organic active layer can be improved by reducing the free volume and the density of the defects at the interface during the evaporation of the solvent [106] and by enhancing interchain interaction [107].

It has also been also reported on the positive influence of subjecting the polymer film to heat treatment to enhance the quantum efficiency of the charge

generation due to the change of morphology at the interface between polymer and electrode[108].

It was observed that annealing lead to a considerable improvement in the solar cell parameters. However, there is an optimum combination of annealing time and temperature beyond which the device parameters rapidly degrade.

The improvement in the device is due to the formation of a structurally better ordered donor phase with a stronger interchain reaction [109, 110]. Beyond a certain temperature there could be a reduction in the values of J_{SC} and V_{OC}. This deterioration can be attributed to the fact that at high temperatures the fullerene molecules can diffuse much easier within the polymer matrix forming large nanocrystals. At higher annealing temperatures, there is also a probability of degradation of the contacts. Besides this when the devices are annealed at higher temperatures, the excess solvent and water is released which may rupture the top aluminum contact layer thereby further degrading the contact.

Buffer layers

The addition of a buffer layer at the ITO–polymer/fullerene composite interface and the polymer/fullerene composite–Al interface helps in improving the device efficiency [111].

PEDOT: PSS is known as a p-type semiconductor, a good hole transport material, and assures a better hole collection from the polymer/fullerene composite layer on to the ITO electrode. The PEDOT: PSS spin coated on to the ITO, smoothens its surface and therefore any possible short circuiting due to the spiky roughness of the surface is prevented.

A thin LiF layer between the polymer/fullerene blend and the aluminum layer increases both the open-circuit voltage and the fill factor of the device, yielding

increased power conversion efficiency. Several mechanisms have been suggested including lowering of the effective work function of the aluminum; dissociation of the LiF and subsequent chemical reaction (doping) of the organic layer; formation of a dipole layer leading to a vacuum level offset between the organic layer and the Al; and protection of the organic layer from the hot Al atoms during thermal deposition. But all of them are under debate.

1.4.6 Effect of illumination intensity on short circuit current and open circuit voltage

The study of light intensity dependence of short circuit current and open circuit voltage of BHJ solar cells could help to understand the loss mechanisms of the device.

a) Intensity dependence of Jsc

Several authors have reported a power law dependence of Jsc upon light intensity, I, [112-118] i.e.

$$J_{sc} \propto I^{\alpha'} \tag{1.40}$$

where α' ranges typically from 0.85 to 1 for polymer/fullerene based solar cells [119].

The interpretation of the exponent α' varies in literature. The deviation from α' =1 has been conjectured to arise from a small loss of carriers via bimolecular recombination [88,117,118]. In the contrary Koster et al has demonstrated that bimolecular recombination does not account for the observed variation of α' from one, but that the true cause lies in the buildup of net space charge due to imbalanced transport of charge carriers[119]. However, Heeger *et al* has emphasized that α' = 1 when all carriers are swept out prior to recombination and collected as a current in the external circuit. Thus, measurements at short circuit, where the internal field is high and the charge carriers are efficiently swept out, are not ideal for the study of recombination [120].

b) Intensity dependence of Voc

The light intensity dependence of Voc provides independent and complementary information on the details of the recombination processes from that obtained from Jsc.

Under open-circuit conditions, the current is zero; all photogenerated carriers recombine within the cell. Thus, recombination studies near open circuit are particularly sensitive to the details of the recombination mechanism.

The study of light intensity dependence of open circuit voltage helps to distinguish between trap assisted recombination (monomolecular) or Langevin type recombination (bimolecular recombination) [120]. The value of the slope of Voc versus natural logarithm of the light intensity depends on the strength of the recombination with a slope of β [121] i.e.

$$V_{OC} \propto \ln I, with\ slope\ \beta \tag{1.41}$$

If the slope β = kT/q, the transport is trap free and a Langevin type recombination is a dominant lose mechanism (where k is Boltzmans constant, T absolute temperature, q elementary charge, and I intensity).

If β > kT/q, a trap assisted recombination (monomolecular) is dominated over bimolecular recombination

1.5 Objectives of the study

The general objective of this study is to study charge carrier transport properties of intrinsic conjugated polymers, develop and characterize bulk heterojunction organic solar cells and to get insight on the performance of the polymers.

The specific objectives are:

1. To study the hole transport property of pristine conjugated polymers by using different techniques in order to get insight in their optoelectronic performance.
2. To study the electric field and temperature effects on mobility in order to predict the charge transport mechanism in the polymer.
3. To compare the admittance spectroscopy with other techniques for measurement of charge transport property of polymers in order to establish for future use.
4. To characterize the optical, electrical and transport property of a newly synthesized conjugated polymers in order to predict its performance in organic solar cells.
5. To develop a Bulk Hetrojunction photovoltaics and characterize their performance of organic polymers.
6. To study light intensity effect on the performance of organic photovoltaic in order to get insight about the lose mechanism of the device.

2 Experimental

2.1 General

All required chemicals were bought from Sigma-Aldrich and most of them were used as received except poly(3,4-ethylenedioxythiophene)/polystyrene sulfonic acid (CLEVIOS P VP AI 4083, H.C. Starck), $(C_4H_9)_4NClO_4$ (Fluka, crystallized from CH_3OH and Vacuum dried), and CH_3CN(Merck, stored under argon pressure and over molecular sieves 3 Å activated at 400 °C for four hours).

In all cases a patterned Indium doped Tin Oxide (ITO) glass was used as supporting substrate. The ITO was first cleaned by sonication for 15 minutes with acetone then with another 15 minutes in isopropanole, consecutively. Finally it was treated in Ozone-UV chamber for another 15 minutes.

The I-V characterizations were made with Keilthy 2400 source- meter. AMEL5000 electrochemical work station was used for electrochemical characterizations. UV-Vis absorption spectrum was recorded with a Perkin Elmer 950 spectrometer and Photo luminescence spectrum with Spec Fluorolog II 1681 spectrofluorometer. Solartron 1255 Frequency Response Analyzer with a Solartron 1294 dielectric interface was used for admittance measurements. SRS (Stanford Research Systems inc.) DS 345 function generator was used as a source of function in the measurement of CELIVE experiments. HP 214A was used as a source of rectangular function in DISCL transient characterization. Tencor AlphaStep profilo meter was used for thickness measurements. Pt100 thermoresistor was used to measure the temperature of the devices.

Solar cells were illuminated by using a solar simulator (SUN 2000, Abet Technologies) and the light power intensity was calibrated using a certified silicon solar

cell. For light-intensity dependent measurements, a set of quartz neutral filters were used to vary the incident light power intensity.

2.2 Hole mobility measurement of APFO-Green 6

2.2.1 Hole mobility measurement of APFO-Green 6 with AS

The devices used in this study were prepared in the sandwiched structure ITO/PEDOT:PSS/APFO-Green 6/Al, Figure 2.1, where ITO is indium tin oxide and PEDOT:PSS is poly(3,4-ethylenedioxythiophene)/polystyrene sulphonic acid (work function 5.0 - 5.2 eV). The polymer HOMO/LUMO levels are at – 5.2 eV and at – 3.5 eV respectively.

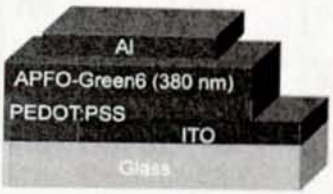

Figure 2.1 Device structure of ITO/PEDOT:PSS/APFO-Green 6/Al.

The polymer layer was spin-coated with 800 rpm from a chloroform solution (20 g/L). The thickness of the polymer film was 380 nm. Before the deposition of the Al cathode on the top of the film, the polymer film was annealed at 135°C for 25 min to completely remove the solvent. The top Al electrode (70 nm) was thermally evaporated at a base pressure of 4×10^{-6} mbar through a shadow mask giving an active device area 0.24 cm^2 in Argon atmosphere glovebox.

The complex admittance was measured at room temperature and under dynamic vacuum (10^{-5} mbar). The amplitude of the ac modulation voltage was 80 mV, V_{dc} was

varied in the range 0 – 10 V with a voltage step of 1 V, and a frequency sweep range of 1–5 x 10^5 Hz was used.

2.2.2 Hole mobility measurement of APFO-Green 6 with CELIV

The device structure was the same as that of AS, ITO/PEDOT:PSS/APFO-Green 6/Al. With this structure two devices were prepared with experimental conditions indicated in Table 2.1.

Table 2.1 Devices tested with CELIV technique

Device code	Solvent used	Conc. (g/L)	Spin coating speed (rpm)	Thickness (nm)	Active area (cm^2)	Annealing
A	$CHCl_3$	40	700	420	0.081	No annealing
B	$CHCl_3$	20	800	380	0.24	135°C (25min)

The annealing was made in argon filled glove box. The CELIV measurement was done under dynamic vacuum in homemade chamber at room temperature.

2.3 Hole mobility measurement of APFO-Green 5

2.3.1 Hole mobility measurement of APFO-Green 5 with AS

The devices used in this study were prepared in the sandwiched structure ITO/PEDOT:PSS/APFO-Green5/Al, Figure 2.2. The polymer layer was spin-coated at 760 rpm from a chloroform solution (10 g/L). The thickness of the polymer layer was 260 nm.

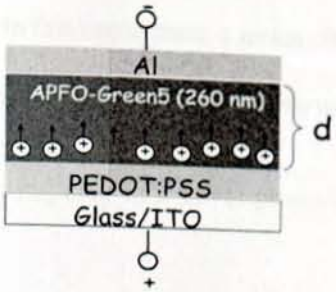

Figure 2.2 Device structure ITO/PEDOT:PSS/APFO-Green5/Al.

Before the deposition of the top electrode the polymer films were annealed at 135 °C for 25 min. The top Al electrode (70 nm) was thermally evaporated at a base pressure of $4x10^{-6}$ mbar through a shadow mask giving an active device area of 0.26 cm^2.

The electrical characterization of the devices was carried out in homemade chamber under dynamic vacuum (0.5 mbar). The amplitude of the ac modulation voltage in Admittance measurement was 50 mV, the forward dc bias was varied in the range 0 – 10 V with a voltage step of 1 V, and a frequency sweep range of 1 – 5 x 10^5 Hz was used.

2.3.2 Hole mobility measurement of APFO-Green 5 with DISCL transient

The devices used in this study were prepared in the sandwiched structure ITO/PEDOT: PSS/APFO-Green 5/Al. The polymer layer was coated on the substrate with doctor - blading technique from a chlorobenzene solution (16 g/L) and dried for 24 hours. The thickness of the polymer layer was 2.33 μm. The top Al electrode (70 nm) was thermally evaporated at a base pressure of $4x10^{-6}$ mbar through a shadow mask giving an active device area of 0.24 cm^2.

The electrical characterization of the devices was carried out under dynamic vacuum (0.5 mbar). In this experiment, a rectangular voltage pulse (amplitude 5 – 40 V, pulse duration 10 ms) was applied to the sample using pulse generator.

2.4 Transport property of a novel phenyl substituted polythiophene (PPOPT)

UV–Vis absorption and Photoluminescence (PL) spectrum were recorded in solution and in thin film on quartz substrate. Quantum yields of PL for solutions were obtained as relative values using $Ru(bipy)_3Cl_2$ in aerated water solution as the reference, and an Edinburgh fluorometer equipped with a Labsphere integrating sphere was used to measure absolute PL quantum yields of solid films [122].

Cyclic voltammetries of PPOPT thin films, spin-coated onto ITO-coated glass substrate (15 mm x 15 mm) from a chloroform solution, were recorded. A three electrode system was used, consisting of a platinum wire as auxiliary electrode, aqueous Saturated Calomel (SCE), whose potential resulted –0.392 V vs. ferrocene/ferricenium internal reference [123] and ITO as working electrode. The three electrodes were placed in an electrochemical cell consisting of three compartments separated by glass frits. A 0.1 $molL^{-1}$ tetrabutylammonium perchlorate $(C_4H_9)_4NClO_4$ in acetonitrile (CH_3CN) was used as supporting electrolyte. Argon gas was bubbled for 20 minutes in the working compartment before the measurement. During the measurement, argon gas was flushed into the working electrode compartment.

Admittance spectroscopy technique was used to characterize the transport property of the polymer. The devices used for admittance spectroscopy measurements were prepared in the sandwiched structure ITO/PEDOT: PSS/PPOPT/Al. The layer of PEDOT: PSS (around 40 nm) was spin-coated at 4000 rpm onto ITO/glass substrates, and then baked in an oven at 120°C for 10 min. The polymer layer was spin-coated at

850 rpm from a chloroform solution (22 g L^{-1}) and thermally annealed at 120°C for 25 min in argon atmosphere before the top electrode deposition. The thickness of the polymer layer was 260 nm. The top Al electrode (70 nm) was thermally evaporated at a base pressure of 4 x 10^{-6} mbar through a shadow mask giving an active device area of 0.25 cm^2.

The electrical characterization of the devices was carried out at room temperature under dynamic vacuum (5 x 10^{-5} mbar). Admittance was measured with amplitude of the ac modulation voltage 50 mV, the forward dc bias varied in the range 0 – 10 V with a voltage step of 1 V, and a frequency sweep range of 1 – 5 x 10^5 Hz was used.

2.5 Bulk –hetero junction solar cell of random Co-polymer (PF-Co-FT)

UV–vis absorption spectra of films spin-coated onto quartz substrates were recorded. From electrochemical characterization of the polymer the HOMO and LUMO levels are reported [124] to be –5.61 eV and –2.87 eV, respectively.

Solar cells were fabricated on patterned ITO-coated glass. A PEDOT:PSS layer was spin-coated at 4000 rpm resulting a thickness of around 40 nm, then baked in an oven at 140°C for 10 min. PFB-co-FT and PCBM were dissolved in a given solvent (chloroform, chlorobenzene(CB), diChlorobenzene (DCB) or in mixed 1,2-dichlorobenzene/chloroform solvent in 1:1 v/v). The solutions (25 g L^{-1}) were stirred at 40°C for three days. The blend solutions were spin-coated in air onto the ITO/PEDOT:PSS substrates. Then the samples were transferred to an Argon glove-box, where the device structure was completed with the thermal evaporation of the top electrode (Al or LiF/Al) at a base pressure of 3 x 10^{-6} mbar. The active area of the device was defined by the shadow mask used for the cathode deposition. The solar cell characterization was carried out at room temperature in an Argon glove-box.

2.6 BisEH-PFDTBT: PCBM solar cells: a compositional, thickness, and light intensity dependence study

The synthesis of the polymer reported elsewhere [125]. UV–vis absorption and photoluminescence spectra of films spin-coated onto quartz substrates were recorded for the study of blend weight ratio effect.

Solar cells were fabricated on patterned ITO-coated glass substrates on which a PEDOT:PSS layer was spin-coated at 4000 rpm that result a thickness of around 40 nm, then baked in an oven at 140°C for 10 min. BisEH-PFDTBT and PCBM were dissolved in mixed 1,2-dichlorobenzene/chloroform solvent in 1:1(v/v). The solutions (25 g L^{-1}) were stirred at 40 °C for four days. The blend solutions were spin-coated in air onto the ITO/PEDOT:PSS substrates. Then the samples were transferred to an Argon glove-box, where the device structure was completed with the thermal evaporation of the top electrode (Al or LiF/Al) at a base pressure of 3 x 10^{-6} mbar. The active device area, defined by the shadow mask used for the cathode deposition, was 8 mm^2.

The device electrical characterization was carried out at room temperature in an Argon glove-box. Solar cells were characterized by using solar simulator and the light intensity dependence was studied by using a set of quartz neutral filters.

3. Result and Discussion

3.1 Hole mobility measurement of APFO-Green 6

APFO-Green6 [126] is a family of group of polymers called alternating polyfluorene copolymers. It is a low band gap polymer which absorbs 400 nm to 800 nm, Figure 3.1.

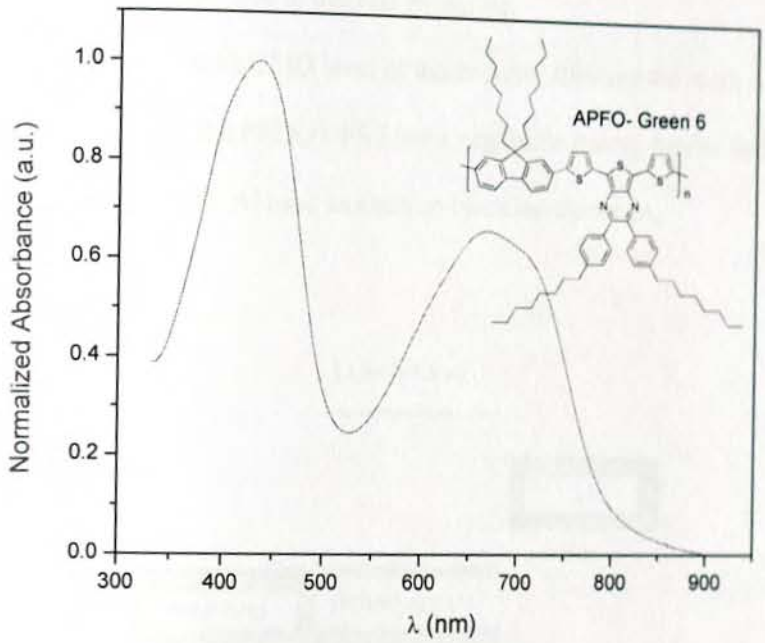

Figure 3.1 Absorption spectra of APFO-Green 6 and its molecular formula.

The polymer HOMO/LUMO levels, estimated by the onset of its oxidation/reduction potentials, are at – 5.2 eV and at – 3.5 eV, respectively [127].

The APFO-Green 6 has been tested for bulk-heterojunction (BHJ) solar cells in which it was used as the absorber and electron-donor material [126]. The polymer was blended with PCBM fullerene derivative, acting as the electron-acceptor, and the related solar cells exhibited a power conversion efficiency of 1.4%.

Gaining insight into the mechanism of charge transport of active materials of solar cells is necessary for optimizing device performance. Therefore, its mobility has been studied with AS and CELIV techniques.

3.1.1 Hole mobility measurement with Admittance Spectroscopy [128]

The absorption spectrum of the polymer film before and after thermal annealing were recorded resulting a similar pattern that may indicate the annealing does not degrade the polymer film due to thermal annealing.

Based on the HOMO/LUMO level of the polymer film and the work function of the electrodes, Figure 3.2, the PEDOT:PSS has a negligible energy barrier and used as hole injecting electrode while Al used as electron blocking electrode.

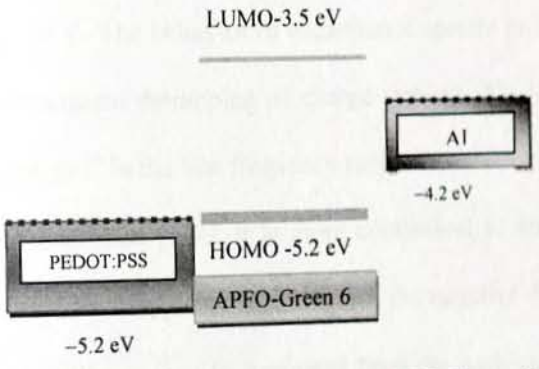

Figure 3.2 Energy levels of ITO/PEDOT:PSS/APFO-Green 6/Al

The built in potential (V_{bi}) was approximated to be nearly 1 V by taking the difference of the work function of PEDOT:PSS and Al electrodes.

Figure 3.3 shows the conductance and capacitance as a function of the modulation frequency measured on an ITO/PEDOT:PSS/APFO-Green6/Al hole-only device structure for different forward dc-bias voltages i.e. V_{dc} 0 – 10 V. Here ITO was positively biased.

At zero bias the low-frequency conductance is low and the capacitance is nearly frequency independent, Figure 3.3a. If a relative dielectric constant of around 3 is assumed for APFO-Green6, the value observed for the capacitance at zero bias (~ 1.7 nF) is consistent with that expected for the geometrical capacitance, C_{geo}, of the polymer film. The same behavior for capacitance and only a slight increase of the low-frequency conductance was observed for V_{dc} = 1 V, indicating no injection of carriers.

As the bias was increased well above the built-in voltage, the behavior changed drastically due to the beginning of hole injection. Towards high frequencies the capacitance again tend to C_{geo}, while a slow decrease of C, with respect to C_{geo}, is observed at intermediate frequencies (10^3 - 10^4 Hz), due to charge injection, Figure 3.3b and 3.4a. In the same intermediate frequency range, the conductance shows a small dip, Figure 3.3a, other than increasing by orders of magnitudes by increasing the applied bias up to 10 V. The behavior of capacitance spectra at low frequencies is due to trapping and subsequent detrapping of charge carriers [52, 129, 130], leading to a positive contribution to C in the low frequency range.

As already demonstrated [131], it is more convenient to infer the average transit times of carriers from the frequency, f_{max}, at which the negative differential susceptance shows its maximum value. τ_{tr} can be evaluated from the position of the maximum in $-\Delta B$ plot through f_{max}. Peaks in $-\Delta B$ plots versus frequencies were clearly observed for V_{dc} of at least 4 V, Figure 3.4b. The peaks increase and shift towards higher frequencies as V_{dc} increases. The hole mobility values were calculated by using Equation 1.21.

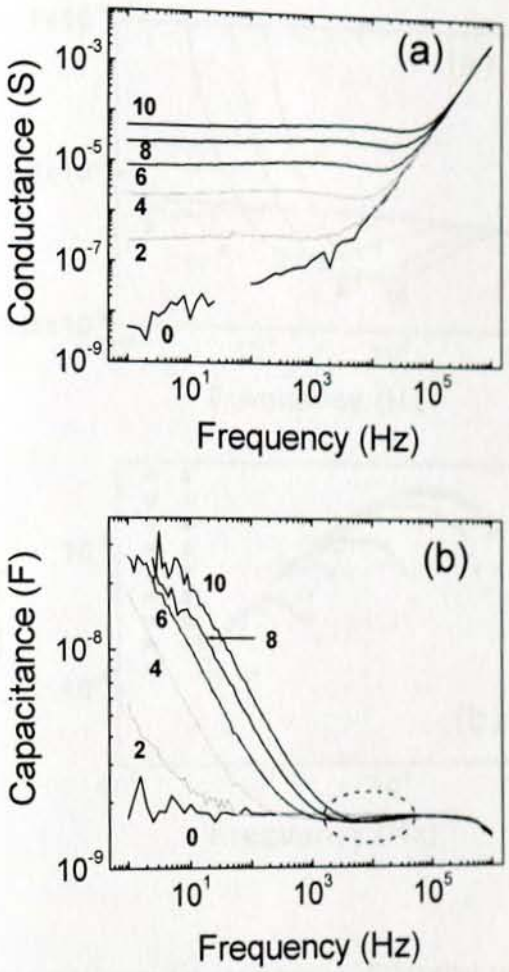

Figure 3.3 Frequency dependence of conductance (a) and capacitance (b) for an ITO/PEDOT:PSS/APFO-Green6/Al device at different dc bias voltages (values in V_{bias} indicated in the figure). In the bottom figure the broken line indicate the intermediate frequency range at which capacitance is lower than the geometrical capacitance.

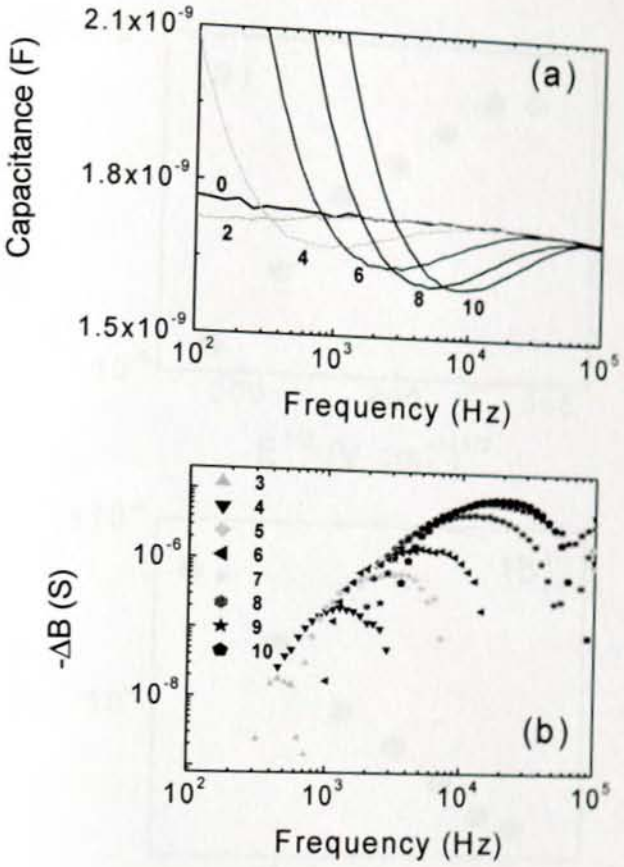

Figure 3.4 Variation of capacitance (a) and negative differential susceptance (b) with frequency in the intermediate frequency range, at different dc bias voltages (values in V indicated in the figure).

The hole mobility (μ_h) calculated from the maximum frequencies are shown in the semi-logarithmic plot of Figure 3.5a as a function of the square root of the electric field *E*.

The rough linear trend indicates that the experimental data follow the Poole-Frenkel expression.

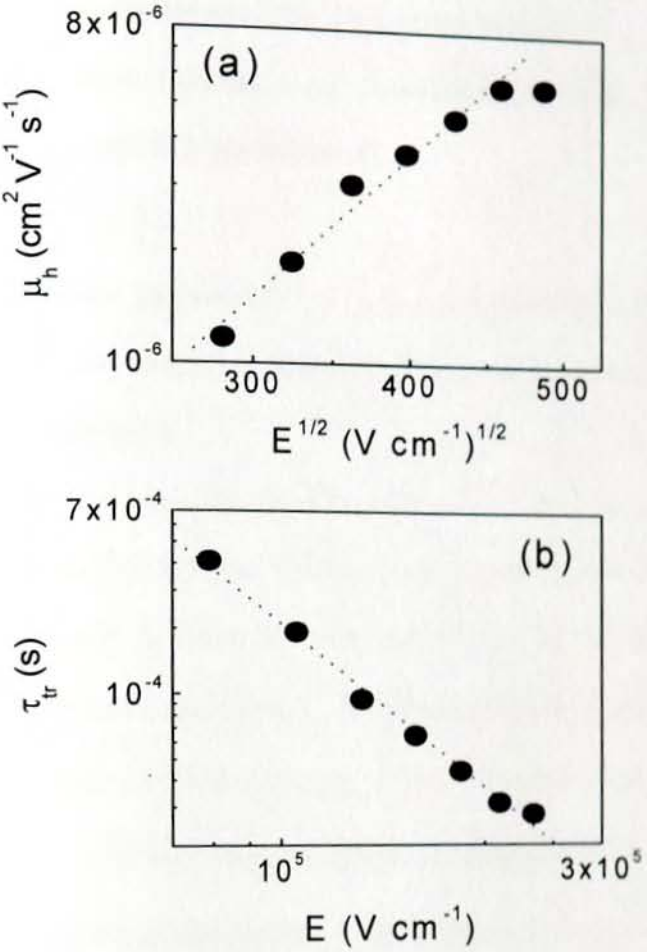

Figure 3.5 Electric field dependence of (a) hole mobilities and (b) hole transit times for an ITO/PEDOT:PSS/APFO-Green6/Al device. The dotted line represents the linear fit to the experimental data.

The parameters for the Poole-Frenkel fit to mobility data of Fig. 3.5a are $\mu_0 = 1.45\text{x}10^{-7}$ cm^2 V^{-1} s^{-1} and $\gamma = 8.0\text{x}10^{-3}$ (V/cm)$^{-1/2}$.

The square root field dependence of mobility, frequently observed in disordered molecular materials [132], is expected in the case of trapping effects. The

immobilization of carriers for time periods by trapping sites distributed in energy leads to a broad distribution of transit times, hat is to a dispersive transport.

It has been shown [133] that, in a multiple trapping model, the transit time of carriers exhibit the electric field dependence of

$$\tau_{tr}(E) \propto E^{-1/\alpha} \tag{3.1}$$

where α is a dispersion parameter ($0 < \alpha < 1$; $\alpha = 1$ for non dispersive transport) introduced by Scher and Montroll [134] in their model for the description of dispersive transport in amorphous solids.

The electric field dependence of hole transit times derived from admittance measurements are reported in Figure 3.5b in a double logarithmic plot. From the slope of the line representing the linear fit to the experimental data a value of 0.4 was obtained for the dispersion parameter α, comparable to other polymers [55]. In the case of an exponential distribution of trapping sites α is related to its characteristic temperature T_0 by $\alpha = T/T_0$, T being the absolute temperature. The obtained value of α gives a characteristic temperature for the energy distribution of traps of 754 K.

3.1.2 Hole mobility measurement of APFO-Green 6 with CELIV

Figure 3.6 shows a typical CELIV measurement of this polymer. Unfortunately the devices did not give the characteristic signals of CELIV and it was not possible to determine the mobility the polymer with this technique, which could be due to high degree of dispersive carrier mobility in this polymer. However, from the capacitive peaks, the relative permittivity of the polymer was calculated by using Equation 1.8 and the average value was found to be 3.2, which is very common value for most organic polymers.

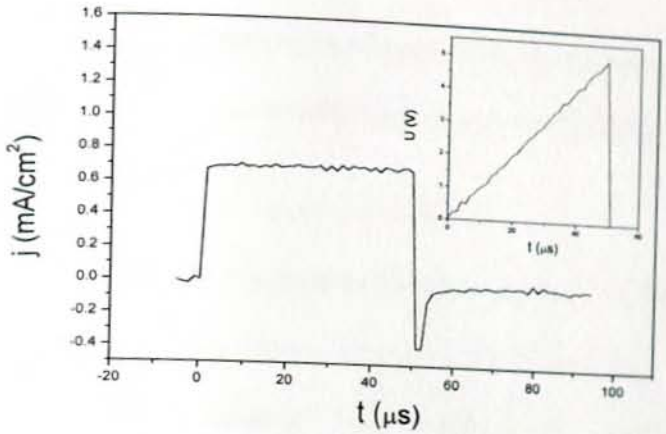

Figure 3.6 CELIV measurement of ITO/PDOT:PSS/APFO-Green/Al, Device B. Thickness of PEDOT:PSS 40 nm, Polymer 380 nm, Al 100 nm. Inset is the ramp with A of 102 kV/s.

3.1.3 Conclusion

The mobility of holes in a film of the alternating polyfluorene APFO-Green6 was investigated by admittance spectroscopy. Mobilities of the order of 10^{-6} cm^2 V^{-1} s^{-1} were calculated at room temperature from the peak positions of the negative differential susceptance in the electric filed range $5x10^4 - 2x10^5$ V cm^{-1}. Hole mobility was found to be strongly field-dependent and, as evidenced by the behaviour of the low-frequency capacitance spectra, carrier transport is affected by trapping effects. A dispersion parameter of 0.4 was achieved from the trend of holes transit times with the electric field.

The measurement of hole mobility of APFO-Green 6 was tried using dark CELIV. But the characteristic CELIV signal was not observed, which could be low charge carrier concentration and high dispersive transport. Hence, photo-CELIV could

be appropriate, which generate more charge carriers. However, the relative permittivity of the polymer was determined to be 3.2.

Therefore, Admittance Spectroscopy could be suitable to determine the charge carrier mobility of this class of compound compared to dark CELIV.

3.2 Hole transport property of APFO-Green 5

The low-bandgap conjugated polymer called APFO-Green 5 belongs to a large family of alternating poly fluorene copolymers (APFOs) [135]. APFO-Green 5 is an alternating copolymer based on fluorine and donor- acceptor-donor segments of thiophene and electron accepting groups. APFO-Green 5, due to the alternating electron-rich and electron-poor units in its molecular structure, Figure 3.7, exhibits a bandgap of 1.6 eV, which makes it suitable for absorbing long-wavelength photons. The synthesis and properties of the polymer is reported elsewhere [136].

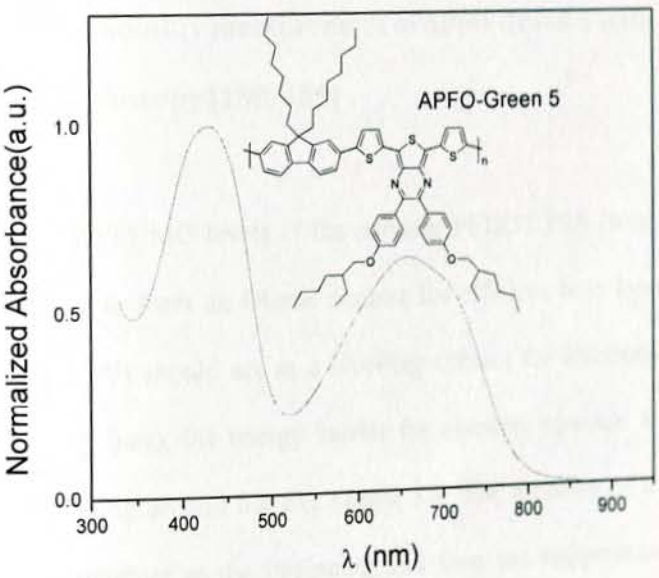

Figure 3.7 Molecular structure and absorption of APFO-Green5.

The polymer HOMO/LUMO levels [136], as determined by cyclic voltammetry, are at – 5.0 eV and at – 3.4 eV, respectively.

APFO-Green5 has already been proposed as electron-donor component in polymer/fullerene bulk heterojunction solar cells, showing a photoresponse extended up to 800 nm and an overall power conversion efficiency of 2.2% [136].

The hole mobility of APFO-Green 5 has already been investigated by FET and CELIV techniques [137]. The two different methods gave hole mobilities differing by one order of magnitude, those extracted from CELIV (around 2×10^{-5} $cm^2 V^{-1}s^{-1}$ for an applied field 10^5 V cm^{-1}) being lower than FET.

In this study, the hole mobility of APFO-Green 5 is investigated by AS and DISCL transient methods and compared to the values previously reported with FET and CELIV methods. In order to get more insight of its performance of the polymer, the effect of temperature on its hole mobility has also been investigated.

3.2.1 Hole mobility measurement of APFO-Green 5 with Admittance Spectroscopy [138, 139]

Based on HOMO/LUMO levels of the polymer PEDOT:PSS (work function 5.0 – 5.2 eV) is expected to form an Ohmic contact for efficient hole injection, while Al (work function 4.2 eV) should act as a blocking contact for electrons under forward bias (ITO positively bias), the energy barrier for electron injection al the Al/APFO-Green 5 interface being around 0.8 eV, Figure 3.8. The mobility of the polymer was done at room temperature at the beginning and then the temperature effect on the mobility was studied in the temperature range of 4-64 °C.

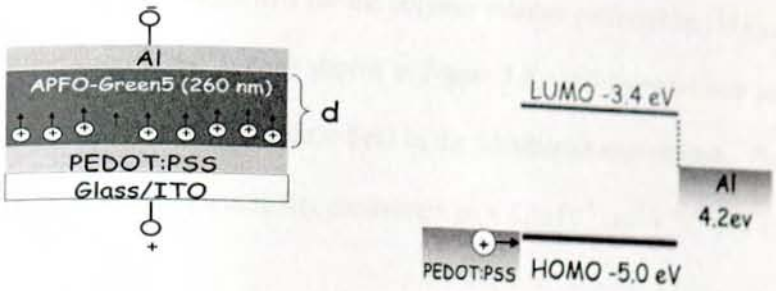

Figure 3.8 Device structure and Energy level diagram of ITO/PEDOT:PSS/APFO-Green5/Al.

The exact calculation of the electric field (E) applied to the ITO/PEDOT:PSS/APFO-Green5/Al structure requires the evaluation of the device built-in potential (V_{bi}).

Since a polymer can be assumed to be completely depleted of charges at low voltages, the electric field inside the polymer is spatially uniform and the energy bands remain rigid. In this case the built-in potential is expected to be given by the difference in the work functions of the electrodes. However, due to the creation of interface dipoles, chemical reactions between polymer and electrode, or charge accumulation near the electrodes, the built-in potential could significantly deviate from the difference of the two electrode work functions [139,140]. From the values of the electronic work functions of PEDOT:PSS (around 5.0 eV) and Al the V_{bi} is expected lower than 1 V. The value of V_{bi} was evaluated from the current-voltage (I-V) curve of the device, for forward bias V_{bias} in the same range used for the admittance experiments (up to 10 V) and found to be 0.7 V.

The J-V characteristic of the ITO/PEDOT:PSS/APFO-Green 5/Al device was fitted by using the formula of Murgatroyd [61] in the space-charge limited current regime, Equation 1.23, where the electric field is given by $(V_{bias} - V_{bi})/d$.

By assuming a value of 3 for the polymer relative permittivity [141], a good fit was obtained for V_{bi} = 0.7 V, as shown in Figure 3.9, and its value was used for the determination of the applied electric field in the admittance experiments. The fit of the j-V data also provided the mobility parameters $\mu_0 = 6.5 \times 10^{-8}$ cm^2 V^{-1}s^{-1} and $\gamma = 8.3 \times 10^{-3}$ (V cm^{-1})$^{-1/2}$.

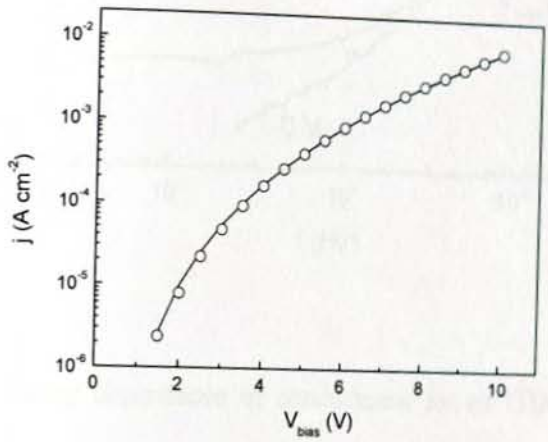

Figure 3.9 Current density as a function of forward bias for an ITO/PEDOT:PSS/APFO-Green 5/Al device. The line is a fit to the experimental data by using the formula of Murgatroyd. The thickness of the polymer layer was 260 nm.

3.2.1.1 Room Temperature Hole mobility

The admittance experiments were performed by using a V_{bias} up to 10 V, with a voltage step of 1 V. The conductance, very low for V_{bias} = 0 V, increased by orders of magnitude by increasing the dc bias, Figure 3.10. A small dip in the conductance spectra was observed in the intermediate frequency range (10^4-10^5 Hz), shifting to higher frequencies for higher values of V_{bias}. These features are an indication of the occurrence of charge injection.

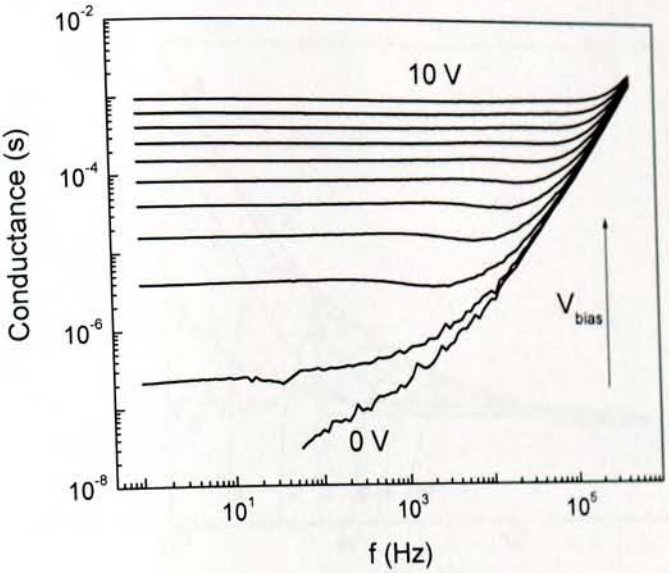

Figure 3.10 Frequency dependence of conductance for an ITO/PEDOT:PSS/APFO-Green 5/Al device, for dc bias (V_{bias}) values in the range 0 – 10 V and with a step of 1 V. The arrow indicates the direction of increasing V_{bias}.

The capacitance was found to be almost frequency-independent when the dc bias was not applied (V_{bias} = 0 V), as expected in the case of no injection of charge carriers, and its value (around 2.7 nF) is consistent with the geometrical capacitance of a sample with an area of 0.26 cm^2, a thickness of 260 nm, and a relative permittivity of 3. The capacitance spectra greatly changed upon applying the bias, mainly at low frequencies, as shown in Figure 3.11. For V_{bias} up to 3 V, C increased with increasing V_{bias} and decreasing f up to its minimum value (1 Hz). The capacitance excess at low frequencies provides evidence for charge relaxation in trap levels [52,129,130], other than indicating charge injection.

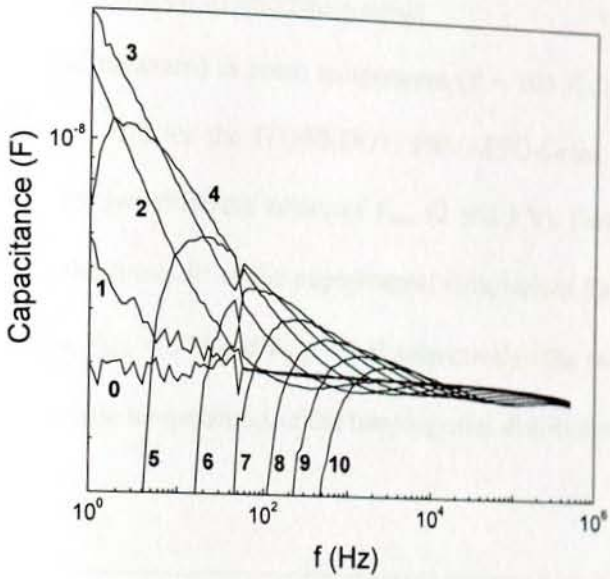

Figure 3.11 Frequency dependence of capacitance for an ITO/PEDOT:PSS/APFO-Green 5/Al device at different dc bias values (values in V are shown in the figure) in the all range of the modulation frequency in log – log scale.

It has been shown that in the case of an exponential distribution of trapping sites, very common in disordered organic semiconductors [134, 142], the characteristic temperature of the distribution, T_0, can be derived from the slope of the double-logarithmic plot of C vs f, Equation 3.2. Indeed, for $T < T_0$, T being the absolute temperature, the capacitance is expected to follow a power-law expression, in the low-frequency region

$$C(f) \propto f^{-\alpha} \tag{3.2}$$

where $\alpha = T/T_0$ is a dispersion parameter ($0 < \alpha < 1$; $\alpha = 1$ for non dispersive transport)

This formalism is introduced by Scher and Montroll [134] in their model for the description of dispersive transport in amorphous solids.

The capacitance measured at room temperature (T = 300 K) and in the low-frequency range (f > 40 Hz) for the ITO/PEDOT: PSS/APFO-Green 5/Al device is shown in Figure 3.12 for two different values of V_{bias} (2 and 3 V). From the slopes of the lines representing the linear fit to the experimental data, values for α of 0.40 and 0.41 were obtained, for V_{bias} = 3 V and V_{bias} = 2 V respectively. The two values for α correspond to characteristic temperatures of the trapping-sites distribution of 750 K and 732 K, respectively.

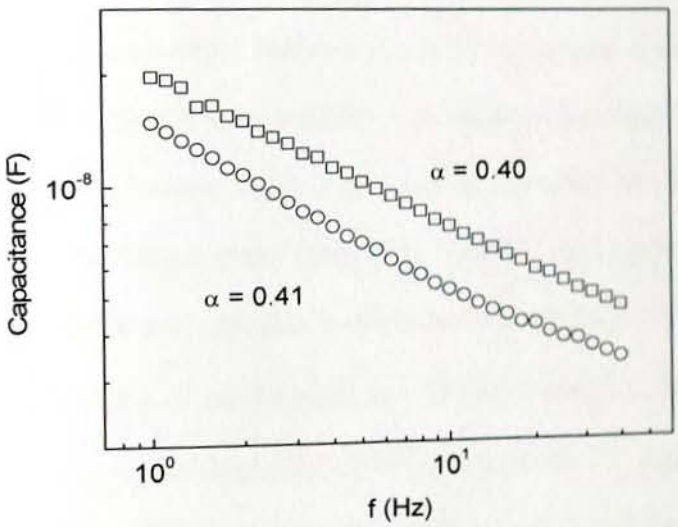

Figure 3.12 Low-frequency range dependence of capacitance for an ITO/PEDOT:PSS/APFO-Green 5/Al device at V_{bias} of 2 V (circles) and of 3 V (squares). The dotted lines represent the linear fits to the experimental data. The values of the dispersion parameter α are shown in the figure.

When V_{bias} was further increased (V_{bias} > 3 V), a more complex behavior of capacitance was observed at low frequencies ($f < 10^3$ Hz). Towards low f, capacitance first increased, reached a maximum, and then rapidly decreased attaining negative values. The frequency range in which C showed this behavior was strongly dependent on the dc bias, shifting towards higher frequencies as V_{bias} increased, Figure 3.11. The frequency at which negative values of C were attained changed from 3 Hz for V_{bias} = 5 V to 280 Hz for V_{bias} = 10 V. These features of the capacitance spectra indicate double-injection of carriers [142] that is the aluminum contact allows for a weak unintentional injection of negative carriers.

For V_{bias} > 1 V, a minimum in the capacitance spectra was observed in the intermediate-high frequency range, Figures 3.11 and 3.13a, expected in conditions of high injection. The position of that minimum, determined by the transit time of the injected carriers, shifted towards higher frequencies by increasing the dc bias. It is convenient to infer the average transit times of carriers from the frequency, f_{max}, at which the negative differential susceptance shows its maximum value [53]. τ_{tr} can be evaluated from the position of the maximum in $-\Delta B$ plot through f_{max}. Peaks in $-\Delta B$ plots versus frequencies were clearly observed for V_{bias} higher than 1 V, Figure 3.13b.

The peaks increased in magnitude and shifted towards higher frequencies as V_{bias} increased. It is worth noting that susceptance spectra do not show two relaxation peaks, expected for dual-carrier injection. This indicates the occurrence of one or more of the following conditions [143]: (i) charge-transport is hole-dominated in the ITO/PEDOT:PSS/APFO-Green 5/Al structure for the investigated range of V_{bias}, so a second peak related to the transit times of negative carriers is not visible; (ii) two peaks cannot be resolved in the susceptance spectra because the mobilities of positive and negative carriers do not meaningfully differ; (iii) the contribution of trapping effects to

capacitance curves obscures the susceptance peak corresponding to the slowest carriers. We believe that, in the investigated ITO/PEDOT:PSS/APFO-Green 5/Al devices, transport is dominated by positive carriers injected from the ITO/PEDOT:PSS electrode, so the peak observed in the susceptance spectra is related to the transit time effect of holes, as discussed hereinafter.

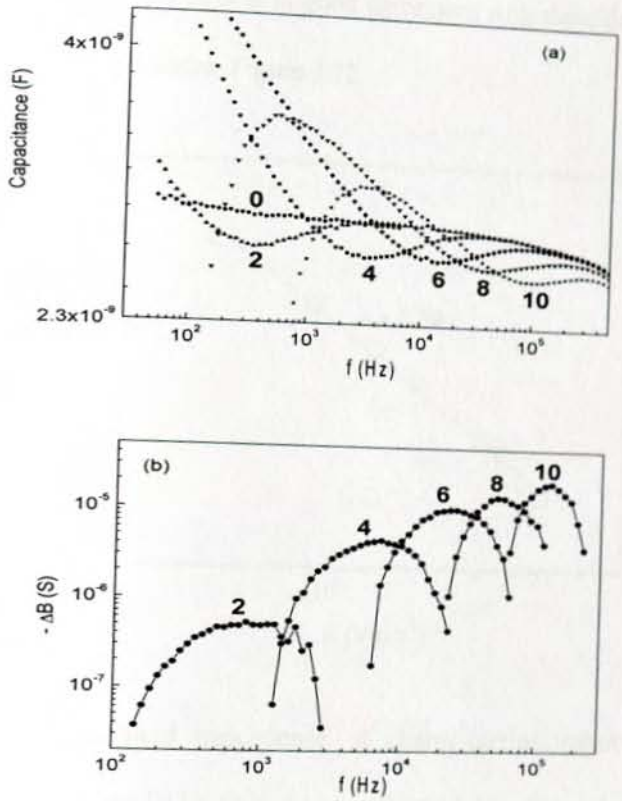

Figure 3.13 (a) Frequency dependence of capacitance for an ITO/PEDOT:PSS/APFO-Green 5/Al device at different dc bias values (values in V are shown in the figure) in the frequency range at which C is lower than the geometrical capacitance. (b) Variation of the negative differential susceptance with frequency at different dc bias voltages (values in V indicated in the figure). In the bottom figure, the lines are shown to guide the eye.

The transit times, derived from the maximum frequency of $-\Delta B$ plots are shown in Figure 3.14 as a function of the applied electric field with $V_{bi} = 0.7$ V.

From the linear fit to the experimental data of the double logarithmic plot shown in Figure 3.14, a value of 0.39 was obtained for the dispersion parameter α by using Equation 3.1, leading to a characteristic temperature for the energy distribution of traps of 769 K. The value of α is in good agreement with those derived from the low-frequency capacitance spectra, Figure 3.12.

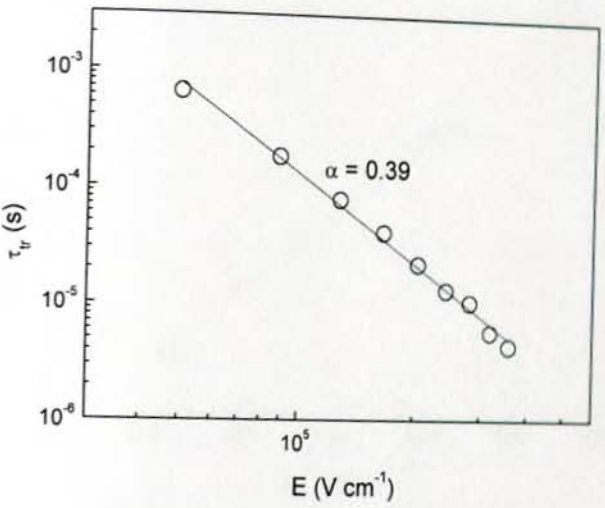

Figure 3.14 Electric field dependence of charge-carrier transit times. The line represents the linear fit to the experimental data. The value of the dispersion parameter α is shown in the figure.

Charge transport in most conjugated polymers, and in general in disordered systems, usually occurs as a series of hops between localized states, leading to a strong dependence of mobility on temperature and electric field [16] thus the investigation of mobility with temperature and field provides insight into the mechanisms of charge transport in these materials.

The calculated values of the charge-carrier mobilities are shown in the semi-logarithmic plot of Figure 3.15 as a function of the square root of the electric field. The good linear trend indicates that the experimental data follow the Poole-Frenkel expression, Equation 1.4, as expected from the I-V curve. The parameters for the Poole-Frenkel fit to mobility data of Figure 3.15 are $\mu_o = 1.44 \times 10^{-7}$ cm^2 V^{-1} s^{-1} and $\gamma = 8.0 \times 10^{-3}$ (V/cm)$^{-1/2}$, showing a good agreement, at least for γ, with those derived from the fit of the I-V data.

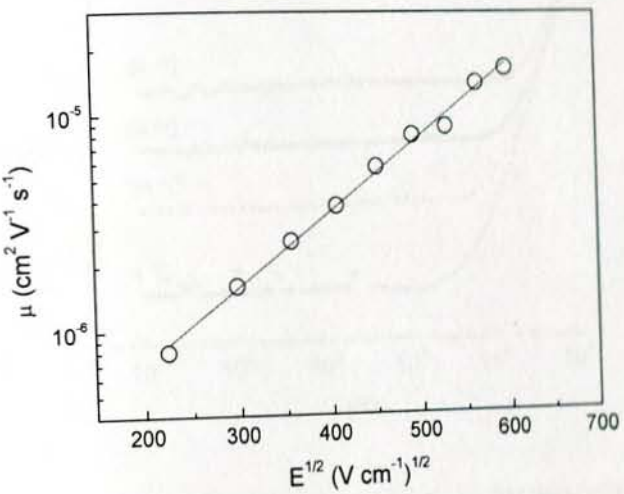

Figure 3.15 Square-root field dependence of charge-carrier mobility for an ITO/PEDOT:PSS/APFO-Green 5/Al device. The line represents the linear fit to the experimental data.

3.2.1.2 Effect of Temperature on Hole mobility

The dependence of the hole mobility of APFO-Green 5 was studied with temperature range of 4 – 64 °C. Figure 3.16 shows the conductance as a function of the modulation frequency for different values of temperature and at the forward bias of 6 V.

As expected, conductance was also greatly enhanced by increasing the temperature, changing by more than one order of magnitude in the temperature range 4 – 64 °C, indicating strongly thermally-activated charge carrier mobility. In the intermediate frequency range $10^4 - 10^5$ Hz, the conductance spectra show very small dips, Figure 3.16, moving toward higher frequencies for higher temperatures. Those dips are an indication of charge injection.

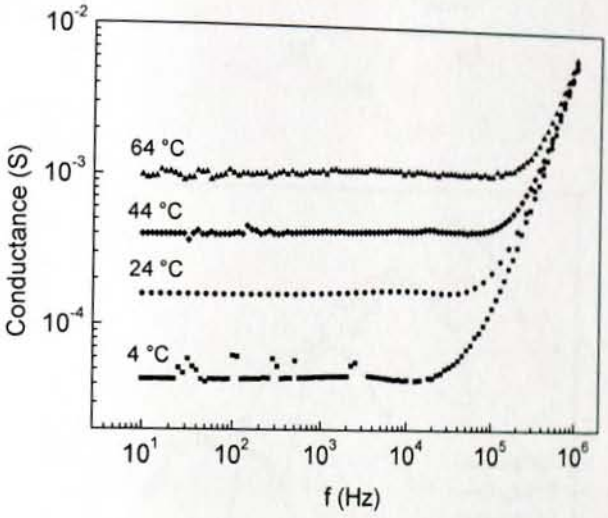

Figure 3.16 Frequency dependence of conductance for an ITO/PEDOT:PSS/APFO-Green 5/Al device at different temperatures and for a dc bias of 6 V.

In the capacitance spectra the typical minima were also observed in the same frequency range, Figure 3.17a. Hence, the negative differential susceptance, $-\Delta B$, is plotted based on these results, Figure 3.17b, for $V_{bias} = 6$ V and the average transit time of carriers were inferred from this plot. The peaks increased and shifted towards higher frequencies as temperature increases.

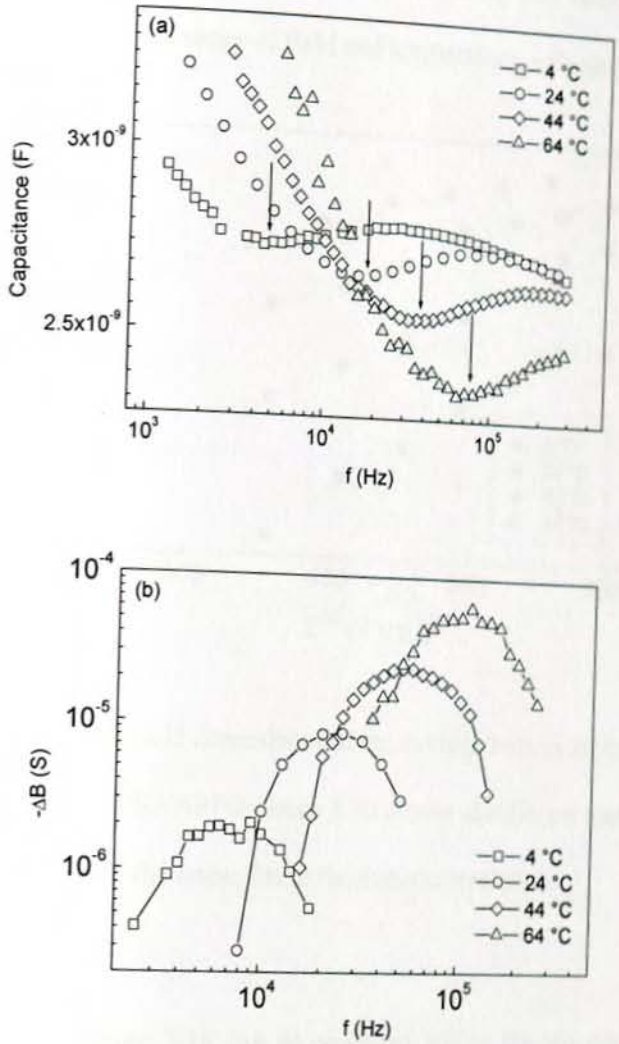

Figure 3.17 Intermediate-frequency spectra of capacitance (a) and negative differential susceptance (b) for an ITO/PEDOT:PSS/APFO-Green 5/Al device at different temperatures and for a dc bias of 6 V. In the bottom figure, the lines are shown to guide the eye.

The average hole mobility values obtained at the considered temperatures are reported in the semi-logarithmic plot of Figure 3.18 as a function of the square root of the electric field. A good linear trend of the experimental data was obtained, very

common for disordered organic materials and indicating that mobility in APFO-Green 5 obeys, in the investigated range of field and temperature, a Poole-Frenkel behavior.

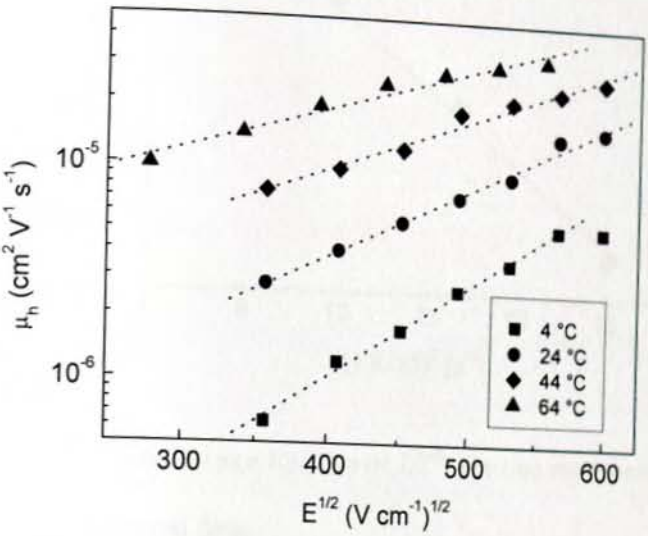

Figure 3.18 Square-root field dependence of the average hole mobility for an ITO/PEDOT:PSS/APFO-Green 5/Al device at different temperatures. The lines represent the linear fits to the experimental data.

The data of Figure 3.18 can be analyzed within the disorder formalisms for hopping transport in disordered organic solids. According to the well-known Gaussian Disorder Model (GDM) [144] for the hopping conduction of charge carriers among localized sites with a Gaussian profile of the density of states, mobility can be expressed with the semi-empirical equation, Equation 1.5.

The behavior with temperature of the zero-field mobility, obtained for each temperature from the fits of the experimental data of Figure 3.18 to Poole-Frenkel equation is reported in Figure 3.19.

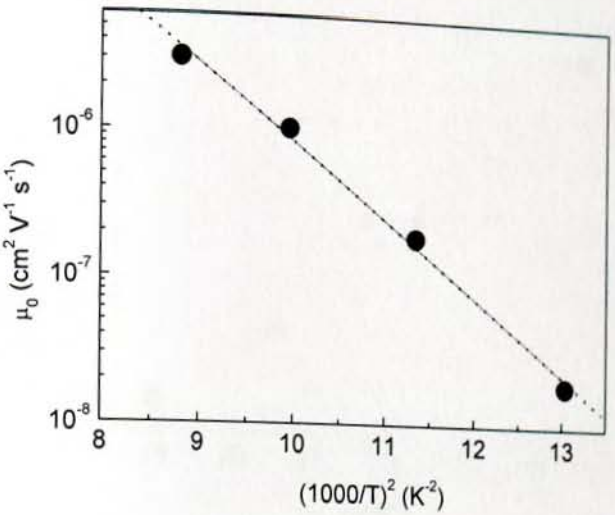

Figure 3.19 Zero-field mobility as a function of $1/T^2$. The line represents the linear fits to the experimental data.

Figure 3.19 shows an exponential decreasing trend with $1/T^2$, as predicted by the GDM model. The slope of the plot of μ_o versus $1/T^2$ yielded $\sigma = 0.14$ eV and its value was used to build the plot of Figure 3.20, in which the parameter γ is reported as a function of $(\sigma/kT)^2$. Again, γ was derived, for each temperature, from the fits of the mobility data shown in Figure 3.18 to Poole-Frenkel, Eqation 1.4.

According to GDM, Equation 1.5, the x intercept of the plot of Figure 3.19 gave $\Sigma = 3.86$. The values determined for the other parameters are $\mu_{inf} = 0.15$ cm^2 V^{-1} s^{-1} and $C_0 = 4.8\text{x}10^{-4}$ (V cm^{-1})$^{-1/2}$.

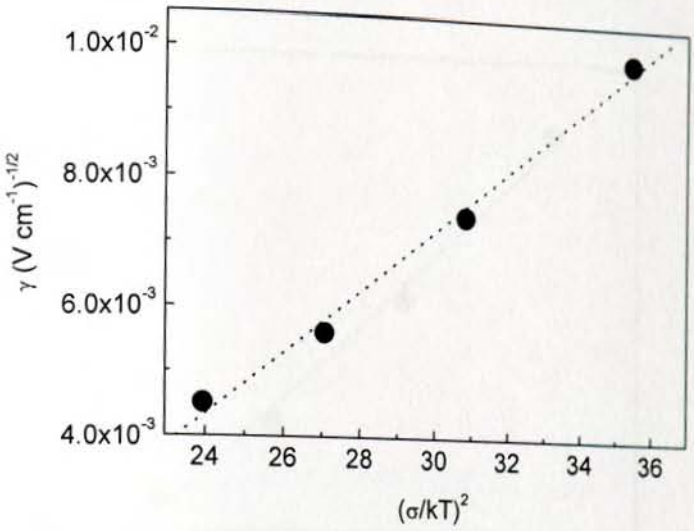

Figure 3.20 Poole-Frenkel γ parameter as a function of $(\sigma/kT)^2$ (GDM). The lines represent the linear fits to the experimental data.

Figure 3.19 results were also analyzed by the Correlated Gaussian Disorder Model (CDM). The main difference between GDM equation, Equation 1.5, and CDM equation, Equation 1.6, is the different temperature dependence of parameterγ, apart a slightly higher values for the energetic disorder σ, with respect to the GDM model. Hence, a 0.16 eV was calculated for σ from the fit of data of Figure 3.19 to Equation 1.6 (CDM).

The values of γ were plotted against $(\sigma/kT)^{3/2}$, Figure 3.21, and a very high value for the average site separation, a = 4.1 nm, was extracted from the linear fit according to Equation 1.6 (CDM).

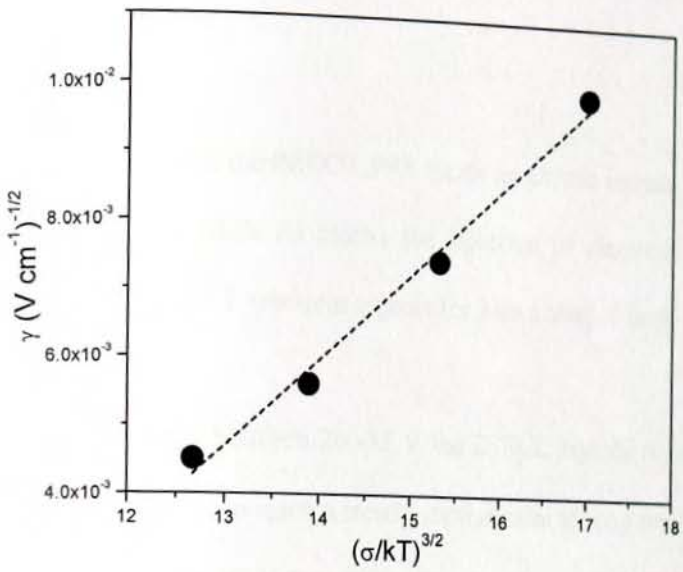

Figure 3.21 Poole-Frenkel γ parameter as a function of $(\sigma/kT)^{3/2}$ (CDM). The lines represent the linear fits to the experimental data.

The values of the charge transport parameters obtained by fitting the mobility data using the GDM and CDM models are summarized in Table 3.1. All the parameters are rather high, justifying the moderate transport properties of the investigated polymer films.

Table 3. 1. Values of the charge transport parameters obtained by fitting the mobility data using the GDM and CDM models.

Model	Parameter				
	μ_{inf} ($cm^2\ V^{-1}\ s^{-1}$)	σ (eV)	C_0 $(V\ cm^{-1})^{-1/2}$	Σ	a (nm)
GDM	0.15	0.14	4.8×10^{-4}	3.86	-
CDM	0.15	0.16	-	-	4.1

3.2.2 Hole mobility measurement of APFO-Green 5 with DISCL transient

As mentioned above the PEDOT:PSS forms an Ohmic contact with the polymer and used to inject holes while Al blocks the injection of electrons into the system. Figure 3.22 shows the DISCL transient signals for bias voltages from 10 – 40 V in step of 5 V.

For bias potentials between 20 -35 V the DISCL signals riches a peak at well defined time, τ_{tr}, and decays to reach a steady state current at long time. But below bias potential of 20 V and after 35 V it is difficult to see the characteristic DISCL signals may be due to poor injection in the lower bias potentials and short transit time at high potentials. In the regions where the characteristic DISCL signal were observed it is simple to extract the parameters that are necessary to calculate the hole mobility data.

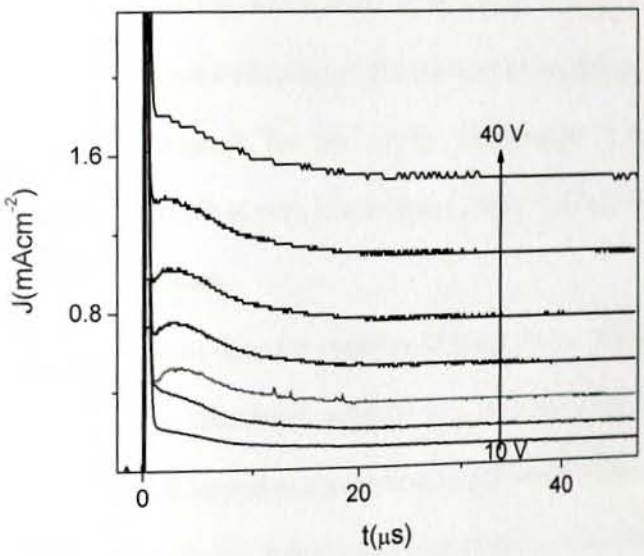

Figure 3.22 Room temperature DI transient s under applied bias from 10 – 40 V in step of 5V of APFO Green 5 with device structure of ITO/PEDOT: PSS/APFO-Green 5/Al. Active layer thickness was 2.33 μm.

The DISCL transient time extracted from Figure 3.22 as a function of applied electric field is shown in Figure 3.23.

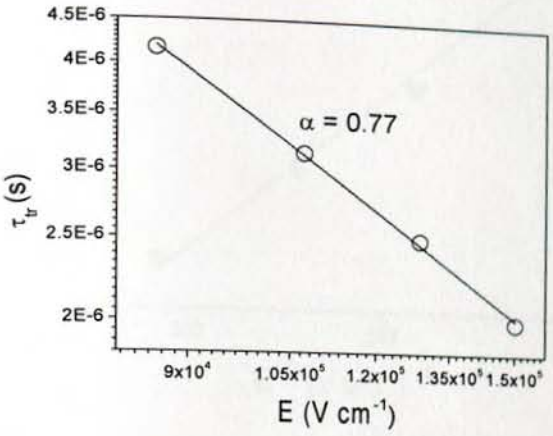

Figure 3.23 Electric field dependence of charge carrier transit time. The dispersion parameter value α is 0.77 and shown on the plot.

As shown in Figure 3.23 the transit time decreased with the increase of applied field as expected for a dispersive transport. The dispersion parameter in DISCL (0.77) is much higher than AS (0.39), which could be the result of thickness and morphology difference due to the solvent difference of film formation process in the two techniques. The characteristic temperature for the energy distribution of traps in DISCL is calculated to be 399 K which is very lower than AS that may be the reason for the fast transition in this measurement.

Based on the transit time the mobility of the polymer has been determined by using Equation 1.16. The calculated mobility as a function of square root of applied field is shown in Figure 3.18 and analyzed based on Poole-Frenkel relations, Equation 1.4. The good linear fit indicates that it follows the Pool-Frenkel relation, Figure 3.24.

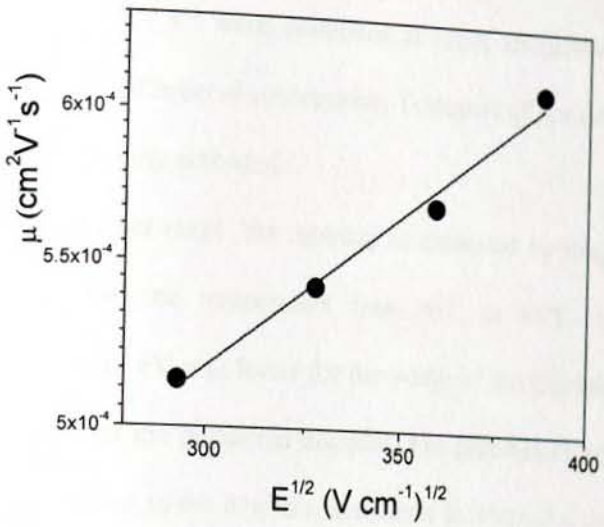

Figure 3.24 Semi-logarithm plot of square root field dependence of charge-carrier mobility for an ITO/PEDOT:PSS/APFO-Green 5/Al. The line indicates the linear fit of the experimental data.

3.2.3 Conclusion

The mobility achieved for APFO-Green 5 in AS at the highest field (3.5×10^5 V cm^{-1}), close to 2×10^{-5} cm^2 V^{-1} s^{-1}, is in excellent agreement with that already reported by Andersson and coworkers [145] for the hole-mobility of the same polymer evaluated by using CELIV technique. For these reasons, we believe that charge transport in the investigated structures is hole-dominated and the peak observed in the susceptance spectra are related to the transit times of positive carriers, though the occurrence of a weak electron-injection at the Al electrode, affecting the admittance low-frequency response. This suggests that bulk techniques should be more suitable for the investigation of transport properties of organic materials to be used in applications requiring sandwiched device structures, such as solar cells or light-emitting diodes.

The electric field dependence of hole mobility in thin films of APFO-Green 5

has been investigated with temperature by admittance spectroscopy. Mobilities of the order of 10^{-6}–10^{-5} cm^2 V^{-1} s^{-1} were calculated at room temperature from the peak positions of the negative differential susceptance. Transport of positive charges carriers is strongly field and thermally activated.

In the investigated field range, the mobility is enhanced by roughly one order of magnitude by increasing the temperature from 4°C to 64°C. Using the GDM formalism, a value of 0.14 eV was found for the width of the Gaussian distribution of energy states and 3.86 for the positional disorder. The parameters extracted by fitting the mobility data according to the disorder formalism indicate that charge transport in spin-coated thin films of APFO-Green5 is greatly affected by high energetic and positional disorder, justifying the moderate mobility values.

The mobility values determined with DISCL technique is one order of magnitude larger than the AS and CELIV techniques. From Poole-Frenkel fit to experimental data, the $\mu_o = 3x10^{-4}$ cm^2 $V^{-1}s^{-1}$ and $\gamma = 1.8x10^{-3}$ $(V\ cm^{-1})^{-1/2}$ were determined. Here the Poole-Frenkel constant is in the same order of magnitude with that of AS. γ can be considered as measure of the sensitivity of the mobility with respect to the applied electric field [145]. Therefore, the hole mobility is equally sensitive to electric field in AS and DISCL for this polymer.

In conclusion the DISCL measured values are one orders of magnitude higher than AS and CELIV techniques. Moreover its potential window is very narrow. Therefore, this technique may not be suitable for the study of such polymer materials as that of AS.

3.3 Transport property of a novel phenyl-substituted polythiophene

Polythiophene and its derivatives constitute one of the most promising classes of conjugated polymers and have been widely used in solution-processed polymer solar cells [92] and field-effect transistors [146], as well as in the fabrication of light-emitting diodes [147].

In order to tune their electronic properties to meet the request for different applications, chemical modifications of polythiopene derivatives have been performed. One method to tailor the electronic properties is the introduction of substituents on the thiophene rings [148]. Substituents can influence the electrical, electrochemical, and optical properties of the resulting polymers, other than modifying their processability in organic solvents. Depending on their nature, size and position, substituents can affect the interaction between polymer chains or induce a distortion of the polymer backbone, resulting in the variation of the π-conjugation of the aromatic system.

Phenyl-substituted polythiophenes have been already reported in the literature, showing how the phenyl substituents affect the electrochemistry [149], the light emission properties [150], as well as the photoinduced charge transfer behaviour [151]. However, the effect of the phenyl-substitution on the transport properties of this class of polythiophenes has not been thoroughly investigated.

Therefore, in this section the characterization of a novel polythiophene derivative, poly[3-(2'-pentyloxy-5'-(1"'-oxooctyl) phenyl)thiophene] (PPOPT), Figure 3.25, is discussed. In addition to the optical and electrochemical characterization, the investigation of bulk transport properties of positive carriers in thin films of PPOPT is described [152].

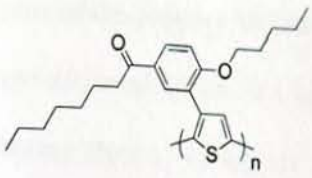

Figure 3.25 Molecular formula of poly[3-(2'-pentyloxy-5'-(1'''-oxooctyl) phenyl)thiophene] (PPOPT).

3.3.1 Optical study

The optical properties of PPOPT were investigated by UV-Vis absorption and PL spectroscopy. The normalized spectra, in a diluted chloroform solution (10^{-5} mol L^{-1}) and in thin film spin-coated onto quartz substrate, are shown in Figure 3.26. The polymer exhibits absorption maxima at 487 nm and at 501 nm, in solution and in thin film, respectively, leading to a red-shift of 14 nm in the solid state. An optical energy gap of 2.0 eV was estimated from the absorption onset of the film. In addition, while the absorption spectrum in solution is structureless, the appearance of a relatively weak shoulder at ~ 580 nm is visible in the solid state. This feature, along with the moderate red-shift of the spectrum when going from solution to thin film, is an indication of moderate interactions between the polymer chains in the solid state [153] or a larger overlap of π orbitals on the polymer backbone due to an increased coplanarity of the thiophene rings in the solid state induced by alignment of the alkyl chains [154]. The narrowing of the PL band in the solid state (full width at half maximum is 0.25 eV in film and 0.36 eV in solution) seems to support a well ordered solid state induced by the substituents on the phenyl ring [155].

Stokes shifts are low and similar in solution and in film (0.38 eV in solution and 0.35 eV in film), suggesting a moderate distortion of the excited state respect to the ground state [156]. Photoluminescence quantum yield in solution (0.11) is relatively

high pointing out a good planarity of the polymer backbone, accordingly, solid state PL quantum yield is high (0.11) and this must be due to a well ordered polymer backbone that is separated from neighboring chains, making the interchain interactions small. This is achieved with attachment of two side-groups on the opposite ortho and meta positions of the phenyl ring which will force the phenyl out of the backbone plane, and thereby separate the polymer chains from each other [155, 157].

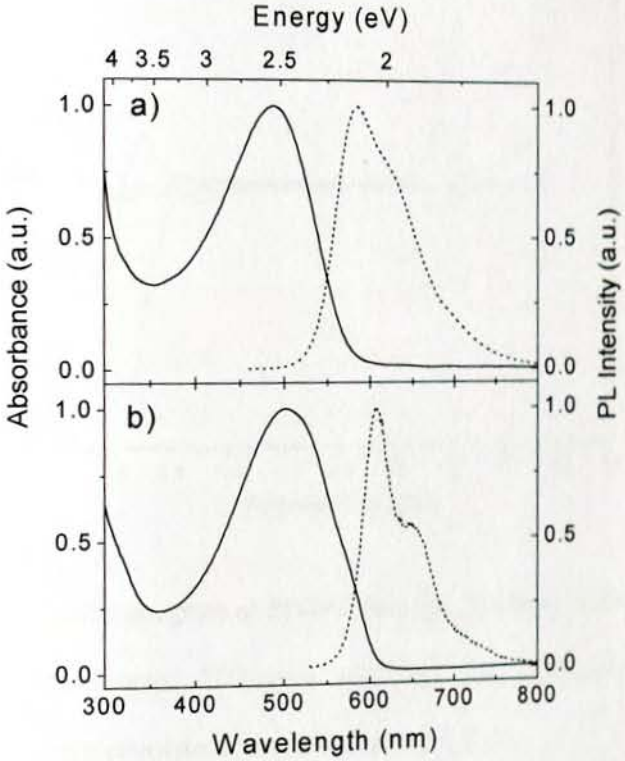

Figure 3.26 Normalized UV-Vis absorption and PL spectra of PPOPT in chloroform solution (a) and in spin-coated film onto quartz substrate (b). The excitation wavelengths were 445 nm and 500 nm, in solution and in film, respectively.

3.3.2 Electrochemical study

Electrochemical cyclic voltammetry measurements were carried out on PPOPT films spin-coated onto ITO/glass substrate, used as working electrode. As shown in Figure 3.27 a quasi-reversible oxidation wave, with the onset potential of 0.81 V *vs.* SCE, and a quasi-reversible reduction wave, with the onset potential of −1.54 V *vs.* SCE, were observed.

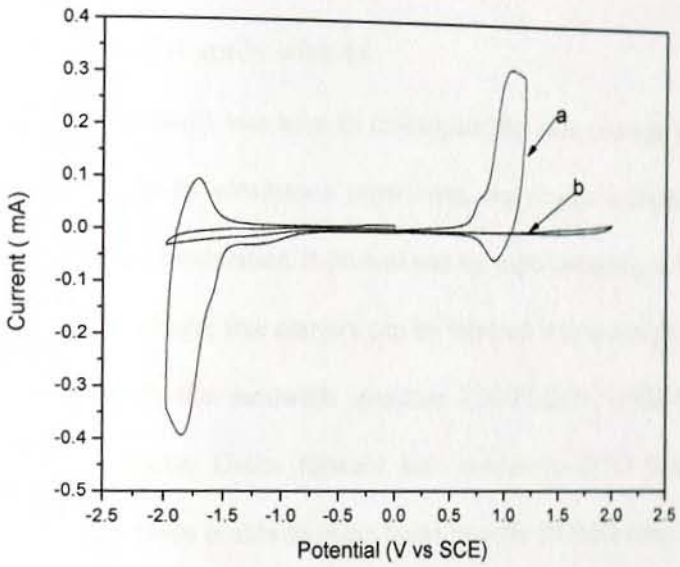

Figure 3.27 Cyclic voltammogram of PPOPT film ((a), first scan) and background (b), spin-coated onto ITO/glass electrode, in $(C_4H_9)NClO_4$/acetonitrile supporting electrolyte at a scan rate of 100 mV s^{-1}.

If compared to a similar phenyl-substitued polythiophene, poly (3-[2'-pentyloxy-5'-(octyl) phenyl]thiophene) [149], the relevant shift of the reduction wave toward less negative potentials (of around 0.5 V) could be attributed to the conjugation of ketone in *meta*-position of the phenyl side-group.

The energy levels of the highest occupied and the lowest unoccupied molecular orbitals (HOMO and LUMO, respectively) were calculated to be – 5.49 eV and –3.14 eV, respectively, from the onset oxidation and reduction potentials, assuming the SCE level at – 4.68 eV [158]. As often observed for conjugated polymers, the electrochemical energy gap was found to be slightly higher than the optical energy gap. This could be related to structural differences in the thin film due to swelling by the solvent, or to the exciton binding energy for conjugated polymers [159].

3.3.3 Transport study with AS

Admittance spectroscopy was used to investigate the bulk average hole mobility in thin film of PPOPT. In an admittance experiment, the charge relaxation driven by a small harmonic voltage modulation is probed and by superimposing a forward dc bias, V_{dc}, to the harmonic voltage, free carriers can be injected into a sample having a diode structure. Devices with the sandwich structure ITO/PEDOT: PSS/PPOPT/Al were prepared for this purpose. Under forward bias conditions (ITO positively biased), ITO/PEDOT:PSS electrode is able to inject holes into the HOMO level of the polymer, while an energy barrier for electron injection of around 1 eV is expected at the Al/PPOPT interface, Figure 3.28. So the aluminum top contact acts as an electron-blocking contact in the investigated hole-only devices under forward bias.

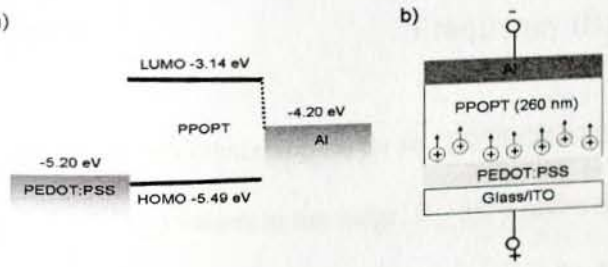

Figure 3.28 Energy diagram and structure of hole-only devices used in this study.

Upon injecting charge carriers, by applying a dc bias V_{dc} to the sample, dramatic changes are observed for admittance Y. As expected, conductance increases by increasing V_{dc}, as shown in Figure 3.29a for the sample ITO/PEDOT:PSS/PPOPT/Al, however, charge injection also affects capacitance spectra.

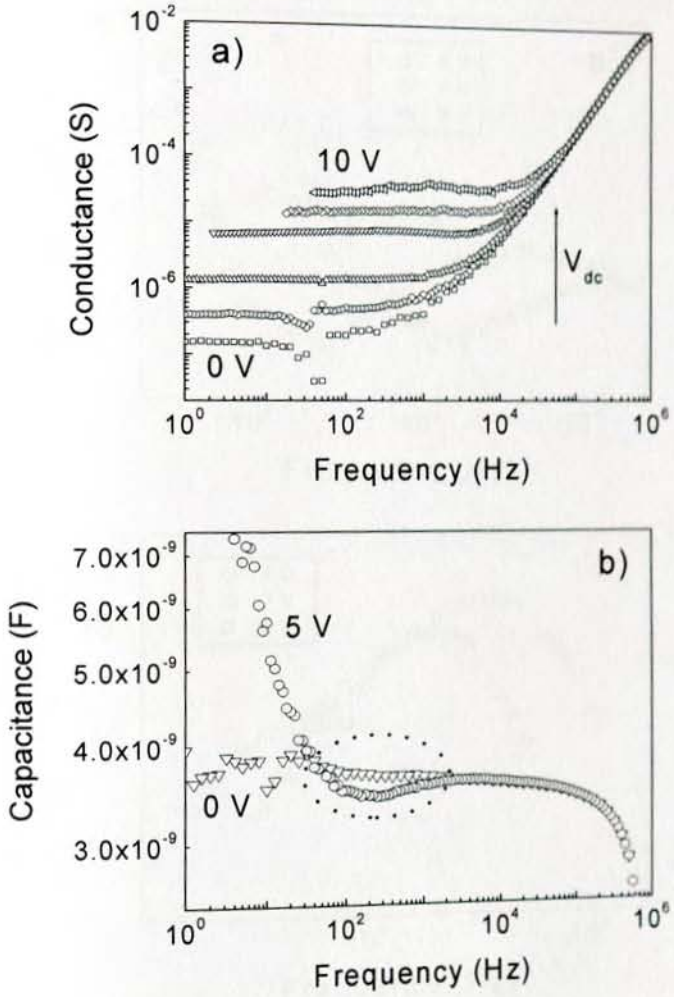

Figure 3.29 (a) Conductance spectra for an ITO/PEDOT:PSS/PPOPT/Al device, for dc bias (V_{dc}) values in the range 0 – 10 V and with a step of 2 V. The arrow indicates the direction of increasing V_{dc}. (b) Capacitance spectra for an ITO/PEDOT:PSS/PPOPT/Al device at dc bias of 0 V and 5 V.

While at zero bias (no injection) capacitance is nearly frequency independent, under high-injection conditions and for one-carrier devices, C usually shows a light minimum in the intermediate frequency range. As an example, the capacitance spectrum obtained for an ITO/PEDOT:PSS/PPOPT/Al sample at $V_{dc} = 5$ V is shown in Figure 3.29b and compared with that at $V_{dc} = 0$.

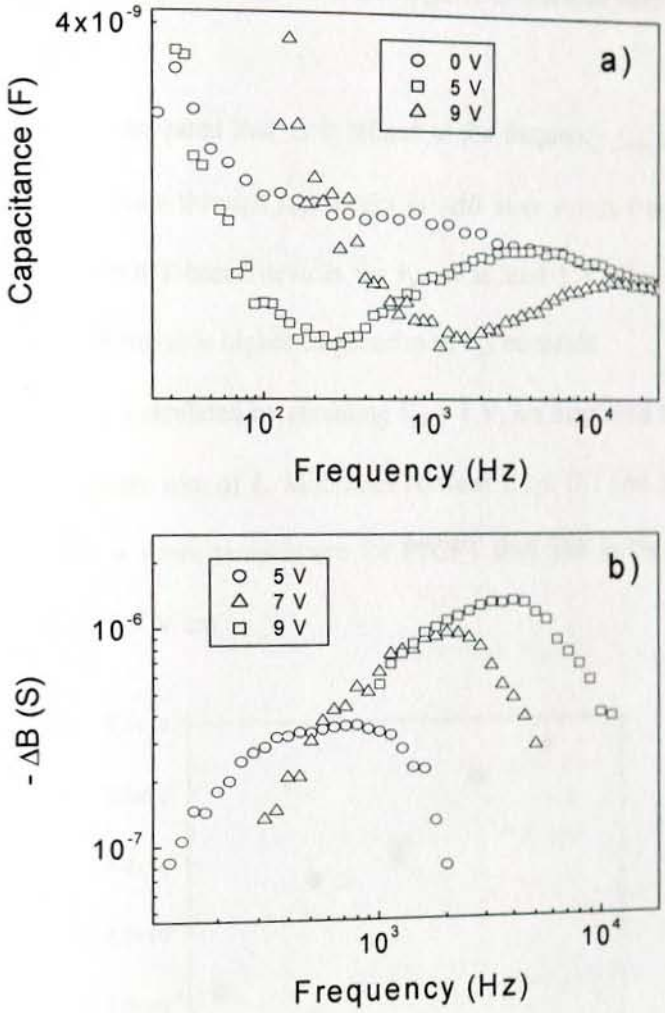

Figure 3.30 Intermediate-frequency range capacitance (a) and negative differential susceptance spectra (b) for an ITO/PEDOT:PSS/PPOPT/Al device at different dc bias (values shown in the figure).

The positive contribution to C in the low frequency range, with respect to zero-bias conditions, is often observed for disordered materials and has been attributed to trapping and subsequent detrapping of charge carriers [52]. The minima in the capacitance spectra are better displayed in Figure 3.30a and the figure also shows their shift toward higher frequency as the dc bias increases. The average transit time, τ_{tr}, of charge carriers can be easily evaluated from the negative differential subsceptance $-\Delta B$, Figure 3.30b.

It has been demonstrated that τ_{tr} is related to the frequency f_{max} at which $-\Delta B$ exhibits its maximum value through f_{max}. Peaks in $-\Delta B$ plots versus frequencies were clearly observed for PPOPT-based devices for V_{dc} of at least 5 V, Figure 3.30b. The peaks increase and shift towards higher frequencies as V_{dc} increases.

The values of μ, calculated by assuming V_{bi} = 1 V, are displayed in Figure 3.31 as a function of the square root of E. Mobilities between 2.1 x 10^{-7} and 5.6 x 10^{-7} cm^2 V^{-1} s^{-1} were obtained at room temperature for PPOPT thin film in the electric field range 1.9 x 10^5 – 3.5 x 10^5 V cm^{-1}.

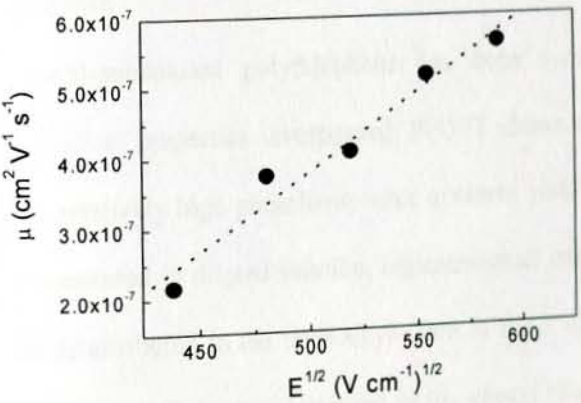

Figure 3.31 Square-root field-dependence of the average hole mobility for an ITO/PEDOT:PSS/PPOPT/Al device. The line represents the linear fit to the experimental data.

These values are orders of magnitude lower than that recently reported for another phenyl-substitute polythiophene [160], poly [3-(4-n-octyl)-phenylthiophene] (POPT) [161]. Indeed, a bulk hole mobility of 1.0×10^{-4} cm^2 V^{-1} s^{-1} has been demonstrated for POPT films, comparable with that measured for regioregular poly (3-hexylthiophene) (P3HT) in the same experimental conditions. This indicates that the substitution of the solubilizing alkyl chain of P3HT with the phenyl-alkyl group of POPT leads to a similar organization of polymer chains in the solid state, profitable for charge transport. Differently, the 2'-pentyloxy-5'-(1'''-oxooctyl) phenyl substituent in PPOPT likely prevents interactions between adjacent polymer chains due to its steric effect, resulting in a strong negative effect for charge transport. The rough linear trend of the plot displayed in Figure 3.31 indicates that hole mobility in PPOPT thin films follows the Poole-Frenkel expression [28,162].

The parameters for the Poole-Frenkel fit to mobility data of Figure 3.30 are $\mu_0 = 1.77 \times 10^{-8}$ cm^2 V^{-1} s^{-1} and $\gamma = 6.0 \times 10^{-3}$ $(V\ cm^{-1})^{-1/2}$. The value of γ is rather high, indicating a strong dependence of hole mobility on electric field.

3.3.4 Conclusion

A novel phenyl-substituted polythiophene has been synthesized and its electrochemical and optical properties investigated. PPOPT shows an optical energy gap of 2.0 eV and its relatively high photolumiscence quantum yield in the solid state (0.11), equal to that measured in diluted solution, indicates small interactions between polymer chains. This is attributed to the long alkyl-chain of the 2'-pentyloxy-5'-(1'''-oxooctyl) phenyl substituent which causes twisting of the phenyl ring out of the plane and leads to poor electronic interaction of the thiophene chains.

This picture is confirmed by the investigation of the bulk transport properties of PPOPT. Hole mobility in thin films of PPOPT was found to be moderate (of the order

of 10^{-7} cm^2 V^{-1} s^{-1} for an electric field of 10^5 V cm^{-1}) and strongly field-activated, as indicated by the rather high value (6.0×10^{-3} $(V\ cm^{-1})^{-1/2}$) of the Poole-Frenkel parameter describing the field dependence of mobility. The present study demonstrates the importance of substituents for the π-conjugation of the aromatic system of polymer materials and how dramatically they can affect the electronic properties.

3.4 Bulk-heterojunction solar cells of a random co-polymer (PFB-co-FT)

Several groups have devoted to designing new optimized conjugated polymers, improving efficiency, and decreasing the cost of processing for device fabrication. Low band gap conjugated polymers with main chain alternating donor/acceptor (D – A) structure are promising, which can broaden the absorption to the red and even to the near IR region and result in higher PCE [163].

Functional groups such as fluorene [164 – 168], carbazole [169, 170], silafluorene [171], cyclopentadithiophene [172 – 174], N-substituted dithienopyrrole [175,176] and dithienosilole [177], have been used as donor moieties; whereas, functional groups such as benzothiadiazole [178], quinoxaline [179], diketopyrrolopyrrole [180], thienopyrazine [181], fluoranthene [182] and so on were usually used as acceptor moieties.

The rigid conjugated polymers are usually required to carry flexible side chains to ensure that polymers have certain solubility in organic solvents. The lengths of alkyl chains play an important role in molecular weights, energy levels of conjugated polymers, morphologies of blend films, and therefore the photovoltaic performance of devices [183, 184]. Moreover, the position of alkyl chain on each D-A repeat unit is also a key point in tailoring polymer structures [185 - 187]. Recently a benzothiadiazole moiety demonstrated a PCE of 5.4% [188].

In this study, a photovoltaic characterization of a novel family of fluorene – thiophene-benzothiadiazole containing, poly{[4'-(9,9-bis(2-ethylhexyl)fluoren-2-yl)-2',1',3'-benzothiadiazole-7,7'-diyl]-co-[2'-(9,9-bis(2-ethyl-hexyl)fluoren-2-yl)thien-7,5'-diyl]} (PFB-co-FT, Figure 3.32), random copolymers is described [189]. The study includes selection of the best solvent, analyzing annealing effects, optimization of polymer: PCBM weight ratio, optimization of the active layer thickness and studying

the effect of LiF buffer layer in order to get optimized performance. The effect of the incident light intensity was also investigated in order to get insight about the space charge effect on the device.

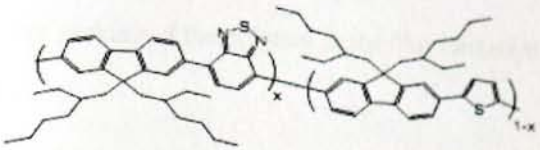

Figure 3.32 Molecular structure of PFB-co-FT.

3.4.1 Optical study

The absorption spectrum of thin film of PFB-co-FT is shown with the background of solar irriadiation spectrum at air mass 1.5 (AM 1.5) in Figure 3.33. The peak position of the film indicates that the polymer material absorbs in the maximum intensity position but very narrow region of the sun spectrum and hence a poor performance is expected as it was confirmed below. One of the reasons could be its large band gap, 2.74eV.

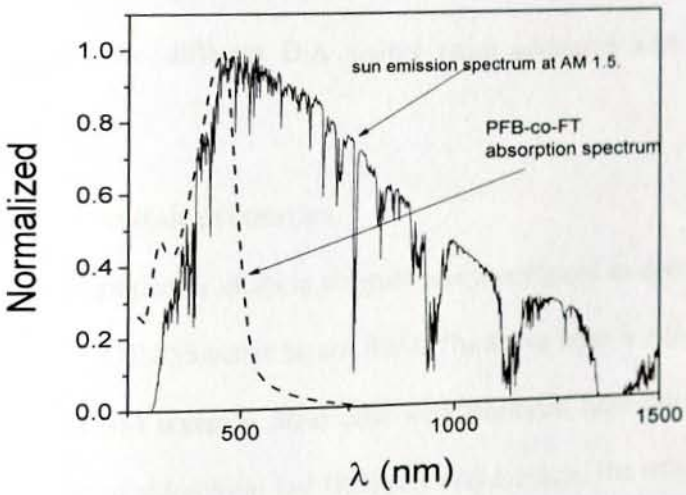

Figure 3.33 Absorption spectrum (normalized) of thin film PFB-co-FT with the background of sun emission spectrum at AM 1.5.

When the UV-Vis spectra of the polymer film blended with PCBM with different weight ratio is analyzed, there is no significant peak position change as compared to the pristine polymer, Figure 3.34. This indicates that the presence of PCBM does not have a significant influence on the polymer inter-chain interaction and no significant effect on the packing of the polymer in the film formation.

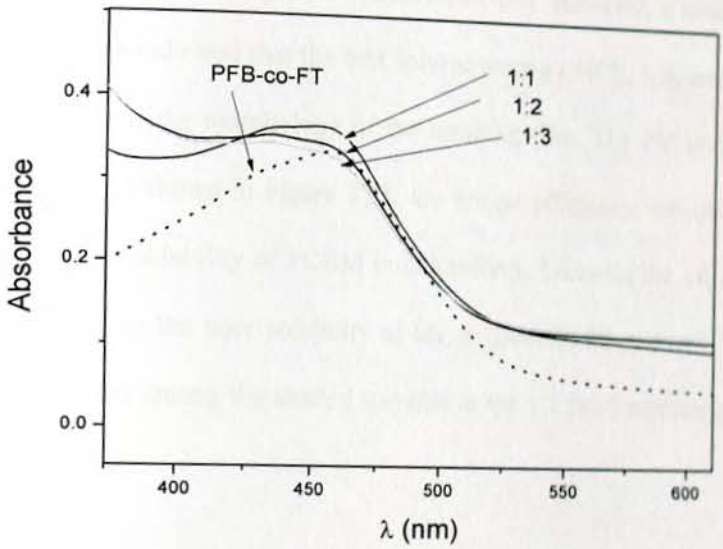

Figure 3.34 Absorption spectra of PFB-co-FT:PCBM films spin-coated on quartz substrates for different D:A weight ratios compared with PFB-co-FT pristine film.

3.4.2 Photovoltaic properties

Photovoltaic properties of these polymer was investigated in devices with the structure of ITO/PEDOT:PSS/active layer/LiF/Al. The active layer is a blend of PFB-co-FT donor and PCBM acceptor. Solar cells were fabricated from chloroform, CB, DCB, or the mixture of chloroform and DCB (1:1 v/v) solution. The ratio of donor to acceptor and the thickness were optimized. Optimum performance was always achieved with a mixture of chloroform and DCB (1:1 v/v) solvents, a ratio of polymer

to PCBM of 1:2 (w/w) and an active layer thickness in the range of 90 nm to 100 nm and the summary of the result is shown in Table 3.2.

3.4.2.1 Selection of solvent

The effect of three different solvents was studied: chloroform ($CHCl_3$), chlorobenzene (CB) and dichlorobenzene (DiB), and in a mixture form. According to the literature the CB and DiB are good solvents for PCBM. However, a solubility test of PFB-co-FT polymer indicated that the best solvent among $CHCl_3$, CB, and DiCB is $CHCl_3$ as deduced from the morphology of the resulting film. The PV investigation also confirmed this. As shown in Figure 3.35, the lowest efficiency was observed in $CHCl_3$ due to the poor solubility of PCBM in chloroform. Likewise the efficiency in CB was also low due to the poor solubility of the polymer in this solvent. The best efficiency was observed among the studied solvents in the 1:1 (v/v) mixture of $CHCl_3$ and CB.

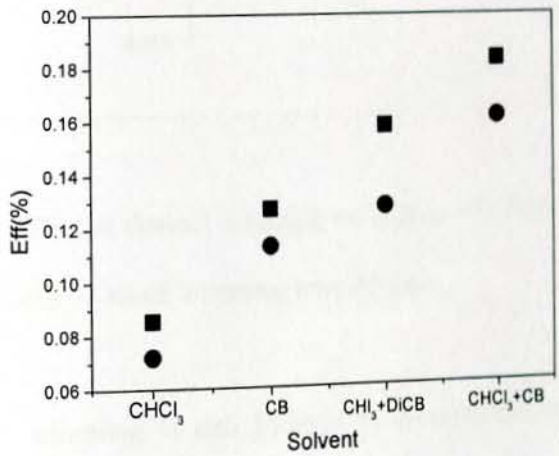

Figure 3.35 Effect of solvent on PFB-co-FT:PCBM (1:1w/w) solar cells with different solvents. ITO/PEDOT:PSS/active layer/Al. Thickness of around 130 nm.; squares indicate maximum values and circles indicate average values on eight cells.

3.4.2.2 Study of annealing effect

The effects of thermal and solvent annealing were studied for PFB-co-FT:PCBM solar cells.

The effect of thermal annealing was tested on complete device by applying different temperatures in Argon atmosphere-glove box for 30 min. However the thermal annealing has shown a negative effect in all cases, Figure 3.36.

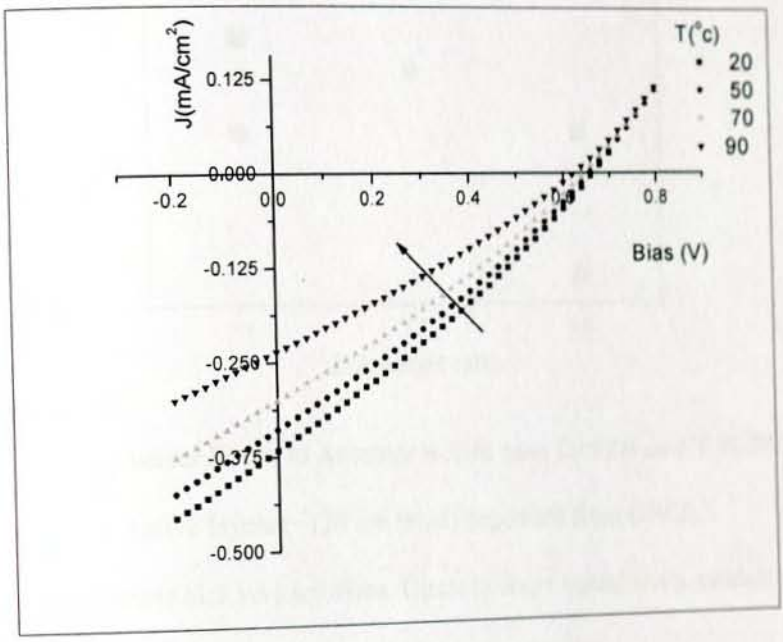

Figure 3.36 Effect of thermal annealing on PFB-co-FT: PCBM (1:1 w/w) solar cells ~130nm; annealing time 30 min.

The solvent annealing is also believed to increase the aggregation of the polymer and improve the morphology of the film of the active layer. Therefore, a test was done on devices in chlorobenzene environment for 30 min, before the top Al deposition. However, it did not show any significant change in efficiency of the devices.

3.4.2.3 Donor to Acceptor weight ratio

In order to choose the best blend composition, active layers with D:A w/w ratios 1:1, 1:2, and 1:3 were studied, Figure 3.37. The maximum value of current density and corresponding efficiency was observed with 1:2 D:A weight ratio.

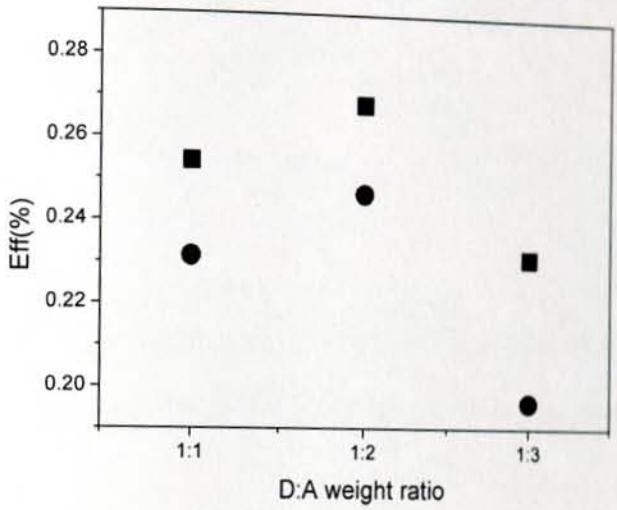

Figure 3.37 Efficiency verses Donor to Acceptor weight ratio for PFB-co-FT:PCBM solar cells. Active layers (~120 nm thick) deposited from $CHCl_3$ /Chlorobenzene (1:1 v/v) solutions. Circle average values (on a number of cells between 4 and 8) and square dots maximum values.

3.4.2.4 Effect of LiF buffer layer

Complete devices without LiF and with 0.6 nm LiF were developed with 1:2 donor to acceptor weight ratio in order to study the effect of LiF buffer layer underneath of Al metal electrode.

The presence of LiF buffer layer has increased the Jsc, Figure 3.38. Practically the presence of LiF buffer is expected to facilitate the electron transport to the collecting electrode resulting the increase in current density.

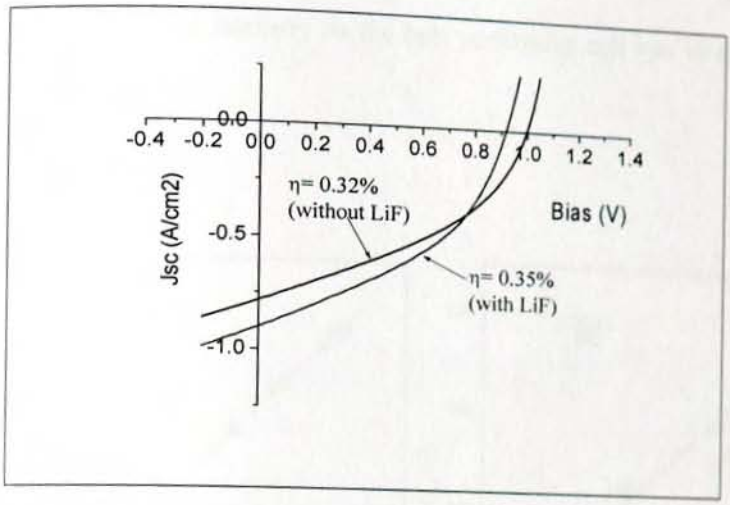

Figure 3.38 Effect of LiF buffer layer for a PFB-co-FT: PCBM solar cell (1:2 w/w), deposited from a $CHCl_3$/ Chlorobenzene (1:1 v/v) solution to a thickness of ~100nm.

3.4.2.5 Thickness optimization

Different devices with different active layer thickness were developed and characterized. From Figure 3.39, the optimal thickness to achieve the best efficiency is around 100 nm.

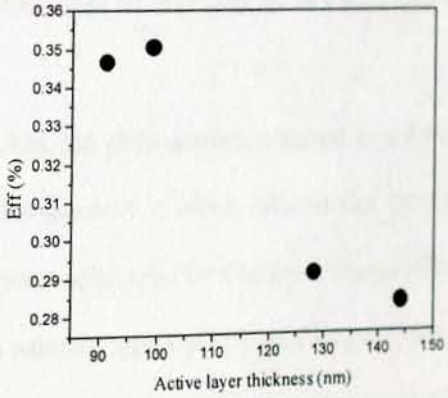

Figure 3.39 Efficiency versus active layer thickness for PFB-co-FT:PCBM (1:2 w/w) solar cells deposited from $CHCl_3$/ Chlorobenzene (1:1 v/v) solutions.

3.4.2.6 Illumination intensity study

In order to get insight about the performance of the PV of this polymer, the effect of incident light intensity on the best performing cell was investigated, Figure 3.40.

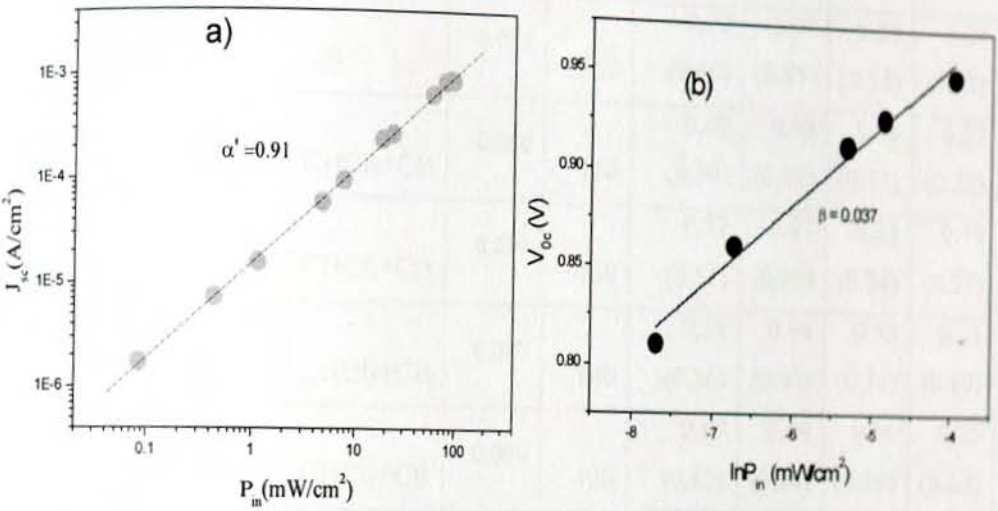

Figure 3.40 Short-circuit current(a) and Open circuit voltage (b) as a function of the incident light intensity for a PFB-co-FT:PCBM (1:2 w/w) solar cell, deposited from a $CHCl_3$ /Chlorobenzene (1:1 v/v) solution to a thickness of ~100 nm.

As shown in Figure 3.40a, the photocurrent analyzed as a function of incident light intensity the slope remains around 0.9, which indicate that there is no significant space charge effect on this polymer solar cell (for free space charge effect $\alpha' = 1$) [190]. Likewise, when the V_{oc} versus natural logarithm of power intensity plot is analyzed the slop (β) is above 25 mV, Figure 3.40b. This indicates that the recombination type in this system is accounted to be trap assisted bimolecular recombination, which leads to loss of fill factor [191].

Table 3.2 Summary of photovoltaic parameters of PFB-co-FT:PCBM solar cells (Averages in parenthesis).

Sample code	PCBM content (% wt)	Solvent	Active area	Thick	Jsc	Voc	FF	Eff
			(cm^2)	nm	mA/cm^2	V		%
6911C+D	50	$CHCl_3$	0.082	120	0.39 (0.35)	0.71 (0.68)	0.29 (0.29)	0.09 (0.07)
6911S+T	50	CB	0.081	130	0.72 (0.60)	1.00 (0.95)	0.39 (0.38)	0.29 (0.23)
6911U+V	50	$CHCl_3$+CB	0.080	150	0.69 (0.59)	0.98 (0.95)	0.38 (0.37)	0.27 (0.22)
6911W+1	50	$CHCl_3$+CB	0.090	130	0.57 (0.51)	0.97 (0.96)	0.33 (0.34)	0.19 (0.17)
6911Y+Z	50	$CHCl_3$+CB	0.090	140	0.59 (0.56)	0.94 (0.93)	0.35 (0.36)	0.21 (0.19)
69112+3	50	$CHCl_3$+CB	0.080	120	0.67 (0.62)	0.99 (0.98)	0.36 (0.36)	0.25 (0.23)
6912G+H	67	$CHCl_3$+CB	0.085	120	0.63 (0.59)	0.97 (0.94)	0.41 (0.42)	0.27 (0.25)
6912I+J	67	$CHCl_3$+CB	0.081	100	0.79 (0.71)	0.99 (0.94)	0.39 (0.39)	0.33 (0.28)
6912K+L	67	$CHCl_3$+CB	0.090	100	0.90 (0.83)	0.92 (0.95)	0.41 (0.38)	0.36 (0.32)
6912M+N	67	$CHCl_3$+CB	0.088	90	0.80 (0.77)	1.01 (0.93)	0.41 (0.39)	0.35 (0.30)
6912O+P	67	$CHCl_3$+CB	0.085	140	0.63 (0.59)	0.99 (0.97)	0.43 (0.43)	0.28 (0.26)
6912Q+R	67	$CHCl_3$+CB	0.085	120	0.67 (0.64)	0.99 (0.97)	0.43 (0.43)	0.30 (0.28)
6913I+J	75	$CHCl_3$+CB	0.085	120	0.52 (0.46)	0.97 (0.93)	0.43 (0.43)	0.23 (0.19)

3.4.3 Conclusion

The polymer PFB-co-FT does not show the sufficient solubility required for solar cell application, at least in the tested solvents. This leads to a very segregated morphology for the polymer:PCBM mixture, as demonstrated by the effects of the thermal annealing treatment. Indeed, these treatments always induce an enhancement of segregation between the two different phases in a D:A blend, so they can be effective only if the segregation level of the starting blend morphology is lower than the "optimum" one for a given D:A couple. Given the poor effects of solvent/thermal treatments, we can conclude that the segregation level of the as-deposited active layers is already too high.

The combination of the lack of control of blend morphology and the poor absorption properties of the polymer leads to the poor PV performance of the solar cells.

The investigation of the trend of Jsc with the light intensity (P_{in}) was done in order to have some indications on the presence of space charge effect. For PFB-co-FT: PCBM solar cells the power factor α' did not change meaningfully and its value is around 0.9 indicating no significant effect of space charge effect.

3.5 BisEH-PFDTBT: PCBM solar cells: a compositional, thickness, and light intensity-dependent study

Conjugated polymers containing alternating electron-rich and electron-poor monomer units represents the most common donor materials used in the fabrication of efficient polymer solar cells. A relevant class of materials with these characteristics is represented by the alternating fluorene copolymers (APFO) [164, 192-194], which leads to solar cells showing promising power conversion efficiencies. In particular, poly{9,9-bisalkylfluorene-2,7-diyl-*alt*-[4,7-bis(thien-2-yl)-2,1,3-benzothiadiazole]-5',5"-diyl} (alkyl = hexyl, octyl, decyl, dodecyl), containing fluorene-thiophene-benzothiadiazole-thiophene units in an alternating sequence, [164,184,195] exhibit energy gaps around 1.9 eV and, thanks to their low-lying highest occupied molecular orbital (HOMO) level, the related solar cells can deliver an open circuit voltage as high as 1 V, when blended with fullerene derivatives.

On the other hand, quite surprisingly few studies exist on APFO bearing branched alkyl chains on the fluorene ring [166]. However, as it has been recently demonstrated and contrary to the common wisdom, the structure of the conjugated backbone is not the only responsible for the energy levels and the device efficiencies [19]. Indeed, for a class of dithienonaphthalene-thiophene-benzothiadiazole-thiophene alternating copolymers it has been shown that 2-ethylhexyl lateral chains lead to the best performance, with power conversion efficiencies almost three times than those observed for polymers bearing octyl chains. Therefore the conclusions on polymers with linear alkyl chains cannot be obviously extrapolated to homologues with branched chains, and for this reason APFO bearing branched chains are worthy of an in-depth examination.

In this study an extended characterization of solar cells made of poly{9,9-bis(2-ethylhexyl)fluorene-2,7-diyl-*alt*-[4,7-bis(thien-2-yl)-2,1,3-benzothiadiazole]-5',5''-diyl} (BisEH-PFDTBT) as the electron-donor and [6,6]-phenyl-C_{61}- butyric acid methylester (PCBM) as electron-acceptor is reported [196]. The dependence of photovoltaic parameters on blend composition, active layer thickness, and light intensity is described, as well as the analysis of photocurrents, with the aim to identify the main loss mechanisms in this photoactive blend.

3.5.1 Effect of blend composition

The absorption spectra of films made of BisEH-PFDTBT and BisEH-PFDTBT:PCBM mixtures are shown in Figure 3.41. The lower-energy peak of the pristine polymer spectrum is slightly red-shifted with respect to the blend in 1:1 D:A ratio, indicating some alteration of the inter-chain interaction in the presence of PCBM. However, the peak absorption wavelength did not further change for films with higher amounts of PCBM, differently from P_3HT:PCBM blends for which significant blue-shifts of the absorption of P_3HT in the visible range were observed with increasing PCBM content, along with the disappearance of the typical vibronic structures of P_3HT [197]. Those spectra modifications were attributed to the disruption of the ordering in the P3HT chains in the presence of PCBM molecules, leading to the lowering of polymer inter-chain interaction.

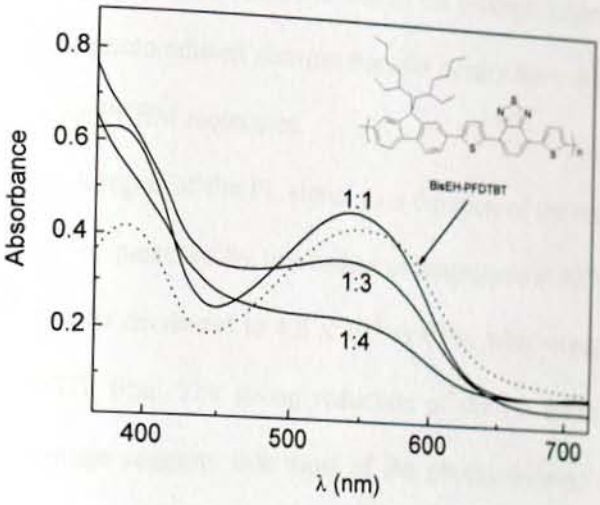

Figure 3.41 Typical absorption spectra of BisEH-PFDTBT:PCBM films spin-coated onto quartz substrates for different D:A weight ratios, compared to that of a BisEH-PFDTBT pristine film.

The typical features of P_3HT absorption spectrum are usually recovered upon thermal annealing of the P_3HT:PCBM composite films[105, 198,199. Differently from P_3HT, BisEH-PFDTBT is an amorphous polymer which does not show the spontaneous tendency to form ordered packed structures in spin-coated films, thus its absorption spectrum is not significantly affected upon blending with PCBM.

The quenching of the donor photoluminescence (PL) was evaluated in BisEH-PFDTBT:PCBM blends with different composition by comparing the integral of the PL signals, calculated in the same wavelength range (574 – 900 nm), Figure 3.42b.

Films with different D:A composition but with the same optical density of around 0.23 at the excitation wavelength (552 nm, corresponding to the low-energy absorption peak of BisEH-PFDTBT) were spin-coated onto quartz substrates. PL quenching is here defined as the ratio of the integrated PL signal of the blend to that of pristine polymer film. The photoluminescence at 552 nm of BisEH-PFDTBT:PCBM

blends is significantly quenched, compared to that of the pristine polymer, Figure 3.42, indicating that efficient photoinduced electron transfer occurs from the donor polymer to the electron-accepting PCBM molecules.

Monitoring the integral of the PL signal as a function of the weight fraction of PCBM reveals that PL is quenched by two orders of magnitude at 33% of PCBM and the PL emission is further decreased to 4.8×10^{-3} at 67%, with respect to that of the pristine BisEH-PFDTBT film. The strong reduction of the PL emission at 67% of PCBM weight percentage suggests that most of the photogenerated excitons in the BisEH-PFDTBT phase are involved in the photoinduced charge transfer process at that blend composition.

Solar cells with the structure ITO/PEDOT:PSS/BisEH-PFDTBT:PCBM/Al were prepared, with a weight percentage of fullerene of at least 50% and with a comparable thickness of the active layer, to study their photovoltaic properties with the blend composition. Representative current-density - voltage (J-V) curves under AM1.5 (100 mW cm^{-2}) irradiation are displayed in Figure 3.43 and the related photovoltaic parameters are collected in Table 3.3.

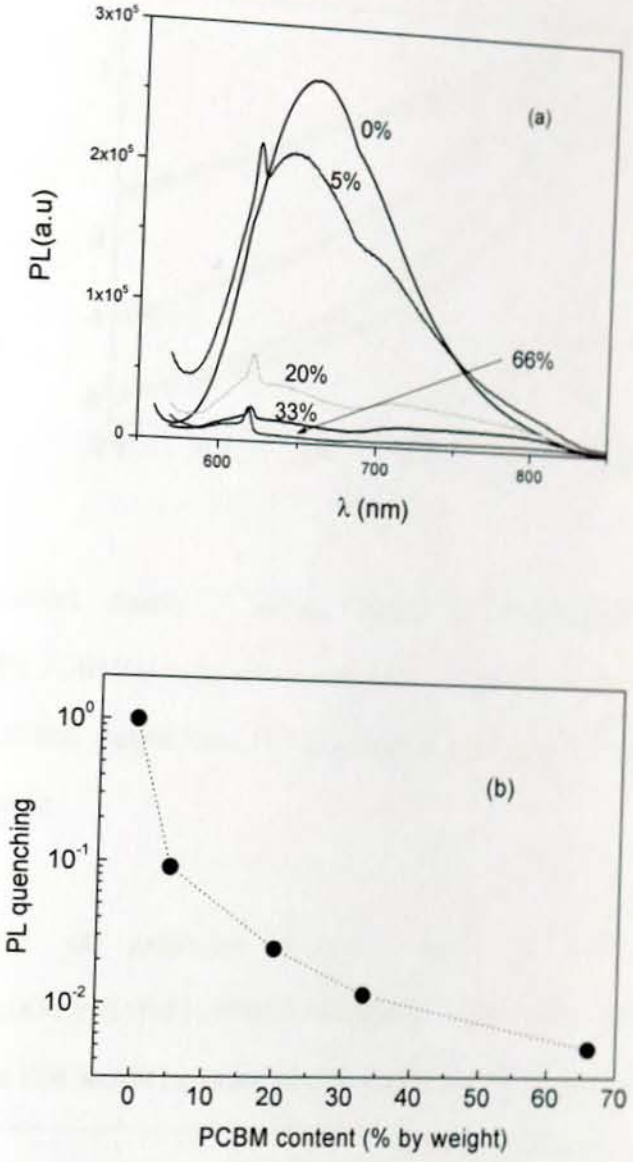

Figure 3.42 Photoluminescence quenching of BisEH-PFDTBT:PCBM films spin-coated onto quartz substrates: (a) photoluminescence spectra; (b) PL quenching for different PCBM weight concentration. The excitation wavelength is 552 nm.

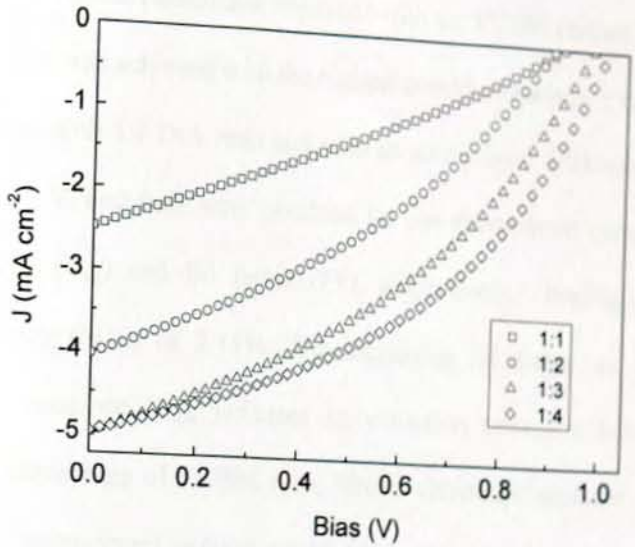

Figure 3.43 Current density - voltage curves of ITO/PEDOT:PSS/BisEH-PFDTBT:PCBM/Al solar cells under AM1.5 (100 mW cm^{-2}) irradiation for different D:A weight ratios: 1:1 (squares); 1:2 (circles); 1:3 (triangles); 1:4 (diamonds).

Table 3.3 Summary of parameters extracted from the J-V curves of ITO/PEDOT:PSS/BisEH-PFDTBT:PCBM/Al solar cells, prepared with different D:A weight ratios and similar thickness of the active layer.

Thickness (nm)	D:A ratio (w/w)	R_s (Ω cm^{-2})	R_{sh} (Ω cm^{-2})	Photovoltaic parameters (AM1.5, 100 mW cm^{-2})			
				J_{sc} (mA cm^{-2})	V_{oc} (V)	FF	PCE (%)
100	1:1	33	4.5×10^3	2.48	0.92	0.29	0.65
110	1:2	24	8.6×10^3	4.03	0.90	0.35	1.27
130	1:3	25	6.1×10^4	4.99	0.98	0.38	1.84
120	1:4	14	1.2×10^6	4.97	1.01	0.42	2.11

All the photovoltaic parameters improved with the PCBM content in the blend. The best performance was achieved with the highest considered acceptor concentration. For the device made with 1:4 D:A ratio and with an active layer thickness of 120 nm, 4.97 mA cm^{-2}, 1.01 V, and 0.42 were obtained for the short-circuit current (J_{sc}), the open-circuit voltage (V_{oc}) and fill factor (FF), respectively, leading to a power conversion efficiency (PCE) of 2.11%. The increasing fill factor, as well as the decreasing series resistance (R_s), indicates an evolution toward a better network formation as the percentage of PCBM rose, likely within the acceptor phase. The slightly increasing open-circuit voltage could be explained by the improved shunt resistance (R_{sh}) (Figure 3.44), undergoing a variation of around three orders of magnitude by passing from 1:1 to 1:4 D:A weight ratio. The drastic increase of R_{sh}, indicating a progressive suppression of leakage currents by increasing the acceptor concentration, could be consistent with the formation, at high PCBM contents, of a vertically segregated blend morphology, leading to an accumulation of the acceptor toward the cathode contact and of the polymer toward the ITO/PEDOT:PSS anode.

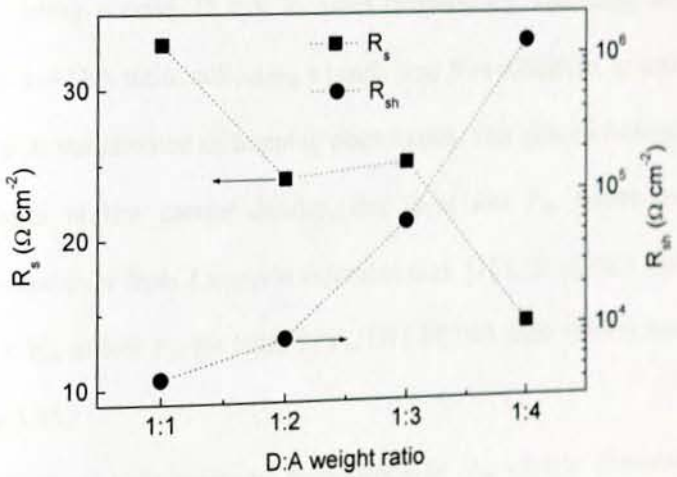

Figure 3.44 Series resistance and shunt resistance of ITO/PEDOT:PSS/BisEH-PFDTBT:PCBM/Al solar cells as a function of blend composition.

3.5.2 Light intensity effect

A light-intensity dependent study was carried out by using a set of neutral quartz filters to attenuate the incident light power (P_{in}). The dependence of V_{oc} on P_{in} is highly affected by the blend composition and is stronger for lower PCBM contents, mainly at low incident light power, Figure 3.45. It has been shown that a linear trend of V_{oc}, when plotted against the natural logarithm of P_{in}, is expected for polymer solar cells in the case of Langevin recombination of charge carriers. In addition, the slope of the linear plot is proportional to the thermal voltage kT/q (k is Boltzmann's constant, T the absolute temperature and q the electronic charge) and is affected by charge trapping phenomena [200].

In the plots shown in Figure 3.45, a linear portion can be detected, limited for lower PCBM concentrations and more extended as the acceptor content was increased.

The values of the slopes calculated from the linear fits are displayed in Figure 3.45b versus the D:A weight ratio of BisEH-PFDTBT:PCBM solar cells. For 1:1 and 1:2 D:A ratios, a slope of around 51 mV was calculated, around twice kT/q, the thermal voltage being around 25 mV at room temperature. The slope decreased to around 28 mV at 1:4 D:A ratio, indicating a nearly trap-free condition, as a slope of just kT/q is expected in the absence of trapping phenomena. The effect of charge trapping on V_{oc} is stronger at low carrier density, that is at low P_{in}, where trap-assisted recombination takes over from Langevin recombination [121, 201], thus justifying the steep increase of V_{oc} at low P_{in} for BisEH-PFDTBT:PCBM solar cells at lower PCBM contents, Figure 3.45.

The analysis of light intensity dependence of V_{oc} clearly demonstrates that charge trapping effects limit the performance of BisEH-PFDTBT:PCBM solar cells with PCBM percentages lower than 80%.

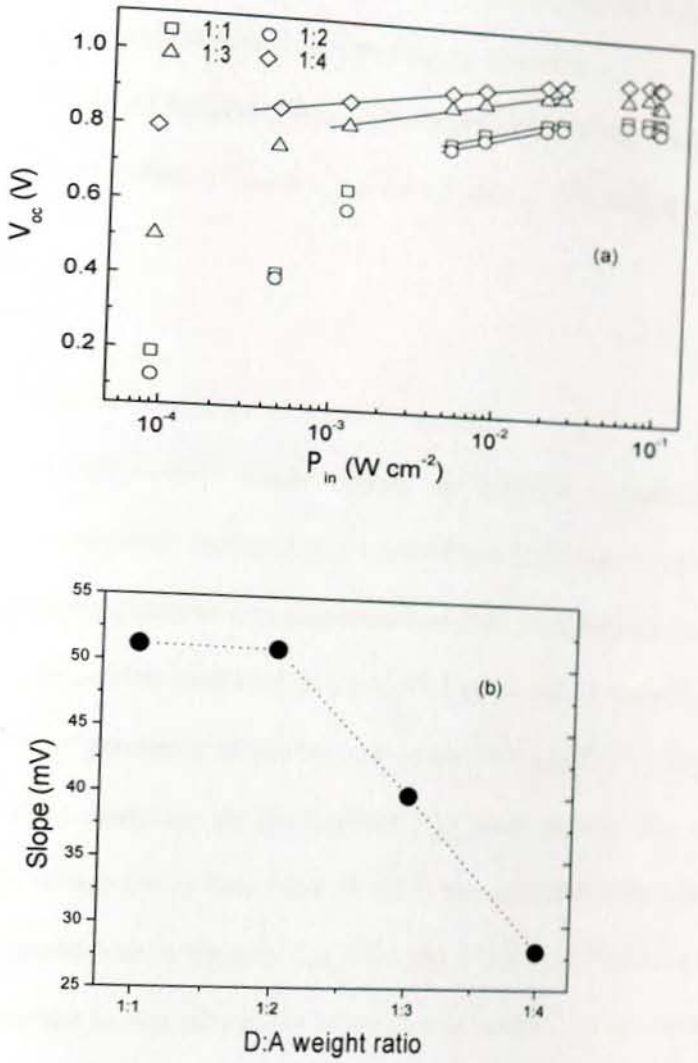

Figure 3.45 (a)Open-circuit voltage of ITO/PEDOT:PSS/BisEH-PFDTBT:PCBM/Al solar cells as a function of the incident light power and for different D:A weight ratios: 1:1 (squares); 1:2 (circles); 1:3 (triangles); 1:4 (diamonds). The lines represent the linear fit to the experimental data. (b) The slopes calculated from the linear fits against the D:A weight ratio.

Likely, the formation of the desired continuous acceptor pathway is only reached with the 1:4 D:A ratio in BisEH-PFDTBT:PCBM blends and for lower

acceptor concentrations electrons are trapped in isolated PCBM aggregates and recombine with charges of opposite sign from the polymer phase.

The occurrence of trapping effects in BisEH-PFDTBT:PCBM solar cells could also explain the lower values of V_{oc} at 1 sun for 1:1 and 1:2 D:A weight ratios (Table 3.3).

3.5.3 Generation of free electron-hole pairs

BisEH-PFDTBT:PCBM blends shows an efficient quenching of the photoluminescence emission. However, it has been shown [202] that the photoinduced charge transfer process generates bound hole-electron (h-e) pairs, because of the strong Coulomb interaction, which could be dissociated into free carriers or recombine.

The ability of generation of free h-e pairs in BisEH-PFDTBT:PCBM solar cells was investigated by analyzing the photocurrent (J_{ph}) under reverse bias conditions [203]. A reverse voltage sweep from 1.2 V to -12 V was applied to solar cells and the current was measured both in the dark (J_D) and under white light irradiation (J_L). The effective photocurrent J_{ph} was obtained by subtracting J_D from J_L. As an example, J_{ph} is displayed in Figure 3.46a in a double logarithmic scale as a function of the effective voltage V_0-V for 1:2 and 1:4 D:A ratios, V_0 being the voltage at which J_{ph} is zero and V the externally applied voltage.

The generation rate of free carriers is dependent on charge carrier mobility, other than on the electric field and temperature. The dependence of J_{ph} on field is stronger for lower PCBM concentrations in BisEH-PFDTBT:PCBM solar cells, indicating better transport properties for higher acceptor concentrations, as often reported for polymer solar cells [190]. From the analysis of the trend of J_{ph} with the effective voltage it is evidenced by a slope of 0.5 in an intermediate range of the

voltage. This is consistent with the nearly linear relationship of J_{sc} with P_{in} observed for all considered blend compositions. For all D:A ratios, J_{ph} reached the saturation at high reverse bias (Figure 3.46), indicating that all photogenerated bound h-e pairs are dissociated into free carriers. From the saturation current (J_{sat}), the generation rate of bound h-e pairs G_{max} was calculated with Equation 1.31 and its value ranged between 4.0×10^{21} and 6.1×10^{21} cm^{-3} s^{-1} for BisEH-PFDTBT:PCBM solar cells, the latter value being related to the 1:1 D:A blend which for comparable thickness absorbs more light. A clear dependence of the percentage of charge generation on BisEH-PFDTBT:PCBM blend composition, Figure 3.46b, with respect to its maximum possible value G_{max}, was found at short-circuit condition (V = 0) and at the voltage V_{MPP} corresponding to the maximum power point of the J-V curve. As expected, both at V = 0 and V = V_{MPP}, the charge generation ability reached its highest value for 1:4 D:A ratio, with values of 64% and 38%, respectively. At 50% by weight of PCBM, those percentages were reduced to 39% and 21%, respectively.

Even for the most efficient blend composition, more than one third of the photogenerated bound h-e pairs does not lead to the formation of carriers free to move, indicating that this step is a major limiting factor of the performance of BisEH-PFDTBT:PCBM solar cells.

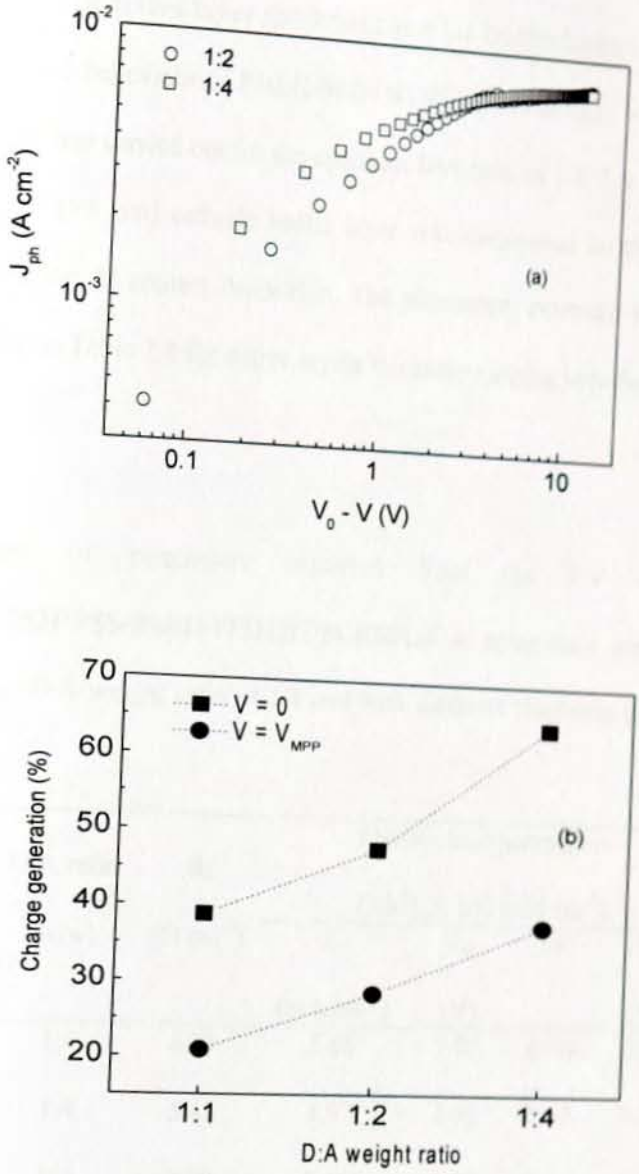

Figure 3.46 (a) Effective photocurrent against the effective voltage of ITO/PEDOT:PSS/BisEH-PFDTBT:PCBM/Al solar cells, under white light irradiation (AM1.5, 100 mW cm^{-2}), for 1:2 (circles) and 1:4 (squares) D:A weight ratios. (b) Probability of charge generation at short-circuit condition and at the maximum power point is displayed against the D:A weight ratio.

3.5.4 Effect of active layer thickness and LiF buffer layer

A study of the behaviour of BisEH-PFDTBT:PCBM solar cells with the active layer thickness was also carried out for the optimum D:A ratio of 1:4. For better device optimization, a LiF (0.8 nm) cathode buffer layer was evaporated on the top of the active layer before the Al contact deposition. The parameters extracted from the J-V curves are reported in Table 3.4 for active layers thickness ranging between 90 nm and 160 nm.

Table 3.4 Summary of parameters extracted from the J-V curves of ITO/PEDOT:PSS/BisEH-PFDTBT:PCBM/LiF/Al solar cells, prepared with the same D:A weight ratio of 1:4 and with different thickness of the active layer.

Thickness (nm)	D:A ratio (w/w)	R_s (Ω cm^{-2})	Photovoltaic parameters (AM1.5, 100 mW cm^{-2})			
			J_{sc} (mA cm^{-2})	V_{oc} (V)	FF	PCE (%)
160	1:4	8.91	5.66	1.05	0.40	2.43
125	1:4	5.42	4.97	1.05	0.42	2.25
100	1:4	3.90	5.16	1.07	0.46	2.57
90	1:4	2.25	5.02	1.04	0.47	2.46

The LiF buffer layer assists in the collection of negative carriers and, as reported by Brabec et al [111], it decreases the cathode contact resistance, resulting in a reduced series resistance of solar cells, Table 3.4. The parameters most affected by the

active layer thickness were the series resistance and fill factor, indicating charge transport limitation in BisEH-PFDTBT:PCBM solar cells.

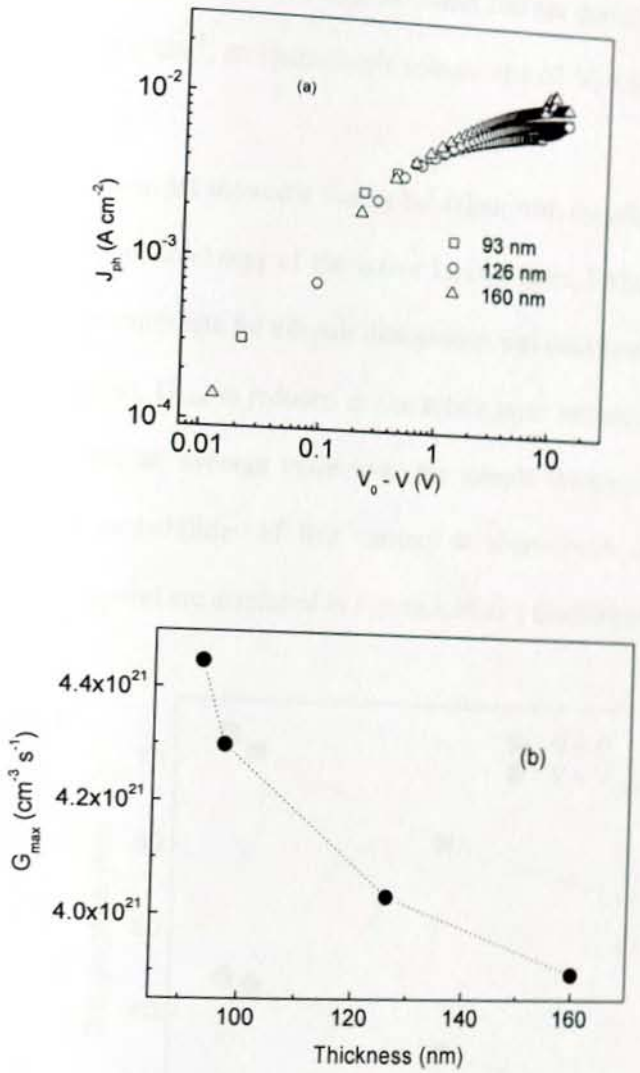

Figure 3.47 (a) The photocurrent curves against the effective voltage and for different thickness: 93 nm (squares); 126 nm (circles); 160 nm (triangles). (b) Maximum possible generation rate of free carriers in ITO/PEDOT:PSS/BisEH-PFDTBT:PCBM(1:4 w/w)/LiF/Al solar cells as a function of the active layer thickness.

The power conversion efficiency did not change a lot with the thickness, being compensated by an enhanced light harvesting ability for thicker active layers. The best overall performance was achieved with the blend 100 nm thick, showing a short-circuit current of 5.16 mA cm^{-2}, an open-circuit voltage of 1.07 V, a fill factor of 0.46 and a PCE of 2.57%.

The photocurrent showed a similar behaviour with the effective voltage for cells made with different thickness of the active layer, Figure 3.47a. From the saturation currents, the maximum rate for e-h pair dissociation was calculated.

As expected, G_{max} is reduced as the active layer becomes thicker and thicker, since it represents an average value over the sample thickness, Figure 3.47b. The generation rate probabilities of free carriers at short-circuit condition and at the maximum power point are displayed in Figure 3.48 as a function of the blend thickness.

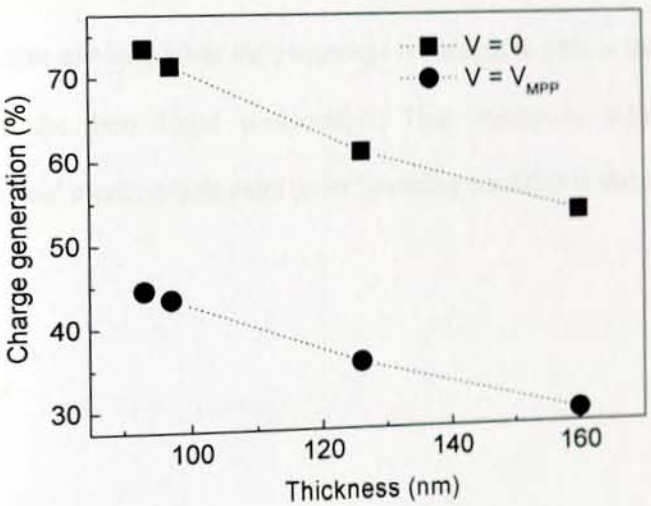

Figure 3.48 Probability of charge generation at short-circuit condition and at the maximum power point for ITO/PEDOT:PSS/BisEH-PFDTBT:PCBM(1:4 w/w)/LiF/Al solar cells as a function of the active layer thickness.

3.5.5 Conclusion

The overall performance of BisEH-PFDTBT:PCBM solar cells reaches its maximum at 80% by weight of fullerene content. Device made with active layers of comparable thickness and PCBM content ranging between 50% and 80% show J_{sc}, FF, shunt resistance, and efficiency increasing with the fullerene content, accomplished by a decreasing series resistance. This clearly indicates the device performance is mainly controlled by the donor/acceptor intermixed network formation rather than by the photon absorption ability, also confirmed by the trend with the active layer thickness. The dependence of V_{oc} with light power intensity indicates the occurrence of trapping effects at lower PCBM content. The best power conversion efficiency was achieved for 1:4 D:A weight ratio and the blend thickness of 100 nm.

A main loss mechanism is represented by the reduced ability of generation of free electron-hole pairs. At short circuit condition, only 64% of the photogenerated excitons leads to free carriers, while the percentage is reduced to 38% at the maximum power point for the best blend composition. This incomplete dissociation of photogenerated bound electron-hole pairs under operating condition is therefore a main lose mechanism.

4. References

1. C. E. Swenberg and M. Pope, *Electronic Processes in Organic Crystals and Polymers, 2nd ed., Oxford.* U. Press, New York, 1999.
2. P. M. Borsenberger and D. S. Weiss, *Organic Photoreceptors for Xerography.* CRC, 1998.
3. G. Malliaras and R. Friend, *Phys. Today*, 58 (2005) 53.
4. Ingmar Grenthe (Ed), *Nobel Lecture In chemistry 1996-2000*, Royal Institute of Technology, (2003), P 380.
5. Y. Sun and J.A. Rogers, *Adv. Mater*, 19 (2007) 1897.
6. F. C. Krebs and K. Norrman, *Progress in Photovoltaics*, 15 (2007) 697.
7. J. A. Hauch, P. Schilinsky, S. A. Choulis, R. Childers, M. Biele, and C .J. Brabec, *SolarEnergy Materials and Solar Cells*, 92 (2008) 727.
8. C. J. Brabec, V. Dyankonov, J. Parissi, N. Sc. Sariciftici (Eds), *Organic photovoltaics-concepts and realization*, Springer, Linz, (2003) p 92.
9. S. Roth, and D. Carroll, *One dimensional metals: Conjugated polymers, Organic crystals, Carbon Nanotubes*, Wiley-VCH Verlay Gmb and Co. Weinheim, (2004) p 134.
10. S. Kappaun, C. Slugovc and E. J. W. List, *Int. J. Mol. Sci. 9* (2008) 1527.
11. M. M. Mandoc, L. J. A. Koster, and P. W. M. Blom, *Appl. Phys. Lett.* 90 (2007) 133504.
12. G. Horowitz, *J. Mater. Res.* 19 (2004)1946.
13. C. Deibel, *Phys. Status Solidi A* 206 (2009) 2731.
14. J. M. Montero, J. Bisquert, G. Garcia-Belmonte, E. M. Barea and H. J. Bolink, *Org. Elect.* 10 (2009) 305.

15. A. Pivrikas1, N. S. Sariciftci, G.Juska and R. Osterbacka, *Prog. Photovolt: Res. Appl.* 15 (2007) 677.

16. V. Coropceanu, J. Cornil, D. da Silva Filho, Y. Olivier, R. Silbey, and J. L. Bredas, *Chem. Rev.* 107 (2007) 926.

17. W. Warta and N. Karl, *Phys.Rev. B* 32 (1985)1172.

18. N. Karl and J. Marktanner, *Mol. Cryst. Liq. Cryst.* 355 (2001)149.

19. V. Podzorov, E. Menard, J. A. Rogers and M. E. Gershenson, *Phys. Rev. Lett.* 95(2005) 26601.

20. O. Ostroverkhova, D. G. Cooke, F. A. Hegmann, J. E. Anthony, V. Podzorov, M. E. Gershenson, O. D. Jurchescu and T.T. M. Palstra, *Appl. Phys. Lett.* 88 (2006)162101.

21. G. Horowitz, *Adv. Polym. Sci.* 223 (2010)113.

22. P. G. L. Comber and W. E. Spear, *Phys. Rev. Lett.* 25 (1970) 509.

23. G. Horowitz, R. Hajlaoui and P. Delannoy, *J. Phys.* 5 (1995) 355.

24. M. Mottaghi and G. Horowitz, *Org. Electron.* 7 (2006) 528.

25. A. B. Kaiser, *Rep. Prog. Phys.* 64 (2001) 1.

26. R. Coehoorn, W. F. Pasveer, P. A. Bobbert and M. A. J. Michels, *Phys. Rev. B* 7 (2005)155206.

27. W. F. Pasveer, J. Cottaar, C. Tanase, R. Coehoorn, P. A. Bobbert, P. W. M. Blom, D. M. de Leeuw, and M. A. J. Michels, *Phys. Rev. Lett.* 94 (2005) 206601.

28. J. Frenkel, *Phys. Rev.* 54 (1938) 647.

29. H. Bassler Phys. Stat. Sol (b) 175 (1993) 15.

30. S. V. Novikov, D. H. Dunlap, V. M. Kenkre, P. E. Parris, and A. V. Vannikov, *Phys. Rev. lett.*81(1998) 4472.

31. S. Tiwari and N. C. Greenham, *Opt. Quant. Elect.* 41(2009) 69.

32. R. G. Kepler, *Phys. Rev.* 119 (1960) 1226.

33. M. Tan, W. Goh, J. Li, G. Pundir, V. Chellappan, and Z. Chen, *Appl. Mater. and Inter.* 2 (2010) 1414.

34. I. H. Campbell, D. L. Smith, C. J. Neef and J. P. Ferraris, *Appl. Phys. Lett.* 74 (1999) 2809.

35. G. Juska, K. Arlauskas, M. Viliunas, and J. Kocka, *Phys. Rev. Lett.* 84 (2000) 4946.

36. A. Pivrikas, N. S. Sariciftci, G. Juska, and R. Osterbacka, *Prog. Photovolt: Res. Appl.* 15 (2007) 677.

37. J. Lorrmann, B. H. Badada, O. Inganäs, V. Dyakonov, and C. Deibel, *J. Apl. Phys.* 108 (2010) 113705.

38. G. Juška, K. Arlauskas, M. Viliūnas, K. Genevičius, R. Österbacka, and H. Stubb, *Phys. Rev. B* 62 (2000) R16235.

39. S. Bange, M. Schubert, and D. Neher. *Phys. Rev. B* 81 (2010) 035209.

40. J. Lorrmann, B. H. Badada, O. Inganäs, V. Dyakonov, and C. Deibel, *J. Apl. Phys.* 108 (2010) 113705.

41. S. C. Tse, S. W. Tsang, and S. K. So, *J. Appl. Phys.* 100 (2006) 063708.

42. M. Abkowitz, J. S. Facci, and M. Stolka, *Appl. Phys. Lett.* 63 (1993) 1892.

43. A. J. Campbell, D. D. C. Bradley, H. Antoniadis, M. Inbasekaran, W. W.Wu, and E. P. Woo, *Appl. Phys. Lett.* 76 (2000) 1734.

44. A. Many and G. Rakavy, *Phys. Rev.* 126 (1962)1980.

45. D. Poplavskyy and J. Nelson, *J. Appl. Phys.* 93 (2003) 341.

46. M. A. Lampert and P. Mark, *Current Injection in Solids*, Academic, New York, 1970.

47. M. Schmeits, *J. Appl. phys.* 101 (2007) 084508.

48. H. C. F. Martens, W. F. Pasveer, H. B. Brom, J. N. Huiberts, and P. W. M. Blom, *Phys. Rev. B* 63 (2001) 125328.

49. S. Berleb and W. Brutting, *Phys. Rev. Lett.* 89 (2002) 286601.

50. H. Gommans, M. Kemerink, G. G. Andersson, and R. M. T. Pijper, *Phys. Rev. B* 69 (2004) 155216.

51. K. K. Tsung and S. K. So, *J. Appl. Phys.* 106 (2009) 083710.

52. D. Poplavskyy and F. So, *J. Apl. Phys.* 99 (2006) 033707.

53. H. C. F. Martens, J. N. Huiberts, and P. W. M. Blom, *Appl. Phys. Lett.* 77 (2000) 1852.

54. P. W. M. Blom, H. C. F. Martens and J. N. Huiberts, *Synth. Met.* 121 (2001)1621.

55. H. C. F. Martens, H. B. Brom, and P. W. M. Blom, *Phys. Rev. B* 60 (1999) R8489.

56. P. Mark and W. Helfrich, *J. Appl. Phys.* 33(1962) 205.

57. M. A. Lampert, Phys. Rev. 103 (1956)1648.

58. P. Stallinga *Electrical characterization of organic material and devices* ,John Wiley and Sons Ltd, 2009 ,Southern gate, UK p54.

59. L. J. A. Koster, *Phys. Rev. B*, 81 (2010) 205318.

60. P. W. M. Blom, M. J. M. de Jong, and M. G. van Munster, *Phys. Rev. B* 55 (1997) R656.

61. P. N. Murgatroyd, *J. Phys. D: Appl. Phys.* 3 (1970) 151.

62. V. D. Mihailetchi, J. K. van Duren, P. W. Blom, J. C. Hummelen, R. A. Janssen, J. M. Kroon, M. T. Rispens, W. J. H. Verhees and M. M. Wienk *Adv. Funct. Mater.* 13 (2003) 43.

63. R. E. Smalley, *MRS Bulletin* 30 (2005) 412.

64. Q. Schiermier, J. Tollefson, T. Scully, A. Witze and O. Morton, *Nature* 454 (2008) 816.

65. D. M. Chapin, C. S. Fuller, and G. L. Pearson, *J. Appl. Phys.* **25** (1954) 676.

66. M. A. Green, K. Emery, D. L. King, S. Igari and W. Warta, *Prog. Photovol.Res.Appl.* 11 (2003) 347.

67. M. D. McGehee, *Nature photo.* 3 (2009) 250.

68. D. Butler, *Nature* 454 (2008) 558.

69. C. J. Brabec, *Sol. Energy Mater. Sol. Cells* 83 (2004) 273.

70. C. J. Brabec, N. S. Sariciftci and J. C. Hummelen, *Adv. Funct. Mater.* 11 (2001) 15.

71. B. C. Thompson and J. M. J. Fréechet, *Angew. Chem., Int. Ed.* 47 (2008) 58.

72. R. Kroon, M. Lenes, J. C. Hummelen, P. W. M. Blom and B. de Boer, *Polym. Rev.* 48 (2008) 531.

73. C . W. Tang, *A ppl. Phys. Lett.* 48 (1986) 183.

74. M. Gràtzel, *Nature* 414 (2001) 338.

75. P. Peumans, V. Bulovic and S. R. Forrest, *Appl. Phys. Lett.* 76 (2000) 2650.

76. G. Yu, J. Gao, J. C. Hummelen, F. Wudl and A. J. Heeger, *Science* 270 (1995) 1789.

77. N. S. Sariciftci, L. Smilowitz, A. J. Heeger and F. Wudl, *Science* 258 (1992) 1474.

78. J. C. Hummelen, B. W. Knight, F. Lepeq, F. Wudl, J. Yao and C. L. Wilkins, *J. Org. Chem.* 60 (1995) 532.

79. S. E. Shaheen, C. J. Brabec, N. S. Sariciftci, F. Padinger, T. Fromherz and J. C. Hummelen, *Appl. Phys. Lett.*78 (2001) 841.

80. M. A. Green, K. Emery, Y. Hishikawa and W. Warta, *Prog. Photovoltaics* 19 (2011) 84.

81. R. F. Service, *Science* 332 (2011) 293.

82. M. D. McGehee and M. A. Topinka, *Nature mater* 5 (2006) 675.

83. P. W. M. Blom, V. D. Mihailetechi, L. J. A. Koster, and D. E. Markov, *Adv. Mater.* 19 (2007) 1551.

84. J. Nelson, *Materials today* 14 (2011) 462.

85. P.G. Nicholson and F.A. Castro, *Nanotechnology* 21 (2010) 492001.

86. K. M. Coakley and M. D. McGehee, *Chem. Mater.* 16 (2004) 4533.

87. J. J. M. Halls, C. A. Walsh, N. C. Greenham, E. A. Marseglia, R. H. Friend, S. C. Moratti, and A. B. Holme, *Nature* 376 (1995) 498.

88. P. Schilinsky, C. Waldauf and C. J. Brabec, *Appl. Phys.Lett.* 81 (2002)3885.

89. S. Gnes, H. Neugebauer, N. S. Sariciftci, *Chem. Rev.* 107 (2007) 1324.

90. C. J. Brabec, G. Zerza, N. S. Sariciftci, G. Cerullo, S. S. DeSilvestri Luzatti and J. C. Hummelen, *Chem. Phys. Lett.* 340 (2001) 232.

91. R. Koeppe and N. S. Saricifti, *Photochem. Photobiol. Sci.*5 (2006) 1122.

92. R. Po, M. Maggini and N. Camaioni, *J. Phys. Chem. C* 114 (2010)695.

93. S. Sun, Z. Fan, Y. Wang and J .Haliburton, *J. Mater. Sci.* 40 (2005) 1429.

94. V. D. Mihailetchi, J. K. van Duren, P. W. Blom, J. C. Hummelen, R. A. Janssen, J. M. Kroon, M. T. Rispens, W. J. H. Verhees and M. M. Wienk , *Adv. Funct. Mater.* 13 (2003) 43.

95. R. Sokel and R.C. Hughes, *J. Appl. Phys.* 53 (1982) 7414.

96. J .A. Barker, C. M. Ramsdale and N. C. Greenham, *Phys. Rev. B 67* (2003) 075205.

97. M. A. Baldo and S. R. Forrest, *Phys. Rev. B* 64 (2001) 085201.

98. B. Kippeler and J. Bredas, *Energy and Environ. Sci.* 2 (2009) 251.

99. G. Dennler, M. C. Scharber and C. J. Brabec, *Adv. Mater.*21 (2009) 1323.

100. M. C. Scharber, D. Muhlbacher, M. Koppe, P. Denk, C. Waldauf, A. J. Heeger, and C. J. Brabec, *Adv. Mat.* 18 (2006) 789.

101. D. Veldman, S. C. J. Meskers, and R. A. J. Janssen, *Adv. Funct. Mater.* 19 (2009) 1939.

102. C. J. Brabec, C. Winder, N. S. Sariciftci, J. C. Hummelen, A. Dhanabalan, P. A. van Hal and R. A. Janssen, *Adv. Funct. Mater*, 12 (2002)709.

103. G. D. Sharma, P. Suresh, S. S. Sharma, Y. K. Vijay and J. A. Mikroyannidis, *Appl. Mat. and Interf.* 2 (2010) 504.

104. M. Kroon, M. A. J. Michels and R. A. J. Janssen, *Nano Lett.* 5 (2005) 579.

105. T. Erb, U. Zhokhavets, G. Bobsch, S. Raleva, B. Stuehn, P. Schilinsky, C. Waldauf and C. J. Brabec, *Adv. Funct. Mater.* 15 (2005) 1193.

106. T. Ahn and H.L. Sein-Ho Ha, *Appl. Phys. Lett.* 80 (2002) 392.

107. P. J. Brown, D. S. Thomas, A. Kohler, J. S. Wilson, J. S. Kim, C. M. Ramsdale, H. Sirringhaus and R. H. Friend, *Phys. Rev. B* 67 (2003) 064203.

108. T. W. Lee and O. O. Park, *Macromolecules* 11 (2000) 801.

109. J. J. Dittmer, E. A. Marseglia and R. H. Friend, *Adv. Mater.* 12 (2000) 1270.

110. P. Vanlaeke, A. Swinnen, I. Haeldermans, G. Vanhoyland, T. Aernouts, D. Cheyns, C. Deibel, J. D. Haen, P. Heremans, J. Poortmans and J. V. Manca, *Sol. Energy Mater. Sol. Cells* 90 (2006) 2150.

111. C. J. Brabec, S. E. Shaheen, C. Winder, N .S. Sariciftci and P. Denk, *Appl. Phys. Lett.* 80 (2002) 1288.

112. I. Riedel, J. Parisi, V. Dyakonov, L. Lutsen, D. Vanderzande, and J. C. Hummelen, *Adv. Funct. Mater* 14 (2004) 38.

113. J. Gao, F. Hilde, and H. Wang, *Synth. Met.* 84 (1997) 979.

114. P. Schillinksy, C. Waldauf, and C. J. Brabec, *Appl. Phys. Lett.* 81(2002) 3885.

115. J. K. J. van Duren, X. N. Yang, C. W. T. Bulle-Lieuwma, A. B. Sieval, J. C. Hummelen, and R. A. J. Janssen, Adv. Funct. Mater. 14 (2004) 425.

116. V. Dyakonov, *Thin Solid Films* 451(2003) 493.

117. I. Riedel, N. Martin, F. Giacalone, J. L. Segura, D. Chirvase, J. Parisi, and V. Dyakonov, *Thin Solid Films* 451(2004) 43.

118. D. Gebeyehu, M. Pfeiffer, B. Maenning, J. Drechsel, A. Werner, and K. Leo, *Thin Solid Films* 451(2004) 29.

119. L. J. A. Koster, V. D. Mihailetchi, H. Xie, and P. W. M. Blom, *Appl. Phys. Lett.* 87 (2005) 203502.

120. S. R. Cowan, A. Roy, and A. J. Heeger, *Phys. Rev. B* 82 (2010) 245207

121. M. M. Mandoc, W. Veurman, L. J. A. Koster, B. de Boer, and P. W. M. Blom, *Adv. Funct. Mater.* 17 (2007) 2167

122. J. C. deMello, H. F. Wittman and R. H. Friend, *Adv. Mater.* 9 (1997) 230.

123. G. K. J Gritzner. *Pure Appl. Chem.* 56 (1984) 461.

124. L. Bonoldi, A. Calabrese, A. Pellegrino, N. Perin, R. Po, S. Spera, A. Tacca, *J. Mater. Sci* 46 (2011) 3960.

125. A. Calabrese, A. Pellegrino, R. Po, A. Savoini, F. Tinti, N. Camaioni, *Solar Energy Mate. and Solar Cells* 95 (2011) 3428.

126. W. Mammo, S. Admassie, A. Gadisa, F. Zhang, O. Inganäs, and M. R. Andersson, *Sol. Energy Mater. Sol. Cells* 91 (2007) 1010.

127. S. Admassie, *Ph.D. thesis*, Addis Ababa University, 2006.

128. S .E. Debebe, W. Mammo, T. Yohannes, F. Tinti, A. Zanelli, and N. Camaioni, *Appl. Phys. Lett.* 96 (2010) 082109.

129. K. Kassing, *Phys. Status Solidi A* 28 (1975) 107.

130. T. Okachi, T. Nagase, T. Kobayashi, and H. Naito, *Jpn. J. Appl. Phys.* 47 (2008) 8965.

131. P. W. M. Blom, H. C. F. Martens, and J. N. Huiberts, *Synth. Met.* 121 (2001) 1621.

132. P. M. Borsenberger and D. S. Weiss, *Organic Photoreceptors for Xerography, Marcel Dekker*, New York, 1998, p. 274.

133. T. Tiedje and A. Rose, *Solid State Commun.* 37 (1981) 49.

134. H. Scher and E. W. Montroll, *Phys. Rev. B* 12 (1975) 2455.

135. X. J. Wang, E. Perzon, F. Oswald, F. Langa, S. Admassie, M. R. Andersson,and O. Inganäs, *Adv. Funct. Mater.* 15 (2005)1665.

136. F. Zhang, W. Mammo, L. M. Andersson, S. Admassie, M. R. Andersson and O. Inganäs, *Adv. Mater.* 18 (2006) 2169.

137. S. E. Debebe, W. Mammo, T. Yohannes, F. Tinti, A. Martelli, and N. Camaioni, *J. Appl. Phys.* 108 (2010) 023709.

138. F. Tinti, S. E. Debebe, W. Mammo, T. Yohannes, N. Camaioni, *Synth. Met.* 161 (2011) 794.

139. Y. Hirose, A. Kahn, V. Aristov, P. Soukiassian, V. Bulovic, and S. R. Forrest, *Phys. Rev. B* 54 (1996) 13748.

140. I. G. Hill, A. Rajagopal, and A. Kahn, *J. Appl. Phys.* 84 (1998) 3236.

141. F.Huang, K. Chen, H. Yip, S. K. Hau, O. Acton, Y. Zhang, J. Luo, and A. K. Jen, *J. Am. Chem. Soc.* 131 (2009) 13886.

142. N. D. Nguyen, M. Schmeits, and H. P. Loebl, *Phys. Rev. B* 75 (2007) 075307.

143. M. Schmeits, *J. Appl. Phys.* 101 (2007) 084508.

144. H. Bassler, *Phys. Status Solidi B* 175 (1993) 15.

145. S. C. Tse, S. W. Tsang, and S. K. So, *J. Appl. Phys.* 100 (2006) 063708.

146. Y. Yamashita, *Sci. Technol. Adv. Mater.* 10 (2009) 024313.

147. M. R. Andersson, M. Berggren, O. Inganaes, G. Gustafsson, J. C. Gustafsson-Carlberg, D. Selse, T. Hjertberg and O. Wennerstroem, *Macromolecules* 28 (1995) 7525.

148. *Handbook of Thiophene-based Materials: Applications in Organic Electronics and Photonics*, Volume 1, Eds. Igor F. Perepichka, Dmitrii F. Perepichka, John Wiley and Sons, 2009.

149. T. Johansson, W. Mammo, M. Svensson, M. R. Andersson and O. Inganas, *J. Mater. Chem.* 13 (2003) 1316.

150. I. F. Perepichka, D. F. Perepichka, H. Meng and F. Wudl, *Adv. Mater.* 17 (2005) 2281.

151. F. L. Zhang, M. Svensson , M. R. Andersson, M. Maggini, S. Bucella, E. Menna, O. Inganas, *Adv. Mater.* 13 (2001)1871.

152. S. E. Debebe, D. A. Gedefaw, W. Mammo, T. Yohannes, F. Tinti, A. Zanneli, V. Fattori, N. Camaioni, *J. Poly. Sc. A: Poly. Chem.* 49 (2011) 2693.

153. X. Jiang, R. Osterbacka, O. Korovyanko, C. P. An, B. Horowitz, R. A. J. Janssen and Z. V. Vardeny, *Adv. Funct. Mater.* 12 (2002) 587.

154. R. D. McCullough, R. D. Lowe, M. Jayraman and D. L. Anderson, *J. Org. Chem.* 58 (1993) 904.

155. K. E. Aasmundtveit, E. J. Samuelsen, W. Mammo M. Svensson, .M. R. Andersson, L. A. A. Pettersson and O. Inganas, *Macromolecules* 33 (2000) 5481.

156. K. Kanemoto, T. Sudo, I. Akai, H. Hashimoto, T. Karasawa, Y. Aso and T. Otsubo, *Phys. Rev. B* 73 (2006) 235203.

157. M. Theander, O. Inganas, W. Mammo, T. Olinga, M. Svensson and M. R. Andersson, *J. Phys. Chem. B.* 103 (1999) 7771.

158. S. Trasatti. *Pure Appl. Chem.* 58 (1986) 955.

159. I. H. Campbell, T. H. Hagler, D. L. Smith and J. P. Ferraris, *Phys. Rev. Lett.* 76 (1996)1900.

160. C. H. Woo, T. W. Holcombe, D. A. Unruh, A. Sellinger and J. M. Frechert, *Chem. Mater.* 22 (2010) 1673.

161. Q. Pei, H. Jarvinen, J. E. Osterholm, O. Inganas, J. Laakso, *Macromolecules* 25 (1992) 4297.

162. H. H. Poole, *Philos. Mag.* 33 (1916) 112.

163. S. Roquet, A. Cravino, P. Leriche, O. Alévêque, P. Frère and J. Roncali, *J. Ame. Chem. Soc.* 128 (2006) 3459.

164. M. Svensson, F. Zhang, S .C. Veenstra, W. J. H. Verhees, J .C. Hummelen, J. M. Kroon, O. Inganäs and M. R. Andersson, *Adv. Matet.* 15 (2003) 988.

165. D. Kitazawa, N. Watanabe, S. Yamamoto and J. Tsukamoto, *Appl. Phys. Lett.* 95 (2009) 053701.

166. M. Chen, J. Hou, Z. Hong, G. Yang, S. Sista, L. Chen and Y. Yan, *Adv. Mater.* 21 (2009) 4238.

167. L. J. Lindgren, F. Zhang, M. Andersson, S. Barrau, S. Hellstrom, W. Mammo, E. Perzon, O. Inganäs and M. R. Andersson, *Chem. Mat.* 21 (2009) 3491.

168. Y. Li, H. Li, B. Xu, Z. Li, F. Chen, D. Feng, J. Zhang and W. Tian, *Polymer* 51 (2010) 1786.

169. N. Blouin, A. Michaud and M. Leclerc, *Adv. Mat.* 19 (2007) 2295.

156. K. Kanemoto, T. Sudo, I. Akai, H. Hashimoto, T. Karasawa, Y. Aso and T. Otsubo, *Phys. Rev. B* 73 (2006) 235203.

157. M. Theander, O. Inganas, W. Mammo, T. Olinga, M. Svensson and M. R. Andersson, *J. Phys. Chem. B.* 103 (1999) 7771.

158. S. Trasatti. *Pure Appl. Chem.* 58 (1986) 955.

159. I. H. Campbell, T. H. Hagler, D. L. Smith and J. P. Ferraris, *Phys. Rev. Lett.* 76 (1996)1900.

160. C. H. Woo, T. W. Holcombe, D. A. Unruh, A. Sellinger and J. M. Frechert, *Chem. Mater.* 22 (2010) 1673.

161. Q. Pei, H. Jarvinen, J. E. Osterholm, O. Inganas, J. Laakso, *Macromolecules* 25 (1992) 4297.

162. H. H. Poole, *Philos. Mag.* 33 (1916) 112.

163. S. Roquet, A. Cravino, P. Leriche, O. Alévêque, P. Frère and J. Roncali, *J. Ame. Chem. Soc.* 128 (2006) 3459.

164. M. Svensson, F. Zhang, S .C. Veenstra, W. J. H. Verhees, J .C. Hummelen, J. M. Kroon, O. Inganäs and M. R. Andersson, *Adv. Matet.* 15 (2003) 988.

165. D. Kitazawa, N. Watanabe, S. Yamamoto and J. Tsukamoto, *Appl. Phys. Lett.* 95 (2009) 053701.

166. M. Chen, J. Hou, Z. Hong, G. Yang, S. Sista, L. Chen and Y. Yan, *Adv. Mater.* 21 (2009) 4238.

167. L. J. Lindgren, F. Zhang, M. Andersson, S. Barrau, S. Hellstrom, W. Mammo, E. Perzon, O. Inganäs and M. R. Andersson, *Chem. Mat.* 21 (2009) 3491.

168. Y. Li, H. Li, B. Xu, Z. Li, F. Chen, D. Feng, J. Zhang and W. Tian, *Polymer* 51 (2010) 1786.

169. N. Blouin, A. Michaud and M. Leclerc, *Adv. Mat.* 19 (2007) 2295.

170. Y. P. Zou, D. Gendron, R. Badrou-Aich, A. Najar, Y. Tao and M. Leclerc, *Macromolecules* 42 (2009) 2891.

171. P. L. T. Boudreault, A. Michaud and M. Leclerc, *Macro. Rap. Comm.* 28 (2007) 2176.

172. D. Muhlbacher, M. Scharber, M. Morana, Z. G. Zhu, D. Waller and R. Gaudiana, *Adv. Mat.* 18 (2006) 2931.

173. K. C. Li, Y. C. Hsu, J. T. Lin, C. C. Yang, K. H. Wei and H. C. Lin, *J. Poly. Sc. Part A-Poly. Chem.* 47 (2009) 2073.

174. A. J. Moule, A. Tsami, T. W. Buennagel, M. Forster, N. M. Kronenberg and M. Scharber *Chem. Mate.* 20 (2008) 4045.

175. E. J. Zhou, M. Nakamura, T. Nishizawa, Y. Zhang, Q. S. Wei and K. Tajima, *Macromolecules* 41(2008) 8302.

176. E. J. Zhou, S. Yamakawa, K. Tajima, C. H. Yang and K. Hashimoto, *Chem. Mat.* 21 (2009) 4055.

177. L. Liao, L. M. Dai, A. Smith, M. Durstock, J. P. Lu and J. F. Ding, *Macromolecules* 40 (2007) 9406.

178. J. Kim, S. H. Park, S. Cho, Y. Jin, J. Kim and I. Kim, *Polymer* 51 (2010) 390.

179. F. L. Zhang, J. Bijleveld, E. Perzon, K. Tvingstedt, S. Barrau and O. Inganäs *J. Mat. Chem.* 18 (2008) 5468.

180. A. B. Tamayo, X. D. Dang, B. Walker, J. Seo, T. Kent and T. Q. Nguyen, *Appl. Phy. Lett.* 94 (2009) 103301.

181. A. P. Zoombelt, J. Gilot, M. A. Wienk and R. A. J. Janssen, *Chem. Mat.* 21 (2009) 1663.

182. A. Palmaerts, L. Lutsen, T. J. Cleij, D. Vanderzande, A. Pivrikas and H. Neugebauer, *Polymer* 50 (2009) 5007.

183. L. H. Nguyen, H. Hoppe, T. Erb, S. Gunes, G. Gobsch and N. S. Sariciftci, *Adv. Func. Mat.* 17 (2007) 1071.

184. O. Inganäs, M. Svensson, F. Zhang, A. Gadisa, N. K. Persson and X. Wang, *Appl. Phys. A-Mat. Sc. & Proc.* 79 (2004) 31.

185. E. G. Wang, M. Wang, L. Wang, C.H. Duan, J. Zhang and W. Z Cai, *Macromolecules* 42 (2009) 4410.

186. M. Jayakannan, P. A. Van Hal and R. A. J. Janssen, *J. Poly. Sc. Part A-Poly. Chem.* 40 (2002) 2360.

187. M. Jayakannan, P. A. Van Hal and R. A. J. Janssen, *J. Poly. Sc. Part A-Poly. Chem.* 40 (2002) 251.

188. R. P. Qin, W. W. Li, C. H. Li, C. Du, C. Veit and H.F Schleiermacher, *J. Ame. Chem. Soc.* 131 (2009) 14612.

189. A. Calabrese, A. Pellegrino, R. Po, N. Perin, A. Tacca, L. Longo, N. Camaioni, F. Tinti, S. E. Debebe, S. Patanè and A. Consoli, *Int. Fed. Info. Pro. AICT* 349 (2011) 596.

190. V. D. Mihailetchi, J. Wildeman, and P. W. M. Blom, *Phys. Rev. Let.* 94 (2005) 126602.

191. L. J. A. Koster, V. D. Mihailetchi, and P. W. M. Blom, *Appl. Phys. Let.* 88 (2006) 052104.

192. N. K. Persson, M. Sun, P. Kjellberg, T. Pullerits and O. Inganäs, *J. Chem. Phys.* 123 (2005) 204718.

193. R. S. Ashraf, M. Shahid, E. Klemm, M. Al-Ibrahim and S. Sensfuss, *Macromol. Rapid. Commun* 27 (2006) 1454.

194. A. Gadisa, W. Mammo, M. Andersson, S. Admassie, F. Zhang, M. R. Andersson and O. Inganäs, *Adv. Funct. Mater.* 17(2007) 3836.

195. L. H. Slooff, S. C. Veenstra, J. M. Kroon, D. J. D. Moet, J. Sweelssen and M. M. Koetse, *Appl. Phys. Lett.* 90 (2007)143506.

196. A. Calabrese, G. Schimperna, R. Po, T. Yohannes S. E. Debebe, F. Tinti, and N.Camaioni *J. Appl. Phys.* 110 (2011) 113106.

197. D. Chirvase, J. Parisi, J. C. Hummelen and V. Dyakonov, *Nanotechnology* 15 (2004) 1317.

198. G. Li, V. Shrotriya, Y. Yao and Y. Yang, *J. Appl. Phys.* 98 (2005) 043704.

199. M. Campoy-Quiles, T. Ferenczi, T. Agostinelli, P. G. Etchegoin, Y. Kim, T. D. Anthopoulos, P. N. Stavrinou, D. D. C. Bradley and J. Nelson, *Nature Mater.* 7 (2008)158.

200. L. J. A. Koster, V. D. Mihailetchi, R. Ramarker and P. W. M. Blom, *Appl. Phys. Lett.* 86 (2005)123509.

201. M. M. Mandoc, F. B. Kooistra, J. C. Hummelen, B. de Boer and P. W. M. Blom, *Appl. Phys. Lett.* 91 (2007) 263505.

202. I. W. Hwang, D. Moses and A. J. Heeger, *J. Phys. Chem. C* 112 (2008) 4350.

203. V. D. Mihailetchi, L. J. A. Koster, J. C. Hummelen and P. W. M. Blom, *Appl. Phys. Lett.* 93 (2004) 216601.